



TURKISH JOURNAL OF ENGINEERING

EDITOR IN CHIEF

Prof. Dr. Murat YAKAR
Mersin University Engineering Faculty
Turkey

CO-EDITORS

Prof. Dr. Erol YAŞAR
Mersin University Faculty of Art and Science
Turkey

Prof. Dr. Cahit BİLİM
Mersin University Engineering Faculty
Turkey

Assist. Prof. Dr. Hüdaverdi ARSLAN
Mersin University Engineering Faculty
Turkey

ADVISORY BOARD

Prof. Dr. Orhan ALTAN
Honorary Member of ISPRS, ICSU EB Member
Turkey

Prof. Dr. Armin GRUEN
ETH Zurich University
Switzerland

Prof. Dr. Hacı Murat YILMAZ
Aksaray University Engineering Faculty
Turkey

Prof. Dr. Artu ELLMANN
Tallinn University of Technology Faculty of Civil Engineering
Estonia

Assoc. Prof. Dr. E. Çağlan KUMBUR
Drexel University
USA

TECHNICAL EDITORS

Prof. Dr. Roman KOCH
Erlangen-Nurnberg Institute Palaontologie
Germany

Prof. Dr. Hamdalla WANAS
Menoufyia University, Science Faculty
Egypt

Prof. Dr. Turgay CELIK
Witwatersrand University
South Africa

Prof. Dr. Muhsin EREN
Mersin University Engineering Faculty
Turkey

Prof. Dr. Johannes Van LEEUWEN
Iowa State University
USA

Prof. Dr. Elias STATHATOS
TEI of Western Greece
Greece

Prof. Dr. Vedamanickam SAMPATH
Institute of Technology Madras
India

Prof. Dr. Khandaker M. Anwar HOSSAIN
Ryerson University
Canada

Prof. Dr. Hamza EROL
Mersin University Engineering Faculty
Turkey

Prof. Dr. Ali Cemal BENIM
Duesseldorf University of Applied Sciences
Germany

Prof. Dr. Mohammad Mehdi RASHIDI
University of Birmingham
England

Prof. Dr. Muthana SHANSAL
Baghdad University
Iraq

Prof. Dr. Ibrahim S. YAHIA
Ain Shams University
Egypt

Assoc. Prof. Dr. Kurt A. ROSENTRATER
Iowa State University
USA

Assoc. Prof. Dr. Christo ANANTH
Francis Xavier Engineering College
India

Prof. Dr. Bahadır K. KÖRBAHTI
Mersin University Engineering Faculty
Turkey

Assist. Prof. Dr. Akın TATOGLU
Hartford University College of Engineering
USA

Assist. Prof. Dr. Şevket DEMİRCİ
Mersin University Engineering Faculty
Turkey

Assist. Prof. Dr. Yelda TURKAN
Oregon State University
USA

Assist. Prof. Dr. Gökhan ARSLAN
Mersin University Engineering Faculty
Turkey

Assist. Prof. Dr. Seval Hale GÜLER
Mersin University Engineering Faculty
Turkey

Assist. Prof. Dr. Mehmet ACI
Mersin University Engineering Faculty
Turkey

Dr. Ghazi DROUBI
Robert Gordon University Engineering Faculty
Scotland, UK

JOURNAL SECRETARY

Aydin Alptekin
aydinalptekin@mersin.edu.tr

TURKISH JOURNAL OF ENGINEERING (TUJE)

Turkish Journal of Engineering (TUJE) is a multi-disciplinary journal. The Turkish Journal of Engineering (TUJE) publishes the articles in English and is being published 4 times (January, April, July and October) a year. The Journal is a multidisciplinary journal and covers all fields of basic science and engineering. It is the main purpose of the Journal that to convey the latest development on the science and technology towards the related scientists and to the readers. The Journal is also involved in both experimental and theoretical studies on the subject area of basic science and engineering. Submission of an article implies that the work described has not been published previously and it is not under consideration for publication elsewhere. The copyright release form must be signed by the corresponding author on behalf of all authors. All the responsibilities for the article belongs to the authors. The publications of papers are selected through double peer reviewed to ensure originality, relevance and readability.

AIM AND SCOPE

The Journal publishes both experimental and theoretical studies which are reviewed by at least two scientists and researchers for the subject area of basic science and engineering in the fields listed below:

- Aerospace Engineering
- Environmental Engineering
- Civil Engineering
- Geomatic Engineering
- Mechanical Engineering
- Geology Science and Engineering
- Mining Engineering
- Chemical Engineering
- Metallurgical and Materials Engineering
- Electrical and Electronics Engineering
- Mathematical Applications in Engineering
- Computer Engineering
- Food Engineering

PEER REVIEW PROCESS

All submissions will be scanned by iThenticate® to prevent plagiarism. Author(s) of the present study and the article about the ethical responsibilities that fit PUBLICATION ETHICS agree. Each author is responsible for the content of the article. Articles submitted for publication are priorly controlled via iThenticate ® (Professional Plagiarism Prevention) program. If articles that are controlled by iThenticate® program identified as plagiarism or self-plagiarism with more than 25% manuscript will return to the author for appropriate citation and correction. All submitted manuscripts are read by the editorial staff. To save time for authors and peer-reviewers, only those papers that seem most likely to meet our editorial criteria are sent for formal review. Reviewer selection is critical to the publication process, and we base our choice on many factors, including expertise, reputation, specific recommendations and our own previous experience of a reviewer's characteristics. For instance, we avoid using people who are slow, careless or do not provide reasoning for their views, whether harsh or lenient. All submissions will be double blind peer reviewed. All papers are expected to have original content. They should not have been previously published and it should not be under review. Prior to the sending out to referees, editors check that the paper aim and scope of the journal. The journal seeks minimum three independent referees. All submissions are subject to a double blind peer review; if two of referees gives a negative feedback on a paper, the paper is being rejected. If two of referees gives a positive feedback on a paper and one referee negative, the editor can decide whether accept or reject. All submitted papers and referee reports are archived by journal Submissions whether they are published or not are not returned. Authors who want to give up publishing their paper in TUJE after the submission have to apply to the editorial board in written. Authors are responsible from the writing quality of their papers. TUJE journal will not pay any copyright fee to authors. A signed Copyright Assignment Form has to be submitted together with the paper.

PUBLICATION ETHICS

Our publication ethics and publication malpractice statement is mainly based on the Code of Conduct and Best-Practice Guidelines for Journal Editors. Committee on Publication Ethics (COPE). (2011, March 7). Code of Conduct and Best-Practice Guidelines for Journal Editors. Retrieved from http://publicationethics.org/files/Code%20of%20Conduct_2.pdf

PUBLICATION FREQUENCY

The TUJE accepts the articles in English and is being published 4 times (January, April, July and October) a year.

CORRESPONDENCE ADDRESS

Journal Contact: tuje@mersin.edu.tr

CONTENTS

Volume 7 – Issue 2

RESEARCH ARTICLES

Design and walking analysis of proposed four-legged glass cleaning robot Nihat Çabuk	82
Facile production of CsPbBr₃ perovskite single-crystals in a hydrobromic solution Murat Özen, Cansu Akyel, Songül Akbulut Özen.....	92
Enhancing the seismic performance of high-rise buildings with lead rubber bearing isolators Ahmet Hilmi Deringöl, Esra Mete Güneysi.....	99
An alternative method for the particle size distribution: Image processing Mert Aydın, Talas Fikret Kurnaz	108
A comparative assessment for efficient oleuropein extraction from olive leaf (<i>Olea europaea</i> L. folium) Yaşar Kemal Reçepoğlu, Gülin Gümüşbulut, Aşlı Yüksel Özşen.....	116
Determination of optimum design parameters of glow plug and experimental verification Muciz Özcan, Muhammed Fahri Ünlerşen, Mehmet Şen.....	125
A four-wall virtual reality visualization of patient-specific anatomy: Creating full user immersive experience from computed tomography scans Hesham Tanbour, Emad Tanbour.....	134
Sentiment analysis with ensemble and machine learning methods in multi-domain datasets Muhammet Sinan Başarslan, Fatih Kayaalp.....	141
Determination of the critical drop height and critical flow velocity of aluminum alloy (AL-91% Mg-8% Fe-0.4% Zn-0.2%) in gravity sand casting Francis Inegbedion, James Chinedu Orji.....	149
Collapse capacity assessment of non-ductile open ground story reinforced concrete frame Emre Akin, Emad Kanas.....	157



Design and walking analysis of proposed four-legged glass cleaning robot

Nihat Çabuk *¹ 

¹Aksaray University, Vocational School of Technical Sciences, Türkiye

Keywords

Serial manipulator
Legged-robot
Glass cleaning
Design
Kinematic analysis

Research Article

DOI: 10.31127/tuje.1011320

Received: 18.10.2021

Accepted: 29.03.2022

Published: 26.04.2022

Abstract

In this study, a legged and wheeled robot model was proposed for cleaning the glass of greenhouses. The robot has four wheels and four legs, each with three degrees of freedom (DOF). The design, kinematic analysis and simulation of the robot was carried out. Glass greenhouses are created by placing glass sheets on T-shaped iron bars arranged in parallel at certain intervals. The robot performs the glass cleaning task by performing two different movements on greenhouse roof. As a first movement, the robot moves like a train moving on the rail on iron bars with wheels, cleaning the glass as it travels. After cleaning the glasses placed between two iron bars along a column, as second movement, the robot passes the next column using legs. These two movements continue until the entire roof of the greenhouse is cleaned. Kinematic analysis of this robot, which is designed with mechanical properties that can make these movements, has been made. Walking simulation of the robot was carried out according to the kinematic analysis. The simulation results showed that this proposed robot can be used to clean glass on the greenhouse roof.

1. Introduction

The use of robots is increasing day by day in parallel with the technological developments in robot components such as sensors, electric motors and controllers. This increase has led to the need for robots to be categorized into some of their features. The classification of robots can be made according to many criteria such as whether they move or not, where they are used, drive systems and the structures of their arms or legs. [1-7]. These classifications can be further reproduced according to different characteristics. Studies on all these classifications can be found in the literature [8-9]. These studies can be on both design and control according to the usage areas of the robots [10]. Deng et al. [11] have proposed several methods for hexapod robots to overcome object handling problems by using one or both legs as an arm when walking on other legs. Robots are also an important part of agricultural activities such as fertilizing and spraying as well as planting and harvesting [12-14]. Ling et al. [15] developed a mobile robot to tomato harvesting. This

robot, which has two arms, each with two degrees of freedom (DOF), also has a sensor that detects tomatoes.

It is also possible to find studies for general cleaning [16] and cleaning glass in buildings [17]. Sun et al. [18] designed a climbing robot to clean glasses for high rise buildings. Their robot has suction cups to stick on the glass and it moves with a translation mechanism. Antonelli et al. [19] carryout an experimental study on cleaning robot to clean dust on solar photovoltaic panels in solar plants. Li et al. [20] explored different greenhouse cleaning machines. Also, they analyzed the current state of development and prospects of greenhouse cleaning equipment and made some suggestions. Seemuang [21] study on cleaning mechanism to clean roof of plastic sheeting greenhouse.

According to the literature searches, no study has been found on a robot that performs the task of cleaning the glass of greenhouses. Therefore, in this study, a four-legged and four-wheeled mobile robot that cleans the glass of greenhouse roofs was designed, kinematic analysis was performed and simulation was carried out.

* Corresponding Author

^{*}(nihatcabuk@aksaray.edu.tr) ORCID ID 0000-0002-3668-7591

Cite this article

Çabuk, N. (2023). Design and walking analysis of proposed four-legged glass cleaning robot. Turkish Journal of Engineering, 7(2), 82-91

This study consists of the following sections. In the following section, the structural features of the greenhouses were examined and the reason for this study was explained. Next, a solid model of a greenhouse was created and associated with the designed robot and the physical properties of the robot were determined in accordance with the field of use and purpose and a solid model was created. Besides, mathematical equations were obtained by performing kinematic analysis according to this model. In the third section, the robot's walking simulation was performed and its applicability in a real environment was evaluated. In the fourth section, the study was concluded.

2. Method

2.1. Problem overview

Glass greenhouses are structures that can take sunlight well, where air conditioning can be done very well. Although these greenhouses differ according to the region, they are closed areas where fruits and mostly vegetables are grown in cold weather conditions. As it is known, it is an important issue that the glass of these greenhouses, which has a structure that permits sunlight, which is one of the most basic needs of plants although some plants may decrease their yields if exposed to intense sunlight to be transparent in order to pass this light sufficiently, especially in winter. Although it is partially cleaned due to the rain during the year, the cleaning of these glasses, whose transparency decreases over time due to various reasons, is also important due to the reasons mentioned above.

Glass greenhouses are formed by placing certain sizes of glass layers on grids of iron bars (T shape). These glass sheets are generally 550x600 and 500x550 mm in size. Fig. 1 shows a general glass greenhouse subject to this study.



Figure 1. Glass greenhouse structure

2.2. Cleaning strategy

The designed robot has four legs and four wheels. While the wheels enable the robot to move on two fixed iron bars, similar to the movement of the train on the rails, the four legs enable the robot to pass on the other two iron bars. The direction of movement of the robot with wheels and the direction of movement with legs can be seen in Fig. 2.

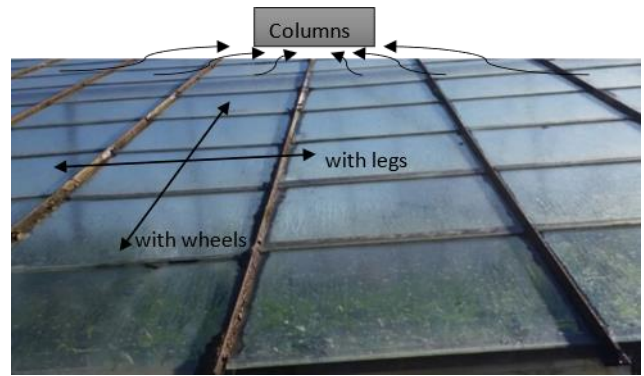


Figure 2. Motion directions of the robot on greenhouse roof

The glass is cleaned with the rotating brush on the robot body and the water coming from the water hose connected externally to the robot. After one column is completely cleaned by the movement of the wheels, the robot moves to the other column by its legs. Both legs and wheels are driven by electric motors. In addition to these, since the brushing system is operated by an electric motor, the electrical energy needed by the robot will be quite high. Thus, this energy is not provided by a battery, but by a cable connected to the electricity grid.

The angle of inclination of the iron bars forming the roof of greenhouses is usually between 20 and 30 degrees in practice. The section view of the greenhouse solid model created by selecting this angle as approximately 30 degrees is given in Fig. 3. Although this angle is a variable that affects the motion of the robot, this study does not include dynamic analysis involving the motion of the robot.

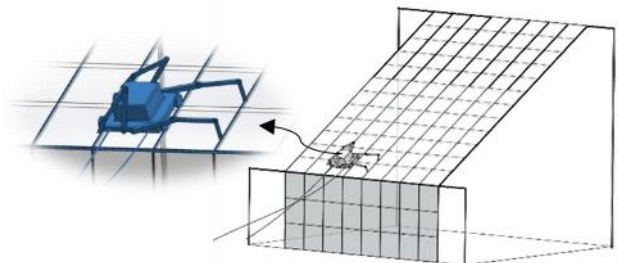


Figure 3. Solid model the greenhouse section and the robot on roof

The serial manipulators that make up the structure of the robot designed within the scope of this study are the mechanisms used in both any legged robot and industrial robot arms. The fields of use can be diversified by adding the required equipment according to the purpose and place of use [22-26].

Each limb of serial manipulators is connected one after the other. These connections are made with rotary, spherical or prismatic joints. The robot designed in this study has serial manipulators and rotational joints are used in these manipulators. The most common example of the use of serial manipulators is industrial robot arms. In these robot arms, the limbs connected to each other by joints, the limb in the base frame and the limb farthest from the base frame and the end actuator is always the same task. Thus, the kinematic chain of the manipulator is formed from the base frame to the end effector fame.

In robots where serial manipulators are used, kinematic analysis of the manipulator should be performed in order to define the robot's motion mathematically. The complexity of this kinematic equation increases as the degree of freedom of the manipulator increases and the rotation axes of the successive joints differ. Kinematic analysis is carried out in two ways: forward kinematics, where the positions of the manipulator's limbs can be determined according to the angle value of the joints and the dimensions of the limbs, and inverse kinematics,

$$\begin{aligned} P_x &= l_1 \cos(\theta_1) + l_2 \cos(\theta_1 + \theta_2) + l_3 \cos(\theta_1 + \theta_2 + \theta_3) \\ P_y &= l_1 \sin(\theta_1) + l_2 \sin(\theta_1 + \theta_2) + l_3 \sin(\theta_1 + \theta_2 + \theta_3) \end{aligned} \quad (1)$$

Here, θ_1 is the angle between the reference axis of the first limb of the serial manipulator, θ_2 is the angle between the the second limb and the axis of first limb and θ_3 is the angle between the third limb and the axis of second limb. Similarly, l_1 , l_2 and l_3 are the lengths of the first, second and third limb of the manipulator, respectively. Besides, P_x and P_y are the coordinates of the manipulator's endpoint. In the following section, kinematic analysis of a four-legged robot, each consisting of 3-DOF planar manipulators, is performed.

2.3. Mechanical design

This proposed four-legged robot basically consists of four serial manipulators with 3-DOF. These legs serve to carry the robot body to the iron bar on one side. In addition, it has four wheels driven by an electric motor that move the robot body on iron bars as seen in Fig. 2 and Fig. 3. The roller brush placed under the body of the robot cleans the glass while moving in the same column with the robot wheels. The water required in this cleaning process is provided by the water hose connected to the robot body. Similarly, the electrical energy needed by the robot is transmitted to the robot with the power cable. The motor drivers, power supply and control unit required for the electric motors which are in leg joints, drive the wheels and rotating the brush are in the chamber on the robot as seen in Fig. 4.

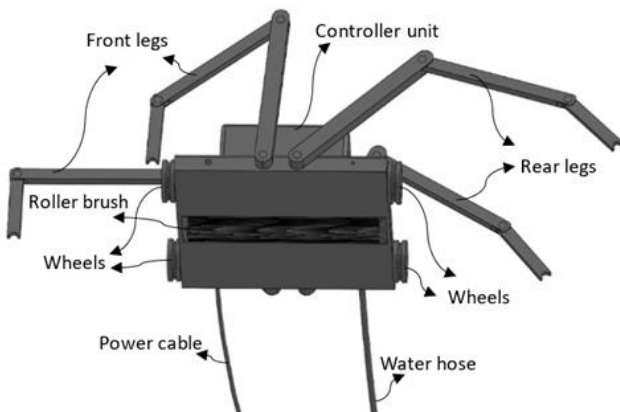


Figure 4. Components of the cleaning robot

In order to obtain the kinematic equations of the robot, the physical description of the robot body is made

where the required joint angles for the desired position and orientation of the limbs are determined. The position relation between the limbs of manipulators that can move in three axes can be established by writing in matrix form using the coordinate axis sets assigned to the joints, while this relationship can be established more simply in planar manipulators moving in two axes. Equation 1 is the forward kinematic equation of a 3-DOF planar manipulator.

in Fig. 5. Since the other two legs of the robot are the same as these two legs, it is not shown in this figure.

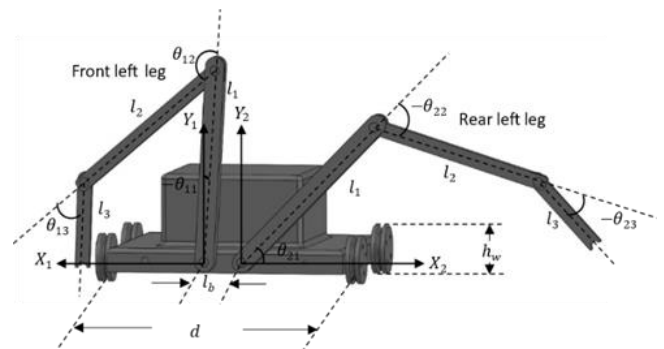


Figure 5. The cleaning robot structure

Here, d is the distance between the two wheels and also represents the distance between the two iron bars. h_w is the diameter of the wheel and l_b is the distance between the axes of rotation of the first joints of the front and rear legs. l_1 , l_2 and l_3 are length of leg limbs. θ_{11} is the angle between the reference axis of the first limb of the serial manipulator, θ_{12} is the angle between the the second limb and the axis of first limb and θ_{13} is the angle between the third limb and the axis of second limb for front legs. θ_{21} , θ_{22} and θ_{23} represent the same variables for the rear legs. Although the installation of greenhouses is made to certain standards, the dimensions of the robot body and legs should be adjustable in accordance with the greenhouse structure in general.

2.4. Kinematic analysis

In this study, the base frame and the end effector frame change places at every step of the robot. Thus, two different kinematic chains are used to obtain the kinematic equation of the robot [27]. Fig. 6 shows the robot kinematic configuration and axes defined for kinematic analysis.

Here, \mathbf{G} -axis set fixed to the body center of gravity can move freely in space with the body. The transformation matrix defining the configuration of the \mathbf{G} axis set according to the axis set $\hat{\mathbf{G}}$ which is located at any point in the robot's motion trajectory is given in equations 2-5. Here, T_{trans} is translational vector of these two axis sets. The rotation matrix $R_{r,p,y}$ denotes the orientation of the \mathbf{G} axis set with respect to the axis set $\hat{\mathbf{G}}$. And the

orientation is defined by the roll-pitch-yaw angular representation.

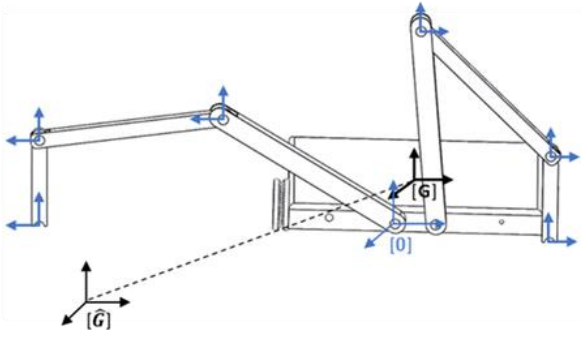


Figure 6. Placement of axis sets on the robot

$$T_{trans} = [x_{\hat{G}} \ y_{\hat{G}} \ z_{\hat{G}}] \quad (2)$$

$$R_p = \begin{bmatrix} \cos(\text{pitch}) & -\sin(\text{pitch}) & 0 \\ \sin(\text{pitch}) & \cos(\text{pitch}) & 0 \\ 0 & 0 & 1 \end{bmatrix} \quad (3a)$$

$$R_y = \begin{bmatrix} \cos(\text{yaw}) & \sin(\text{yaw}) & 0 \\ 0 & 1 & 0 \\ -\sin(\text{yaw}) & \cos(\text{yaw}) & 0 \end{bmatrix} \quad (3b)$$

$$R_r = \begin{bmatrix} 1 & 0 & 0 \\ 0 & \cos(\text{roll}) & -\sin(\text{roll}) \\ 0 & \sin(\text{roll}) & \cos(\text{roll}) \end{bmatrix} \quad (3c)$$

$$R_{r,p,y} = R_p * R_y * R_r \quad (4)$$

$$\hat{G}T_G = \begin{bmatrix} R_{r,p,y} & T_{trans}^T \\ 0_{[1 \times 3]} & 1 \end{bmatrix} \quad (5)$$

Subsequently, the configurations of the leg fixed axis sets according to the G axis set can be expressed as in

equation 6. Here, LF, RF, LR and RR represent the left front, right front, left rear and right rear legs respectively.

$${}^G_0T^{LF} = \begin{bmatrix} \cos(\frac{\pi}{2}) & 0 & \sin(\frac{\pi}{2}) & -\frac{d}{2} \\ 0 & 1 & 0 & 0 \\ -\sin(\frac{\pi}{2}) & 0 & \cos(\frac{\pi}{2}) & \frac{l_b}{2} \\ 0 & 0 & 0 & 1 \end{bmatrix} \quad (6a)$$

$${}^G_0T^{RF} = \begin{bmatrix} \cos(\frac{\pi}{2}) & 0 & \sin(\frac{\pi}{2}) & \frac{d}{2} \\ 0 & 1 & 0 & 0 \\ -\sin(\frac{\pi}{2}) & 0 & \cos(\frac{\pi}{2}) & \frac{l_b}{2} \\ 0 & 0 & 0 & 1 \end{bmatrix} \quad (6b)$$

$${}^G_0T^{LR} = \begin{bmatrix} \cos(-\frac{\pi}{2}) & 0 & \sin(-\frac{\pi}{2}) & \frac{d}{2} \\ 0 & 1 & 0 & 0 \\ -\sin(-\frac{\pi}{2}) & 0 & \cos(-\frac{\pi}{2}) & -\frac{l_b}{2} \\ 0 & 0 & 0 & 1 \end{bmatrix} \quad (6c)$$

$${}^G_0T^{RR} = \begin{bmatrix} \cos(-\frac{\pi}{2}) & 0 & \sin(-\frac{\pi}{2}) & -\frac{d}{2} \\ 0 & 1 & 0 & 0 \\ -\sin(-\frac{\pi}{2}) & 0 & \cos(-\frac{\pi}{2}) & -\frac{l_b}{2} \\ 0 & 0 & 0 & 1 \end{bmatrix} \quad (6d)$$

With a similar approach, the configurations of the axis set placed at the other joints of the legs can be expressed as in equation 7. Finally, the transformation matrices describing the configuration of the axes placed at the end points of the robot legs with respect to the G axis set can be found as in equation 8. Subsequently, the transformation matrices describing the configuration of the leg endpoints with respect to the 0 inertial axes set can be found as in equation 9. Thus, forward kinematic equations of the robot were obtained.

$${}^0_1T = \begin{bmatrix} \cos(\theta_{11}) & -\sin(\theta_{11}) & 0 & l_1 \cos(\theta_{11}) \\ \sin(\theta_{11}) & \cos(\theta_{11}) & 0 & l_1 \sin(\theta_{11}) \\ 0 & 0 & 1 & 0 \\ 0 & 0 & 0 & 1 \end{bmatrix} \quad (7a)$$

$${}^1_2T = \begin{bmatrix} \cos(\theta_{12}) & -\sin(\theta_{12}) & 0 & l_2 \cos(\theta_{12}) \\ \sin(\theta_{12}) & \cos(\theta_{12}) & 0 & l_2 \sin(\theta_{12}) \\ 0 & 0 & 1 & 0 \\ 0 & 0 & 0 & 1 \end{bmatrix} \quad (7b)$$

$${}^2_3T = \begin{bmatrix} \cos(\theta_{13}) & -\sin(\theta_{13}) & 0 & l_3 \cos(\theta_{13}) \\ \sin(\theta_{13}) & \cos(\theta_{13}) & 0 & l_3 \sin(\theta_{13}) \\ 0 & 0 & 1 & 0 \\ 0 & 0 & 0 & 1 \end{bmatrix} \quad (7c)$$

$${}^0_3T = {}^0_1T \ {}^1_2T \ {}^2_3T \quad (8)$$

$$\begin{aligned} {}^0P_x &= l_1 \cos(\theta_{11}) + l_2 \cos(\theta_{11} + \theta_{12}) + l_3 \cos(\theta_{11} + \theta_{12} + \theta_{13}) \\ {}^0P_y &= l_1 \sin(\theta_{11}) + l_2 \sin(\theta_{11} + \theta_{12}) + l_3 \sin(\theta_{11} + \theta_{12} + \theta_{13}) \end{aligned} \quad (9)$$

The answer to the inverse kinematic analysis problem, which seeks an answer to the question of what leg joint angles should be for a desired leg end point position $({}^0P_x, {}^0P_y)$ defined in the leg fixed axes set, is as in equation 9. Here, an inverse kinematic analysis has been carried out so that the last limbs of legs can hold the rails comfortably, so that the orientation of the last limb of legs always points towards the ground. For this reason, $\frac{3\pi}{2}$ value has been determined as a reference in the calculation of θ_{13} . Calculation of all three joint angles of the legs is obtained as in equation 10.

$$\cos(\theta_{13}) = (P_x^2(P_y + l_3)^2 - l_2^2) / 2l_1l_2 \quad (10a)$$

$$\sin(\theta_{13}) = \sqrt{1 - (\cos(\theta_{13}))^2} \quad (10b)$$

$$\theta_{11} = \text{atan2}(P_y + l_3, P_x) - \text{atan2}(k_1, k_2) \quad (10c)$$

Here, $k_1 = l_1 + l_2 \cos(\theta_{13})$ and $k_2 = l_2 \sin(\theta_{13})$

$$\theta_{12} = \text{atan2}(\sin(\theta_{13}), \cos(\theta_{13})) \quad (10d)$$

$$\theta_{13} = \frac{3\pi}{2} - \theta_{11} - \theta_{12} \quad (10e)$$

Here, the values for θ_{11} , θ_{12} and θ_{13} calculated for the left front leg, and these values are the same for the right front leg. For the rear legs, the variables θ_{21} , θ_{22} and θ_{23} are used, and in the calculation of these angles, since the structures of all legs are the same, the same inverse kinematic equations are used. However, in stage 2, the calculation of the angles of the joints of the hind legs is different with the calculation of the front legs. Because during this movement, the kinematic chain of the front legs and the rear legs are opposite [28]. In other words, in both leg groups, the calculation is made with the base axis set and the end axis set displaced.

The approach used to the walking strategy is discussed in the next section.

3. Results

3.1. Motion planning

In this section, motion planning of the robot is explained. The robot performs two basic movements on the greenhouse roof. The first is its movement with wheels on the iron bars while cleaning, which is relatively simple. During this movement, the robot moves forward or backward only along the iron bars with the help of wheels sitting on iron bars. In the other movement, the robot uses the legs it has to move to the other column after cleaning the column it is in.

The second movement, which is relatively complex, is planned in stages. It is desired that the orientation of the robot body does not change during the movement, because a simple but safe trajectory must be followed in order not to damage the additional components mounted on the robot for cleaning and to prevent the greenhouse glass from being damaged. In the rest of the section, the stages of movement planning for column change are explained in more detail. First of all, the legs end waiting

idle in a predetermined position should be fixed to the iron bars in order to carry the body during column change. For this, as a first stage, the legs (front legs) in the direction of the new column that the robot will pass through must be fixed to the next iron bar in the direction of movement. Also, at this stage, the other legs (rear legs) should be fixed to the iron bars where the robot is located in order to prepare the task of moving the robot body from wheels to legs.

In the second stage, when the task of moving the robot body passes to the legs, the legs must lift the robot body without changing its orientation and move it to the next column. In the final stage, the legs should return to their original position so that they do not interfere with work during the cleaning task. The kinematic equations of these stages and the determined trajectories are given below.

Stage 1

At this stage, the trajectory that the legs should follow is determined as shown in the figure. Since the trajectory definition is made according to the $\mathbf{0}$ axis set fixed to the first joint of the legs, the inverse kinematic solutions obtained in equation 10 is used at this stage. As stated in the previous section, an inverse kinematic analysis has been made so that the orientation of the last limb (l_3) of the leg along the trajectory is always pointing downward so that the last limbs can be fixed to the bars. In Figure 7 the trajectories of the leg end points in the first and third stages are given. Here, $\hat{\mathbf{0}}$ is located at any point in the trajectory of motion of the end point of the last limb of the legs.

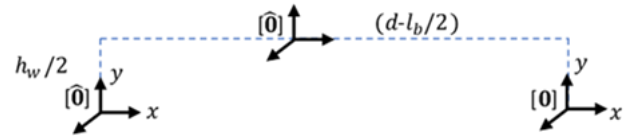


Figure 7. Legs end point trajectory of the robot

This trajectory consists of the movement of the leg joints in n_d steps. The position of the leg end point for each stage is calculated with equation 11. Where n_d is the number of steps ($n = 1 \dots n_d$). $\hat{}^0P_x^*$ and $\hat{}^0P_y^*$ are desired position of legs end points.

$$\begin{aligned} \hat{}^0P_x^*(n) &= {}^0P_x(n_d) - (n * (d - l_b/2)) / n_d \\ \hat{}^0P_y^*(n) &= {}^0P_y(n_d) - (n * h_w/2) / n_d \end{aligned} \quad (11)$$

Here, after the robot legs complete their movement in the y-axis, it starts its movement in the x-axis.

Stage 2

At this stage, the trajectory that the robot's body should follow is shown as in Figure 8. The trajectory

definition is made on the \mathbf{G} axis set fixed to the body, so that the spatial position of the robot body does not need to be followed continuously. With this approach, kinematic calculations can be made without the need to know the spatial position of the robot during column change and a general control approach can be obtained. Here, the most important points are that the trajectory that the trunk should follow must be defined on the \mathbf{G} axis set, the leg ends are fixed on the rails and the orientation of the body along the trajectory is fixed.

With this approach, the question of how the leg joints should change in order for the trunk to follow the desired trajectory should be answered while the positions of the leg end are fixed in space with respect to the \mathbf{G} axis set. For this, first the positions of the leg ends should be determined according to the \mathbf{G} axis set, then the inverse kinematic calculations should be made by calculating the positions in the $\hat{\mathbf{G}}$ axis set moved to any point on the trajectory.

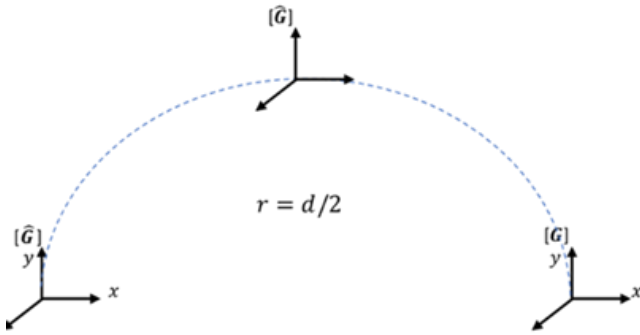


Figure 8. Body trajectory of the robot

The mathematical equivalents of these expressions are given in equations 12-18. An example of the location of the leg end points is shown for the left front leg (LF), and a similar calculation is made for the other legs. With Equation 12, the location of the leg end point with respect to the \mathbf{G} axis set is found.

$${}^G T^{LF} = {}^G T^{LF} * {}^0 T \quad (12)$$

\hat{P}_x^* and \hat{P}_y^* are desired position of robot body along the trajectory in Equation 13.

$$\hat{P}_x^* = (d/2) * (1 - \cos(n * \pi/n_d)) \quad (13a)$$

$$\hat{P}_y^* = (d/2) * \sin(n * \pi/n_d) \quad (13b)$$

Since there is no movement in z direction;

$$\hat{P}_z^* = 0 \quad (13c)$$

And the planar trajectory;

$$T_{trans} = [\hat{P}_x^* \ \hat{P}_y^* \ \hat{P}_z^*] \quad (14)$$

Thus, homogeneous transformation matrix in constant orientation is

$$\hat{T}_G = \begin{bmatrix} I_{[3 \times 3]} & T_{trans}^T \\ 0_{[1 \times 3]} & 1 \end{bmatrix} \quad (15)$$

Since the body is rigid;

$$\hat{G} T^{LF} = {}^G T^{LF} \quad (16)$$

In Equations 17-18, the location of the leg end point with respect to the $\hat{\mathbf{G}}$ axis set is found.

$$\hat{P}_3^{LF} = [\hat{G} T^{LF}]^{-1} * [\hat{T}_G]^{-1} * {}^G T^{LF} \quad (17)$$

$$\hat{P}_x^*(n) = \hat{P}_3^{LF}(1,4) \quad (18)$$

$$\hat{P}_y^*(n) = \hat{P}_3^{LF}(2,4)$$

Stage 3

At this stage, the inverse kinematic solutions obtained in equation 10 is used again. Since there are similar movements as in seen Figure 7, the approach in Stage 1 was followed in the action planning of this stage.

$$\hat{P}_x^*(n) = \hat{P}_x(n_d) + (n * (d - l_b/2) / n_d) \quad (19)$$

$$\hat{P}_y^*(n) = \hat{P}_y(n_d) + (n * h_w/2) / n_d$$

3.2. Walking simulation of the robot

The robot has two different movements on the greenhouse. One of these movements is carried out by four wheels on the robot body, which are driven by electric motors, on iron bars. This movement of the robot on the iron bars is realized only with the back-and-forth command given by the user. For this reason, this movement has not been simulated. Moving to the next column is a more important move. Which is the reason for the robot proposed in this study. This movement takes place with four legs. The results obtained from the simulation of this four-legged robot are given in this section. The physical properties of the robot used in the simulation are given in Table 1. These values can be changed for greenhouses with different dimensions.

Table 1. Cleaning robot specifications used in the simulation

Parameter	Dimensions [mm]						n_d
	d	h_w	l_b	l_1	l_2	l_3	
Value	550	200	50	400	400	100	20

The walking motion that the robot performs with four legs can be shown in three parts. When the robot moves on the rails with wheels, the four legs of the robot are in a position determined as the starting position as seen in Figure 9. First, the robot is fixed in a certain orientation of end limb on the iron bar in the next column by extending its two legs in the direction it should go. In the meantime, the two legs, which are opposite to the direction of movement of the robot, are fixed with a certain orientation to the iron bars on which the wheels closest to it are located.

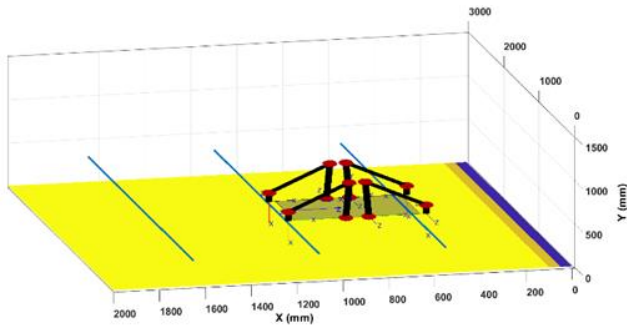
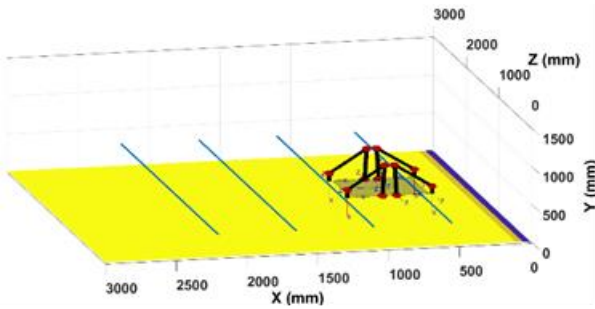
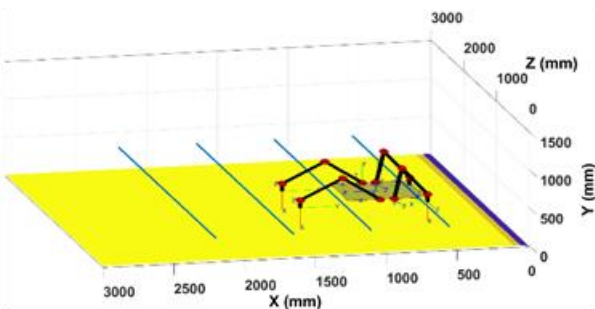


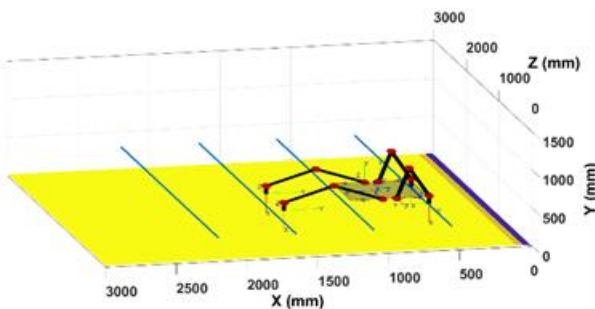
Figure 9. Starting position limbs of robot legs



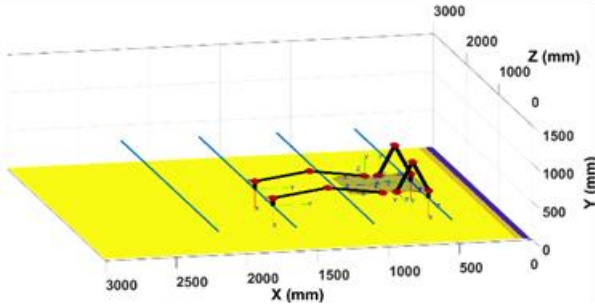
(1)



(2)



(3)



(4)

Figure 10. Stages of legs in first motion

After that, the robot's body is ready to move to the next column. The simulation images regarding this movement are given in Figure 10 in several steps.

The second movement is to move the robot body. In this walking movement, the two legs in the direction of the robot body move both by lifting and pulling the body of the robot, while the other two legs lift and push the body. These two movements occur synchronously without changing the angle of the robot body in any way. In the simulation, a trajectory is determined such that the robot body follows a half circle with a radius of 275 mm as seen in Fig. 8. In this walking action, the symmetry of the movement of the first two legs mentioned above is carried out by the other two legs.

Kinematically, these two groups of legs can be expressed as if the last limb and the first limb were replaced. The representation of this walking motion in eight states is given in Fig. 11 and Fig. 12.

The stages for this movement can be seen in Fig. 13. After the three stages of the robot's walking take place, the robot begins to move on the iron bars in the column it is located, by means of wheels, in order to clean the glass in the column where it is located.

4. Conclusion

In this study, a four-legged robot was designed and simulated for cleaning glass on the roof of greenhouses. The simulation study performed according to the mathematical model obtained showed that this proposed robot model can be used theoretically. This study, which focuses on the movement of the robot walking on the iron bars in order to pass to next column, also includes the movement of the robot with its wheels on the iron bars. However, since this movement is relatively simple and it is foreseen that it will be performed with the user command, it has not been emphasized much.

Four basic products have been found in the literature on robots and mechanisms designed or produced for glass cleaning. The first of these is the mechanisms that work with the principle of elevator on the building surface, developed for cleaning the glazed surfaces of high-rise buildings and the glazed parts of the windows.

The second is four-legged robots that can walk on vertical surfaces with the vacuum structure at their feet. The movement of these robots takes place by moving only one foot at each stage of walking. Using this walking strategy, the robot can move on this vertical surface without falling. Third, in which there is no walking motion, a rail structure is placed on the roof of the greenhouses, on which the washing mechanism can move with its wheels. The washing mechanism moves linearly on the rail on the roof of the greenhouse by performing the washing process towards the other end of the greenhouse. To clean the glass of another roof of the same greenhouse or the glass of the roof of another greenhouse, the rail structure and the washing mechanism must be reinstalled. Or, for this task, as many of these mechanisms as necessary should be installed for each roof and each greenhouse. The last one is robots developed for easier cleaning of dust on photovoltaic panels in solar power plants. These robots perform the cleaning task by moving on a fixed rail. Rail structure

installation is required in order to be used in a different solar power plant.

However, the robot proposed in this study can be used to clean glass on the roof of the greenhouse without any preliminary preparation. This robot can move between the grids in parallel with the determined walking strategy. For the cleaning task, by using the grids as a rail structure, it can move from the beginning to the end of the grid thanks to its wheels. The robot completes its task with these two basic movements. It has been designed with the motion strategy, which is a mixture of

robots and mechanisms mentioned above, presented in the literature. It has been seen by the carried-out design, analysis and simulation that this robot can be used for cleaning the glasses of greenhouse roofs.

This proposed robot can be improved by performing both dynamic analysis and mechanical optimizations. In addition, it can be understood that it can be a final product by conducting tests in real environments with an experimental study.

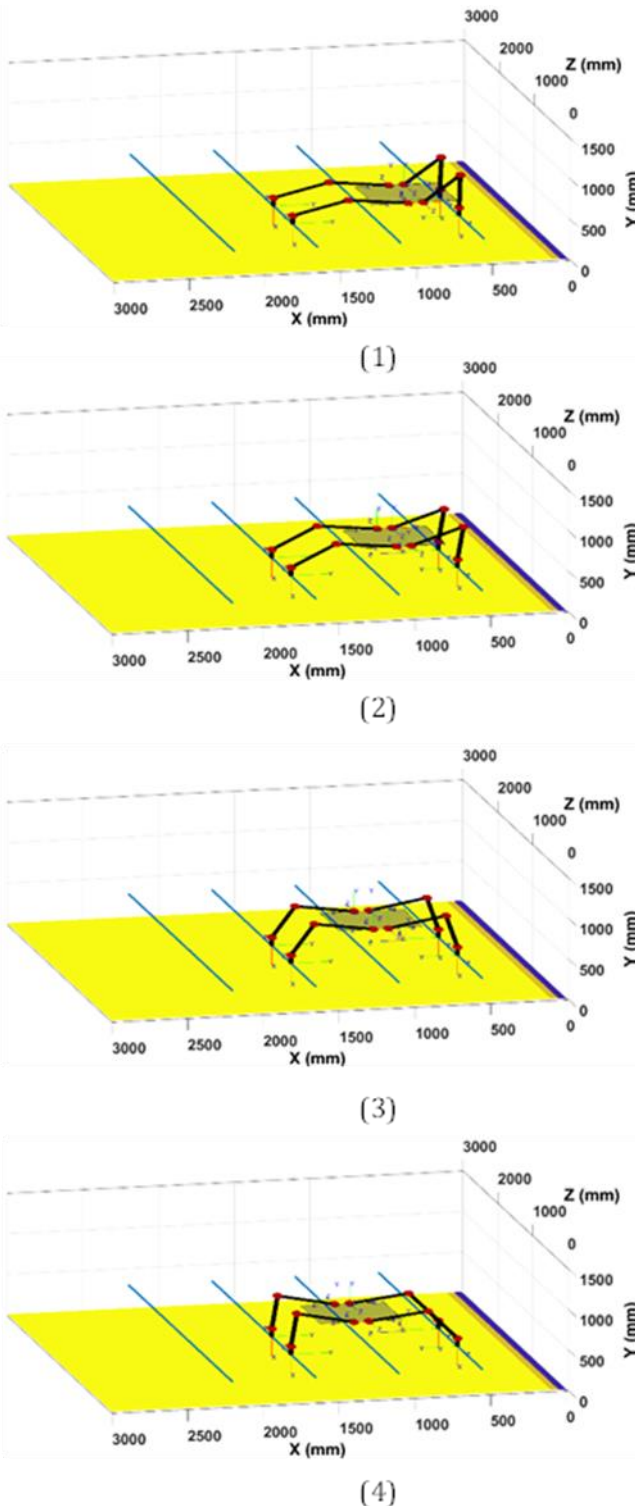


Figure 11. Walking states of robot for move body to next column (a)

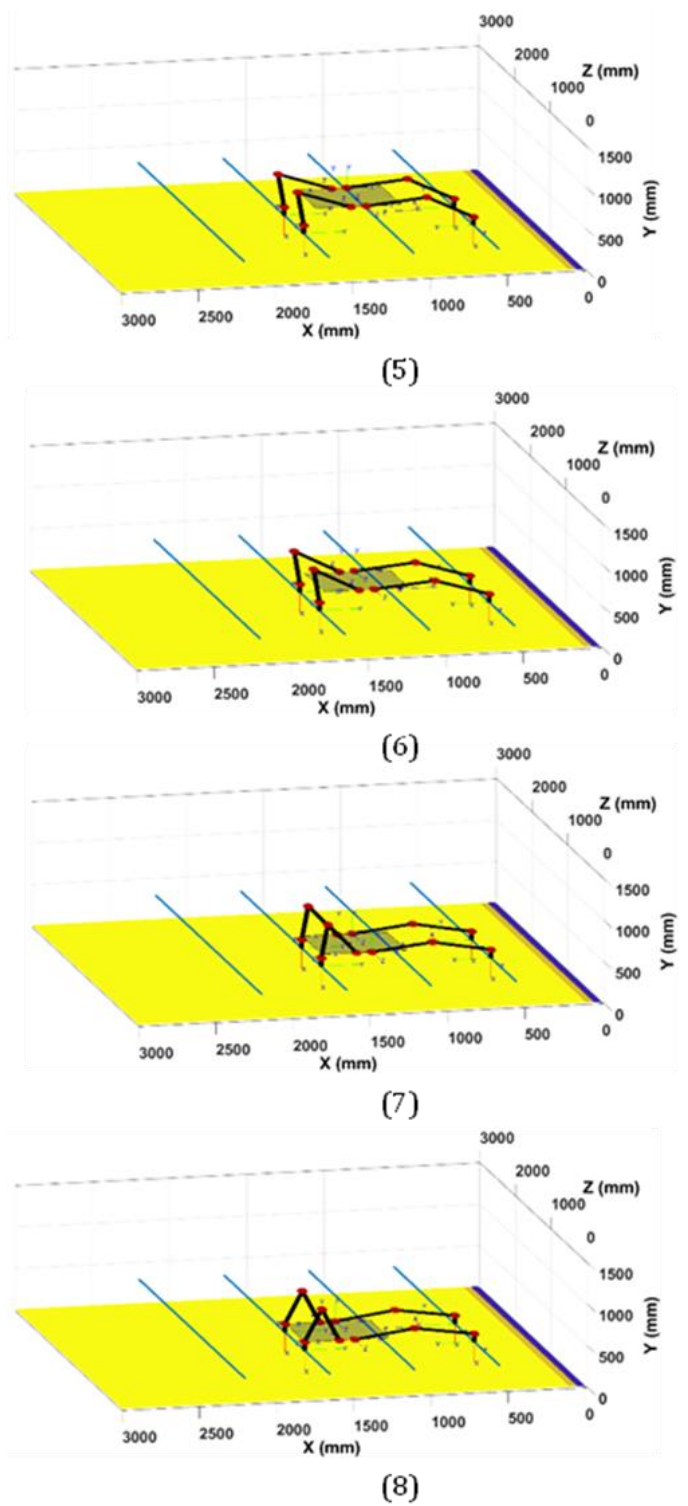


Figure 12. Walking states of robot for move body to next column (b)

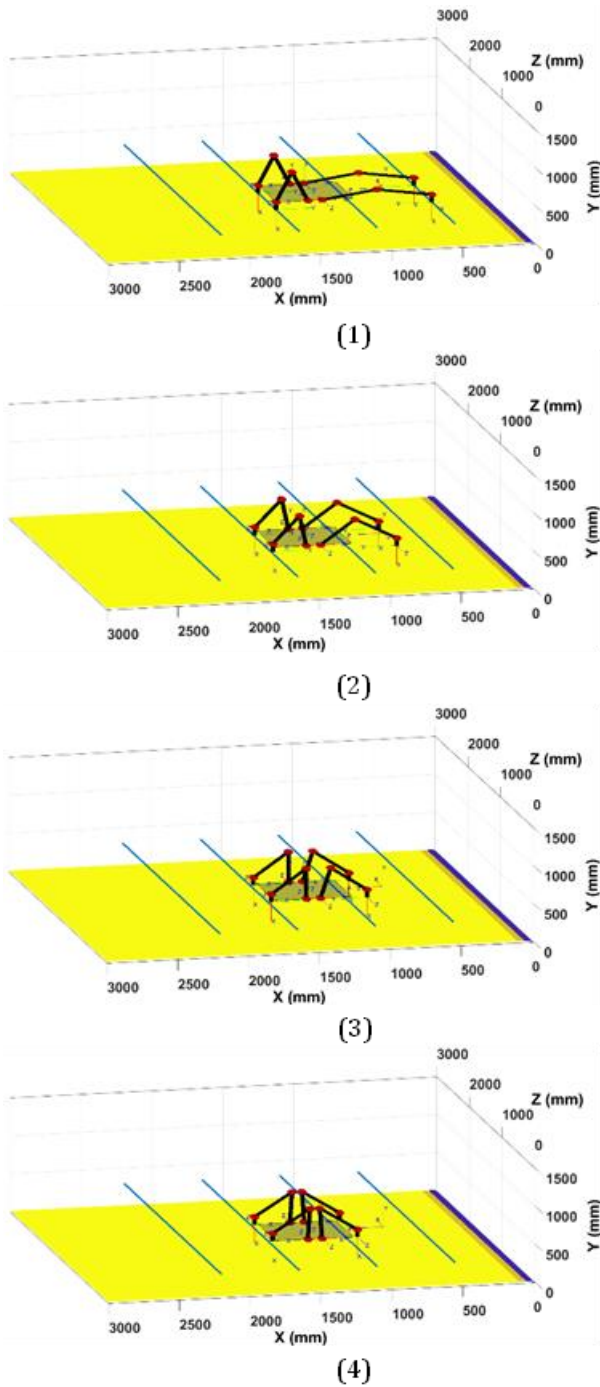


Figure 13. Motion stages of legs in last motion to arrive starting position

Conflicts of interest

The authors declare no conflicts of interest.

References

1. He, B., Cao, X., & Gu, Z. (2020). Kinematics of underactuated robotics for product carbon footprint. *Journal of Cleaner Production*, 257, 120491.
2. Li, J., Wang, J., Peng, H., Zhang, L., Hu, Y., & Su, H. (2020). Neural fuzzy approximation enhanced autonomous tracking control of the wheel-legged robot under uncertain physical interaction. *Neurocomputing*, 410, 342-353.

3. Li, J., Wang, J., Wang, S., Peng, H., Wang, B., Qi, W., Zhang, L., & Su, H., (2020). Parallel structure of six wheel-legged robot trajectory tracking control with heavy payload under uncertain physical interaction. *Assembly Automation*, 40, 675-687.
4. RunBin, C., YangZheng, C., Lin, L., Jian, W., & Xu, M. H. (2013). Inverse kinematics of a new quadruped robot control method. *International Journal of advanced robotic systems*, 10(1), 46.
5. Shim, H., Yoo, S. Y., Kang, H., & Jun, B. H. (2016). Development of arm and leg for seabed walking robot CRABSTER200. *Ocean Engineering*, 116, 55-67.
6. Wang, Z., Ding, X., Rovetta, A., & Giusti, A. (2011). Mobility analysis of the typical gait of a radial symmetrical six-legged robot. *Mechatronics*, 21(7), 1133-1146.
7. Yıldırım, Ş., & Arslan, E. (2019). A Comparison of six legged ODE (open dynamics engine) based gait control algorithm and standard walking gaits. *Avrupa Bilim ve Teknoloji Dergisi*, 242-255.
8. Chen, J., Qiang, H., Wu, J., Xu, G., & Wang, Z. (2021). Navigation path extraction for greenhouse cucumber-picking robots using the prediction-point Hough transform. *Computers and Electronics in Agriculture*, 180, 105911.
9. Tian, Y., Zhang, D., Yao, Y. A., Kong, X., & Li, Y. (2017). A reconfigurable multi-mode mobile parallel robot. *Mechanism and Machine Theory*, 111, 39-65.
10. Ayyıldız, M., & Çetinkaya, K. (2016). Comparison of four different heuristic optimization algorithms for the inverse kinematics solution of a real 4-DOF serial robot manipulator. *Neural Computing and Applications*, 27(4), 825-836.
11. Deng, H., Xin, G., Zhong, G., & Mistry, M. (2018). Object carrying of hexapod robots with integrated mechanism of leg and arm. *Robotics and Computer-Integrated Manufacturing*, 54, 145-155.
12. Ghergan, O. C., Țucu, D., Iusco, A., Drăghicescu, D., & Merce, R. M. B. (2019). Small greenhouse robotized solutions: state of the art and future perspectives. In *Proceedings of the 47th International Symposium, Actual Tasks on Agricultural Engineering, 5-7 March 2019, Opatija, Croatia* (pp. 267-276). University of Zagreb, Faculty of Agriculture.
13. Jia, B., Zhu, A., Yang, S. X., & Mittal, G. S. (2009, December). Integrated gripper and cutter in a mobile robotic system for harvesting greenhouse products. In *2009 IEEE International Conference on Robotics and Biomimetics (ROBIO)* (pp. 1778-1783). IEEE.
14. Roshanianfard, A., & Noguchi, N. (2020). Pumpkin harvesting robotic end-effector. *Computers and Electronics in Agriculture*, 174, 105503.
15. Ling, X., Zhao, Y., Gong, L., Liu, C., & Wang, T. (2019). Dual-arm cooperation and implementing for robotic harvesting tomato using binocular vision. *Robotics and Autonomous Systems*, 114, 134-143.
16. Martínez, D., Alenya, G., & Torras, C. (2015). Planning robot manipulation to clean planar surfaces. *Engineering Applications of Artificial Intelligence*, 39, 23-32.
17. Hong, J., Yoo, S., Joo, I., Kim, J., Kim, H. S., & Seo, T. (2019). Optimal parameter design of a cleaning device for vertical glass surfaces. *International*

Journal of Precision Engineering and Manufacturing, 20(2), 233-241.

18. Sun, D., Zhu, J., Lai, C., & Tso, S. K. (2004). A visual sensing application to a climbing cleaning robot on the glass surface. *Mechatronics*, 14(10), 1089-1104.
19. Antonelli, M. G., Zobel, P. B., De Marcellis, A., & Palange, E. (2020). Autonomous robot for cleaning photovoltaic panels in desert zones. *Mechatronics*, 68, 102372.
20. Li, T., Chen, D., Shi, G., Wei, M., Zhang, Y., & Chang, J. (2019). Analysis and suggestions of greenhouse cleaning machine in China and abroad. In *MATEC Web of Conferences* (Vol. 272, p. 01051). EDP Sciences.
21. Seemuang, N. (2017, April). A cleaning robot for greenhouse roofs. In *2017 2nd international conference on control and robotics engineering (ICCRE)* (pp. 49-52). IEEE.
22. Bakırcıoğlu, V., & Kalyoncu, M., (2019). A Literature Review on Walking Strategies of Legged Robots. *Journal of Polytechnic*, 0900, 961-986.
23. Çabuk, N., & Bakırcıoğlu, V. (2018). Altı serbestlik dereceli bir aydınlatma manipülatörünün yapay sinir ağları temelli ters kinematik çözümü ve benzetimi. *Gazi Üniversitesi Fen Bilimleri Dergisi Part C: Tasarım ve Teknoloji*, 6(1), 117-125.
24. Dewi, T., Nurmaini, S., Risma, P., Oktarina, Y., & Roriz, M. (2020). Inverse kinematic analysis of 4 DOF pick and place arm robot manipulator using fuzzy logic controller. *International Journal of Electrical & Computer Engineering*, 10(2), 1376-1386.
25. Pellicciari, M., Berselli, G., Leali, F., & Vergnano, A. (2013). A method for reducing the energy consumption of pick-and-place industrial robots. *Mechatronics*, 23(3), 326-334.
26. Şen, M. A., Bakırcıoğlu, V., & Kalyoncu, M. (2020). Three degree of freedom LEG design for quadruped robots and fractional order PID (PIλDμ) based control. *Konya Mühendislik Bilimleri Dergisi*, 8(2), 237-247.
27. Yildirim, Ş. (2008). Design of a proposed neural network control system for trajectory controlling of walking robots. *Simulation Modelling Practice and Theory*, 16(3), 368-378.
28. Yildirim, Ş. (2005). A proposed hybrid recurrent neural control system for two co-operating robots. *Journal of Intelligent and Robotic Systems*, 42(1), 95-111.



© Author(s) 2023. This work is distributed under <https://creativecommons.org/licenses/by-sa/4.0/>



Facile production of CsPbBr₃ perovskite single-crystals in a hydrobromic solution

Murat Özen^{*1}, Cansu Akyel¹, Songül Akbulut Özen²

¹Bursa Technical University, Department of Chemistry, Türkiye

²Bursa Technical University, Department of Physics, Türkiye

Keywords

CsPbBr₃
Perovskite
Single-Crystal
Wet Chemical Synthesis

Research Article

DOI: 10.31127/tuje.1018137

Received: 03.11.2021

Accepted: 31.03.2022

Published: 26.04.2022

Abstract

In this study, synthesis of CsPbBr₃ perovskite single-crystals in a hydrobromic solution was investigated. Single-crystal growth experiments were conducted at the solution-nucleation border at a constant temperature or controlled cooling conditions. Working at the solution-nucleation border poses some practical difficulties such as fast precipitation. Often researchers opt to oversaturate the solution and use the supernatant after filtration. However, for conditions where the A to B ratio in the precursor solution for the formation of ABX₃ is not 1, oversaturation is a waste of resources. In this work, precursor solutions were prepared for a particular working temperature and either held at a constant temperature or were gradually cooled to a predetermined temperature. The constant temperature method resulted in large and clear crystals as it reached saturation more slowly. Crystals prepared at high temperatures appeared to be more transparent with clear facets. Crystals prepared at low temperatures appeared to be opaque with multiple nuclei growth on a single-crystal. Seeding of the saturated solution resulted in larger single-crystals. The procedure adapted in this work made possible the production of clear CsPbBr₃ perovskite single-crystals in a hydrobromic acid solution with sizes of up to 5 mm in only 10 days.

1. Introduction

The need for room temperature operated X - and gamma-ray radiation detectors is becoming more and more important every day, not only for scientific purposes but also for our society. For example, radiation detectors may be used in nuclear (medicine) imaging, radioactivity monitoring, security etc. and are hence crucial for the welfare of modern society [1].

Present commercial semiconductor photodetectors, such as CdTe and CdZnTe, are designed from single-crystal ingots formed as a result of high heat treatments. Superior photodetector properties have been reported for perovskite materials with relatively high absorption, high resistivity, and high charge carrier-charge-life [1].

One of the most prominent perovskite materials that has been investigated for its optoelectronic effects are the hybrid organic perovskites. Although hybrid perovskites possess superior properties - such as large absorption coefficient, high charge carrier mobility, long

electron hole diffusion and tunable band gap - hybrid perovskites are known to be unstable at high temperatures due to the volatile nature of organic cations [2].

Inorganic perovskite materials such as metal lead halides (MPbX₃; M = Cs⁺, X = Cl⁻, Br⁻, I⁻) can be preferred for X-ray and gamma detectors due to their wide band gap (>2.0 eV) and large crystal production. Inorganic metal halide perovskites are emerging as an alternative to hybrid perovskites due to their chemical stability, wide energy range in the spectrum and tunable band gap [2].

Perovskite devices based on polycrystalline materials have low performances due to the existence of many voids, grains boundaries, and surface defect states inside the active perovskites layer. Single-crystal perovskites have been developed largely because of their low trap density and the absence of grain boundaries in them [3]. The need for large, high-quality single-crystalline

* Corresponding Author

^{*}(murat.ozen@btu.edu.tr) ORCID ID 0000-0002-3589-2059
(cansu.akyel@btu.edu.tr) ORCID ID 0000-0003-3509-998X
(songul.akbulut@btu.edu.tr) ORCID ID 0000-0001-8025-2141

Cite this article

Özen, M., Akyel, C., & Özen, S. A. (2023). Facile production of CsPbBr₃ perovskite single-crystals in a hydrobromic solution. Turkish Journal of Engineering, 7(2), 92-98

perovskites is essential to enable research into their practical applications.

Classical solid-state methods such as the Czochralski and Bridgman [4-6] are known to produce large crystals, but these techniques pose limitations such as phase-purity due to temperature dependent crystalline phase transformations. Another limitation of the solid-state methods is its relatively high processing temperature. In this regard, wet chemical methods may offer facile production of photodetector materials due to their low-temperature and ambient pressure conditions.

Centimeter-sized CsPbBr_3 single-crystal synthesis is possible at relatively low temperatures. The inverse temperature crystallization and antisolvent vapor crystallization methods are the most important of the solution-based methods. Dirin et al. [7] have developed several solution-based approaches for the growth of centimeter-scale perovskite single-crystals. Dirin et al. [7] reported the synthesis of CsPbBr_3 single-crystal with low-cost precursors under ambient atmosphere using the inverse temperature crystallization method. Dirin et al. [7] obtained orange, transparent perovskite single-crystals with a radius of 8 mm when the solution was heated to 90-100°C using different solvents such as acetonitrile and methanol in combination with dimethylsulfoxide. Rakita et al. [8] have reported procedures for growing pure CsPbBr_3 crystals of several millimeters in size from a precursor solution. Centimeter-sized single-crystals of CsPbBr_3 were synthesized by solvent-based methods, but it has significant structural defects that greatly reduce its electrical properties.

Hydrohalic solutions can provide easy production of high-quality single-crystal perovskites. Su et al. [9] obtained orange $\text{CH}_3\text{NH}_3\text{PbBr}_3$ single-crystals with sizes of roughly 5 mm produced over a period of 10 days by lowering the solution temperature from 70°C to 50°C. Dang et al. [10] successfully grew a 10 x 10 x 8 mm black and shiny crystal of $\text{CH}_3\text{NH}_3\text{PbI}_3$ at the bottom of the flask after a few days by lowering the solution temperature from 65°C to 40°C. Lian et al. [11] obtained small angular crystals of 3 mm in size by lowering the solution temperature from 100°C to 57°C. They fixed a single-crystal to a platinum wire end, placing it at the bottom of the precursor solution and grew a rhombic dodecahedral MAPbI_3 single-crystal with a size of 12 mm x 12 mm x 7 mm [11].

Hybrid perovskites have been successfully obtained from hydrohalic solutions. However, studies on CsPbBr_3 single-crystals grown in hydrohalic solutions are limited. Dirin et al. obtained CsPbBr_3 single-crystals with dodecahedral shape using Cs:Pb ratio of 1.45 in HBr solution [7]. Peng et al. [12] used an initial Cs:Pb precursor ratio of 1 in order to obtain CsPbBr_3 single-crystals in HBr. To the authors' knowledge, a detailed parametric study of CsPbBr_3 perovskite single-crystals in hydrohalic solutions is lacking in literature. In this study, the synthesis of CsPbBr_3 single-crystals in a hydrobromic solution was investigated. The cooling rate, the synthesis temperature, and the effect of seeded-growth were tested.

2. Method

2.1. Material

Precursor solutions were prepared by dissolving CsBr (99%, Alfa Aesar) and PbBr_2 (98+%, Alfa Aesar) in hydrobromic acid (HBr, aq. 48%, Carlo Erba). All experiments were carried out in an oil bath with precise temperature control on a magnetic hot plate stirrer with the help of thermocouples (See Fig. 1).

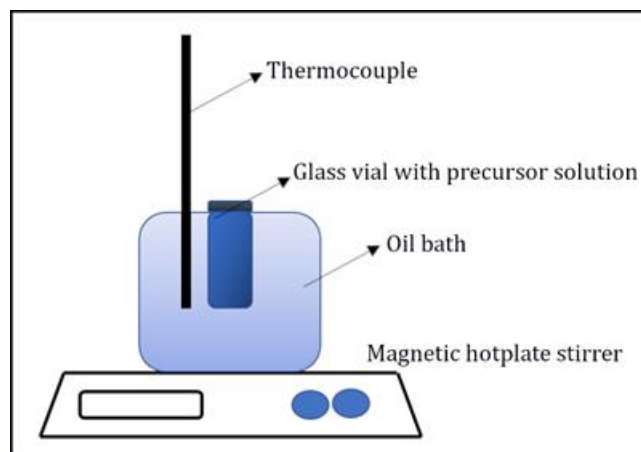


Figure 1. The precursor solution was prepared in an oil bath on a heated magnetic stirrer.

The phase diagram of PbBr_2 :CsBr compositions supports the formation of CsPb_2Br_5 , CsPbBr_3 , Cs_4PbBr_6 [8]. The stoichiometry must be precisely designed to ensure the specific formation of CsPbBr_3 and suppress all other phases. The chemistry behind the Cs to Pb ratio lies in the solubility of the respective ion or ion complexes. In order to reach the desired compositional phase, i.e., CsPbBr_3 , the molar amount of Cs ions – which has a relatively higher solubility in aqueous conditions – needs to be higher than the relatively less soluble Pb ions in aqueous conditions [7]. The Cs:Pb ratio was determined as 1.45 so that the resulting product could only be CsPbBr_3 . Thus, CsBr-rich or PbBr_2 -rich cesium lead bromide phases were avoided.

The synthesis process was finalized by washing the single-crystals with HBr (aq. 48%, Carlo Erba). Afterwards the products were dried and preserved in a desiccator.

2.2. Solubility Test

In order to work at the solution-nucleation border, solubility experiments of CsPbBr_3 were performed in hydrobromic acid by dissolving pre-prepared CsPbBr_3 single-crystals (1 mm and below) at varying temperatures between 30°C and 90°C. Experiments were conducted in glass vials. HBr solutions were heated by means of an oil bath. CsPbBr_3 single-crystals were added to HBr in steps of 0.02 g. The solution was assumed to reach saturation if the last added CsPbBr_3 crystal did not dissolve for 1 hour. The saturation limit was taken as the average weight of crystals added in the last two steps. The appropriate amount of precursor needed at a certain working temperature was determined using the solubility curve in Fig. 2.

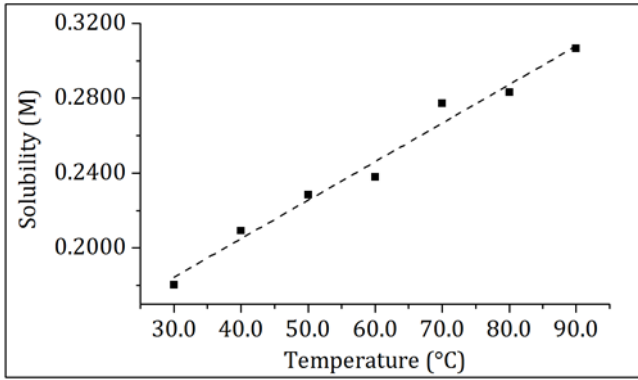


Figure 2. Solubility curve of CsPbBr₃ in HBr (aq. 48%)

2.3. Controlled Temperature Lowering Method

In the controlled temperature lowering method, the temperature of the precursor solution was lowered to the desired final temperature. The glass vial was sealed with a silicone stopper and heated in an oil bath above the saturation temperature. After the precursor was completely dissolved, the solution was cooled to the saturation temperature with a cooling rate of 0.05°C min⁻¹. Once the saturation was reached, the temperature was lowered at a rate of 0.005°C min⁻¹ to avoid multinucleation. The obtained single-crystals were washed with HBr (aq. 48%, Carlo Erba) and dried in a desiccator.

Controlled temperature lowering experiments were carried out at different starting temperatures.

2.4. Constant Temperature Method

In the constant temperature method, the precursor solution was kept at a constant temperature between 30°C and 90°C for a number of days.

2.5. Seeded Growth

In order to grow larger single-crystals, it is crucial to minimize the number of nuclei and use a seed crystal. Hence, a single-crystal of about 1 mm in size was added to a precursor solution and placed at the bottom of the glass vial. Seeded experiments were conducted for both the controlled temperature lowering and constant temperature methods.

2.6. Instrumental

X-ray diffractograms (XRD) were collected with a Bruker AXS/Discovery D8 diffractometer using a Ni-monochromator and Cu-K α radiation ($\lambda=0.1540598$ nm). The tube voltage and the tube current were set at 40 kV and 40 mA, respectively. The scan step size was 0.02 2 θ with 0.5 s per step.

Differential Scanning Calorimetry (DSC) thermograms were recorded under N₂ atmosphere from -75°C to 300°C with a rate of 10°C min⁻¹ using a TA/DSC25 instrument.

The Cs, Pb and Br contents in the prepared single-crystals were analyzed by a Rigaku supermini200X-ray Fluorescence (XRF) Spectrometer and a BrukerTM XFlash 61100 energy dispersive X-ray spectrometer (EDS) instrument.

The obtained CsPbBr₃ single-crystals were visually examined with a Leica M125 light microscope.

UV-VIS-NIR diffuse reflectance measurements of CsPbBr₃ single-crystals were measured in the 200-800 nm range using a SHIMADZU/UV3800 UV-VIS-NIR spectrophotometer. The sample was diluted (5 wt%) in barium sulfate and placed in the sample cup after obtaining a homogeneous mixture. The obtained reflection spectrum was calculated with the Kubelka-Munk equation (Eq.1). Diffuse reflection values were then plotted against the irradiated photon energy $h\nu$ (eV) values by Eq.2. The case where γ is 2 represents the allowed direct electron transfer. The electronic band gap E_g was calculated from the intersection of the linear part with the x-axis in the $(F(R_\infty)h\nu)^2$ versus $h\nu$ graph.

$$F(R) = \frac{(1 - R)^2}{2R} = \frac{K}{S} \quad (1)$$

$$(F(R_\infty)h\nu)^\gamma = A(h\nu - E_g) \quad \text{with } \gamma = 2 \quad (2)$$

3. Results and Discussion

Thermodynamically speaking, single-crystal formation and growth are promoted in a narrow solute concentration area at a specific temperature. By determining the required amount of precursor at a specific temperature, the formation of a single-crystal was aimed without the precipitation of multiple nuclei or polycrystals. For this reason, solubility plots were created for CsPbBr₃ crystals in HBr. The solubility graph that was obtained showed a linear relationship between CsPbBr₃ concentration with increasing temperature (Fig. 2).

Working at the solution-nucleation border does poses some practical difficulties such as fast precipitation. High solute concentrations favor the formation of CsPbBr₃ nuclei, though kinetically speaking dissolution-precipitation mechanisms should also be considered here. Often researchers opt to oversaturate the solution and use the supernatant after filtration. However, for conditions where the A (Cs⁺) to B (Pb²⁺) ratio in the precursor solution is not 1, oversaturation is a waste of resources. In this work, precursor solutions were prepared for a particular working temperature.

Single-crystal growth experiments were conducted at the solution-nucleation border at constant temperature or controlled temperature lowering conditions. The most important aspect of crystallization is undoubtedly temperature and the uniformity thereof. A slight deviation from the predetermined working temperature resulted in multiple nuclei formation. Single-crystal experiments are summarized in Table 1 and Table 2. All single-crystals that were obtained in this work were highly faceted with hexagonal morphologies.

One of the factors that determines the size of single-crystals is the solution's cooling rate. Nucleation is kinetically slowed down at slow heating rates, while high cooling rates trigger rapid nucleation [3]. In this study, multiple small nuclei were formed at relatively high cooling rates. Microscope pictures of CsPbBr₃ single-

crystals are shown in Table 1. At a rate of $0.005^{\circ}\text{C min}^{-1}$ multiple nucleation formation was inhibited and far less nuclei were formed.

Single-crystals that were obtained for experiments conducted from 80°C and 60°C to 40°C resulted in similar average sizes of about 3 mm. Crystal morphologies were hexagonal-shaped. The hexagonal facets were clearly formed for the crystal obtained by cooling from 80°C to 40°C . This was presumed to be due to the longer time spent in the solution. The number of nuclei formed at high starting temperatures were larger. An average of 5 nuclei were formed for the solution prepared by cooling from 60°C to 40°C , while this number was three times higher for the solution cooled from 80°C to 40°C . In both cases clear single-crystals were obtained, though defect formations were also observed. These defect formations are clearly visible in microscope images lit from below the crystal and were thought to be due to the solution's turbidity (see Fig. 3).

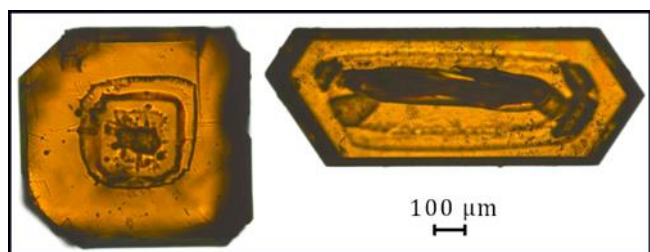


Figure 3. Light microscope images of selected few CsPbBr_3 single-crystals lit from below. Defect formations due to the solution's turbidity are clearly visible inside the single-crystals.

In the constant temperature method, the solution temperature was kept constant for 10 days at 80°C , 60°C and 40°C . Microscope pictures are shown in Table 2. Single-crystals of fairly similar size were obtained (3 mm) irrespective of the temperature. At relatively high temperatures (60°C and 80°C), single-crystal defects became visually apparent due to higher diffusion rates of the ions. Due to the relatively lower thermal energy at 40°C , the resulting single-crystal were clear with far less defects.

In the controlled temperature lowering method, even at extremely low cooling rate of $0.005^{\circ}\text{C min}^{-1}$ equilibrium was continuously disturbed with the potential of multiple nuclei formation.

Larger crystals can be grown by using seed crystals. Seed crystals must have similar crystalline composition as the desired material, i.e., CsPbBr_3 . CsPbBr_3 has the orthorhombic crystalline structure at the synthesis conditions. Large deviations from orthorhombic CsPbBr_3 will cause defects in the final single-crystal.

As previously mentioned, even at low cooling rates equilibrium was continuously disturbed and nucleation was triggered with the formation of multiple small single-crystals. However, less nuclei were observed for seeded experiments. The added seed inhibited the formation of additional nuclei. Furthermore, the final single-crystals were relatively larger compared to those in the unseeded experiments. Single-crystal sizes of up to 5 mm in average were observed for seeded experiments. At conditions where the solution temperature was

lowered from 80°C to 40°C , crystal defect structures were much more pronounced compared to experiments where the solution temperature was lowered from 60°C to 40°C . These differences were attributed to the higher thermal energies of ions in solutions at higher starting temperatures, resulting in more pronounced crystal habit planes.

In contrast, no foreign nuclei were formed for solutions seeded at constant temperature. The grown single-crystal was observed to have a similar morphology to the added seed material. Hence, a good crystalline conformity was obtained between the seed and the final product.

Comparing both the controlled temperature lowering and constant temperature methods, nucleation was observed to be more controllable for constant temperature conditions with regard to the number of nuclei formed during the synthesis. Far less CsPbBr_3 nuclei (about 4 to 5) were formed at constant temperature conditions.

Seeded experiments resulted in the growth of the added seed. A seed crystal with a size of $2\text{ mm} \times 1\text{ mm} \times 1\text{ mm}$ reached a size of $3\text{ mm} \times 3\text{ mm} \times 1\text{ mm}$ when kept at 60°C for 10 days. When cooled from 60°C to 40°C (at $0.005^{\circ}\text{C min}^{-1}$) a seed crystal with a size of $2\text{ mm} \times 2\text{ mm} \times 1\text{ mm}$ grew to a size of $3\text{ mm} \times 2\text{ mm} \times 1\text{ mm}$ in 3 days, which amounted to an average growth of $0.7\text{ mm}^3\text{ day}^{-1}$. At higher temperatures, a seed crystal with a size of $1\text{ mm} \times 1\text{ mm} \times 1\text{ mm}$ reached to a size of $3\text{ mm} \times 2\text{ mm} \times 2\text{ mm}$ when kept at 80°C for 10 days. When cooled from 80°C to 40°C ($0.005^{\circ}\text{C min}^{-1}$), a seed crystal with a size of $2\text{ mm} \times 2\text{ mm} \times 1\text{ mm}$ grew to a size of $5\text{ mm} \times 5\text{ mm} \times 2\text{ mm}$ in only 5 days. This corresponded to a growth rate increase from $1.2\text{ mm}^3\text{ day}^{-1}$ to $9.2\text{ mm}^3\text{ day}^{-1}$. The seed growth rate proved to be faster in the temperature lowering method, especially at higher starting temperatures.

DSC measurement of a well-formed clear CsPbBr_3 single-crystal is shown in Fig. 4. Measurements were taken from -80°C to 300°C at a rate of $10^{\circ}\text{C min}^{-1}$. The first heating cycle (blue) was carried out to remove any possible residues on the sample. The second cooling cycle (red) clearly shows a distinctive peak concurrent with cubic to tetragonal crystal phase transformation (129.8°C) followed by an additional smaller peak, concurrent with the tetragonal to orthorhombic phase transformation at 85.8°C . The third and final heating cycle (green) confirms the crystal phase transformations observed in the second cycle, i.e., orthorhombic to tetragonal crystal phase transformation at 88.7°C and tetragonal to cubic phase transformation at 131.3°C [13]. The DSC graph confirms the phase-pure nature of the obtained CsPbBr_3 single-crystal. DSC measurements of the other CsPbBr_3 samples showed very similar results with clear phase transitions at about 130°C and 85°C .

CsPbBr_3 suffers greatly from phase transitions that occur from cubic to tetragonal at around 130°C and from tetragonal to orthorhombic phase at about 88°C , which can cause mechanical deformations [14]. This is especially true for solid-state procedures that are executed at relatively high temperatures. However, wet-chemical procedures with relatively low synthesis temperatures ($< 80^{\circ}\text{C}$) avoid these issues entirely.

Table 1. CsPbBr₃ single-crystals obtained by the controlled temperature lowering method with a rate of 0.005°C min⁻¹ and a Cs:Pb ratio of 1.45

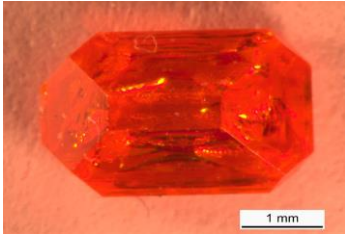
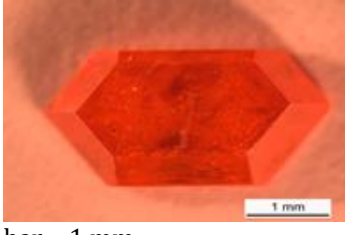
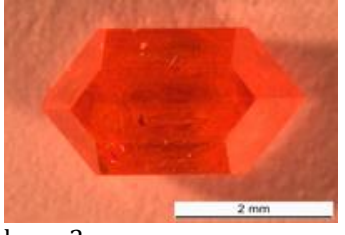
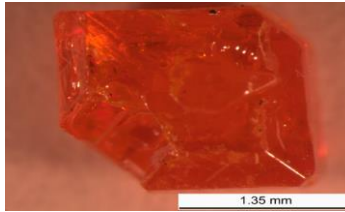
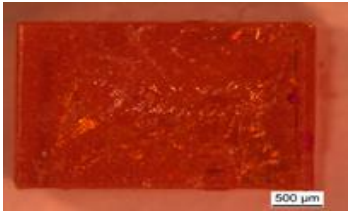
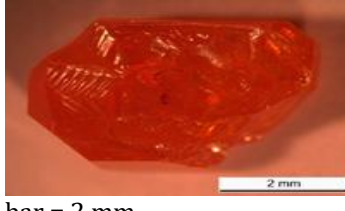
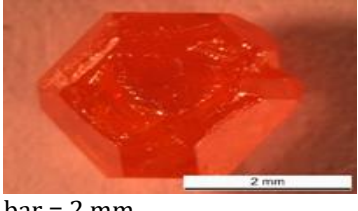
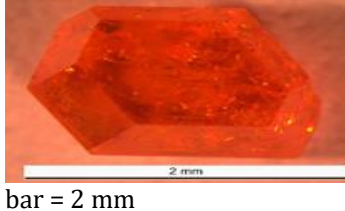
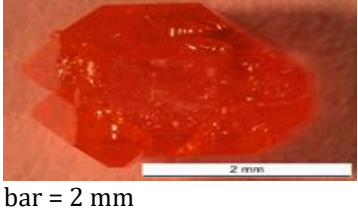
TEMPERATURE	TIME	[Cs] + [Pb]	SEEDLESS	SEEDED
80°C → 40°C	5 Days	0.283 M	 bar = 1 mm	 bar = 1 mm
60°C → 40°C	3 Days	0.235 M	 bar = 1 mm	 bar = 2 mm

Table 2. CsPbBr₃ single-crystals obtained by the constant temperature method with a Cs:Pb ratio of 1.4

TEMPERATURE	TIME	[Cs] + [Pb]	SEEDLESS	SEEDED
80°C	10 Days	0.283 M	 bar = 2 mm	 bar = 500 μm
60°C	10 Days	0.235 M	 bar = 2 mm	 bar = 2 mm
40°C	10 Day	0.2092 M	 bar = 2 mm	 bar = 2 mm

The XRD diffractogram of a CsPbBr₃ single-crystal is shown in Fig. 5. The XRD pattern was matched with QualX software [15] to orthorhombic CsPbBr₃ (COD database with ID 00-451-0745) [16]. XRF and EDS elemental analysis results for a CsPbBr₃ single-crystal did show the presence of a slight Cs-excess (Table 3) that, if not originating from the initial CsBr precursor (which is presumed to be washed away with HBr), might point to possible Cs-rich cesium lead bromide phases in the

final product. Furthermore, secondary cesium lead bromide phases were not detected in XRD (Fig. 5), but it should not be forgotten that the instrument's detection limit is about 5%. Any residual secondary phases such as Cs₄PbBr₆ that might have formed during the low temperature syntheses conditions were presumed to be washed away with HBr. XRD diffractograms of all samples matched with orthorhombic CsPbBr₃.

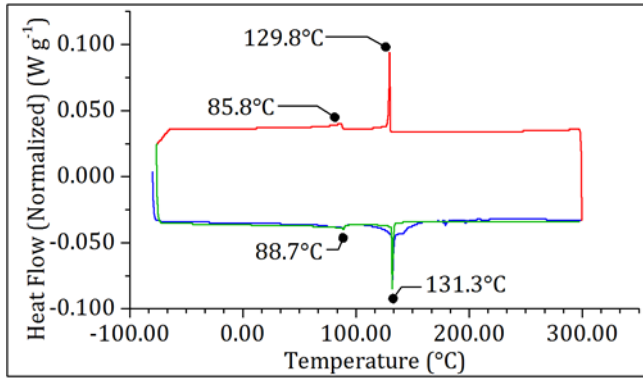


Figure 4. DSC plot of the sample prepared by cooling from 80°C to 40°C (seedless) (Blue plot: -80°C to 300°C, red plot: 300°C to -80°C, green plot: -80°C to 300°C. Measurements were taken at a rate of 10°C min⁻¹).

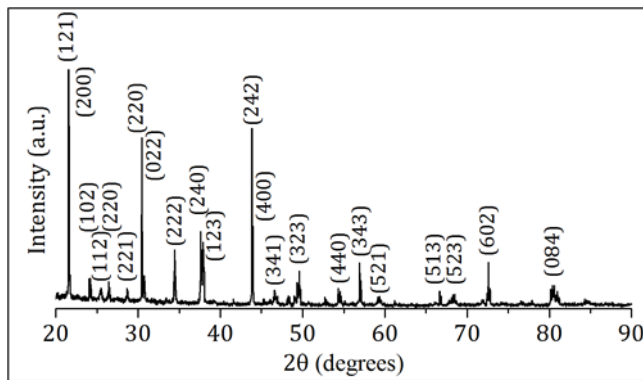


Figure 5. XRD diffractogram of the sample prepared by cooling from 80°C to 40°C (seedless). The pattern was matched with orthorhombic CsPbBr₃ (COD database with ID 00-451-0745) [16]

Table 3. XRF and EDS analysis results of obtained CsPbBr₃ single-crystal

Element	% Mole	
	XRF	EDS
Cs	13.4	17.62
Pb	11.8	16.47
Br	58.1	62.59

Although the XRF values were slightly lower than EDS, both techniques showed that Cs to Pb ratio was close to unity. Excess Cs found with both techniques could be due to the high Cs to Pb ratio (1.45) applied in the initial precursor solution. However, since the solutions were washed with HBr, excess CsBr or even PbBr₂ are unlikely to remain on the single-crystal.

UV-VIS-NIR diffuse reflectance spectroscopy result for a CsPbBr₃ single-crystal is given in Fig. 6. The band gap was calculated using the linear part of the Kubelka-Munk plot. The $F(R)hv^2$ plot has the typical S-like curve and is concurrent with allowed direct band gap semiconductor materials. The Kubelka-Munk plot intersects the x-axis at 2.26 eV, which is concurrent with literature values [17]. All other samples showed similar UV-Vis-NIR diffuse reflectance plots with band gap energies in the 2.2 ± 0.1 eV range. The Kubelka-Munk plot in Fig. 6 shows that CsPbBr₃ is suitable for absorption in the visible spectrum range and high energy photons.

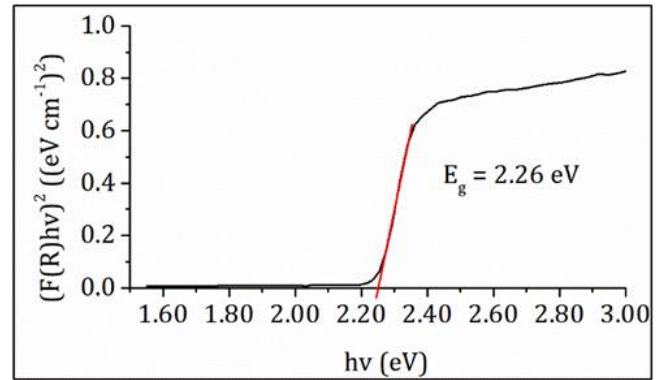


Figure 6. UV-Vis-NIR diffuse reflectance spectrometry measurement of the sample prepared by cooling from 80°C to 40°C (seedless). The linear part of the Kubelka-Munk graph intersects the x-axis at 2.26 eV.

4. Conclusion

To the best of the authors' knowledge, a parametric study on the growth of CsPbBr₃ perovskite single-crystals in HBr has not been reported previously. In this work, constant temperature and controlled temperature lowering techniques were used to grow highly faceted CsPbBr₃ single-crystals.

Multiple nuclei formation could only be avoided by a precise temperature control. Disturbances of equilibrium conditions such as non-uniform temperature distribution or fast temperature lowering rates resulted in multi-nucleation, i.e., more than one single-crystals. Also, high synthesis temperatures increased the turbidity resulting in defects as observed by light microscope. It has also been shown that seeded growth is possible without foreign nucleation.

The formation of phase-pure orthorhombic CsPbBr₃ single-crystals was ensured by using a Cs to Pb ratio of 1.45 in the precursor solutions. XRF and EDS showed Cs-excess that, if not originating from the initial CsBr precursor (which is presumed to be washed away with HBr), might be from a Cs-rich cesium lead bromide phase such as Cs₄PbBr₆. However, the presence of secondary cesium lead bromide phases (such as CsPb₂Br₅, Cs₄PbBr₆) were not detected in XRD or DSC, though, they could be present below the instruments' detection limits. The UV-Vis-NIR diffuse reflectance graph is compatible with a semiconductor direct band gap. The band gap of 2.6 eV, which is consistent with literature, shows that it is suitable for the absorption in the visible region.

High quality CsPbBr₃ single-crystals are needed to understand the potential properties of CsPbBr₃. In this context, the parametric study done in this work offers deeper insight in the chemistry of single-crystal growth. Future research should focus on the growth of plate-like, centimeter-sized, clear CsPbBr₃ single-crystals for high energy photon detector applications.

Acknowledgement

The research was funded by Bursa Technical University-Scientific Research Projects Fund under grant number 182N26 and 200Y015. The authors thank MERLAB Bursa Technical University for the EDS and XRD measurements.

Author contributions

Murat Özen: Data curation, Conceptualization, Writing-Reviewing. **Cansu Akyel:** Data curation, Writing-Original draft preparation, Investigation. **Songül Akbulut Özen:** Visualization, Editing

Conflicts of interest

The authors declare no conflicts of interest.

References

1. Stoumpos, C. C., Malliakas, C. D., Peters, J. A., Liu, Z., Sebastian, M., Im, J., ... Kanatzidis, M. G. (2013). Crystal Growth of the Perovskite Semiconductor CsPbBr₃: A New Material for High-Energy Radiation Detection. *Crystal Growth & Design*, 13(7), 2722–2727. <https://doi.org/10.1021/cg400645t>
2. Liang, J., Liu, J., & Jin, Z. (2017). All-Inorganic Halide Perovskites for Optoelectronics: Progress and Prospects. *Solar RRL*, 1(10), 1700086. <https://doi.org/10.1002/solr.201700086>
3. Tailor, N. K., & Satapathi, S. (2020). The impact of Cs₃Bi₂Cl₉ single crystal growth modality on its symmetry and morphology. *Journal of Materials Research and Technology*, 9(4), 7149–7157. <https://doi.org/10.1016/j.jmrt.2020.04.097>
4. Yu, J., Liu, G., Chen, C., Li, Y., Xu, M., Wang, T., ... Zhang, L. (2020). Perovskite CsPbBr₃ crystals: Growth and applications. *Journal of Materials Chemistry C*, 8(19), 6326–6341. <https://doi.org/10.1039/D0TC00922A>
5. Li, S., Zhang, C., Song, J.-J., Xie, X., Meng, J.-Q., & Xu, S. (2018). Metal Halide Perovskite Single Crystals: From Growth Process to Application. *Crystals*, 8(5), 220. <https://doi.org/10.3390/cryst8050220>
6. Dang, Y., Ju, D., Wang, L., & Tao, X. (2016). Recent progress in the synthesis of hybrid halide perovskite single crystals. *CrystEngComm*, 18(24), 4476–4484. <https://doi.org/10.1039/C6CE00655H>
7. Dirin, D. N., Cherniukh, I., Yakunin, S., Shynkarenko, Y., & Kovalenko, M. V. (2016). Solution-Grown CsPbBr₃ Perovskite Single Crystals for Photon Detection. *Chemistry of Materials*, 28(23), 8470–8474. <https://doi.org/10.1021/acs.chemmater.6b04298>
8. Rakita, Y., Kedem, N., Gupta, S., Sadhanala, A., Kalchenko, V., Böhm, M. L., ... Hodes, G. (2016). Low-Temperature Solution-Grown CsPbBr₃ Single Crystals and Their Characterization. *Crystal Growth & Design*, 16(10), 5717–5725. <https://doi.org/10.1021/acs.cgd.6b00764>
9. Su, J., Chen, D. P., & Lin, C. T. (2015). Growth of large CH₃NH₃PbX₃ (X=I, Br) single crystals in solution. *Journal of Crystal Growth*, 422, 75–79. <https://doi.org/10.1016/j.jcrysgro.2015.04.029>
10. Dang, Y., Liu, Y., Sun, Y., Yuan, D., Liu, X., Lu, W., ... Tao, X. (2015). Bulk crystal growth of hybrid perovskite material CH₃NH₃PbI₃. *CrystEngComm*, 17(3), 665–670. <https://doi.org/10.1039/C4CE02106A>
11. Lian, Z., Yan, Q., Lv, Q., Wang, Y., Liu, L., Zhang, L., ... Sun, J.-L. (2015). High-Performance Planar-Type Photodetector on (100) Facet of MAPbI₃ Single Crystal. *Scientific Reports*, 5(1), 16563. <https://doi.org/10.1038/srep16563>
12. Peng, J., Xia, C. Q., Xu, Y., Li, R., Cui, L., Clegg, J. K., ... Lin, Q. (2021). Crystallization of CsPbBr₃ single crystals in water for X-ray detection. *Nature Communications*, 12(1), 1531. <https://doi.org/10.1038/s41467-021-21805-0>
13. He, Y., Matei, L., Jung, H. J., McCall, K. M., Chen, M., Stoumpos, C. C., ... Kanatzidis, M. G. (2018). High spectral resolution of gamma-rays at room temperature by perovskite CsPbBr₃ single crystals. *Nature Communications*, 9(1), 1609. <https://doi.org/10.1038/s41467-018-04073-3>
14. Zhang, H., Wang, F., Lu, Y., Sun, Q., Xu, Y., Zhang, B.-B., ... Kanatzidis, M. G. (2020). High-sensitivity X-ray detectors based on solution-grown caesium lead bromide single crystals. *Journal of Materials Chemistry C*, 8(4), 1248–1256. <https://doi.org/10.1039/C9TC05490A>
15. Altomare, A., Corriero, N., Cuocci, C., Falcicchio, A., Moliterni, A., & Rizzi, R. (2015). QUALX2.0: A qualitative phase analysis software using the freely available database POW_COD. *Journal of Applied Crystallography*, 48(2), 598–603. <https://doi.org/10.1107/S1600576715002319>
16. Gražulis, S., Daškevič, A., Merkys, A., Chateigner, D., Lutterotti, L., Quirós, M., ... Le Bail, A. (2012). Crystallography Open Database (COD): An open-access collection of crystal structures and platform for world-wide collaboration. *Nucleic Acids Research*, 40(D1), D420–D427. <https://doi.org/10.1093/nar/gkr900>
17. Zhang, H., Liu, X., Dong, J., Yu, H., Zhou, C., Zhang, B., ... Jie, W. (2017). Centimeter-Sized Inorganic Lead Halide Perovskite CsPbBr₃ Crystals Grown by an Improved Solution Method. *Crystal Growth & Design*, 17(12), 6426–6431. <https://doi.org/10.1021/acs.cgd.7b010>



© Author(s) 2023. This work is distributed under <https://creativecommons.org/licenses/by-sa/4.0/>



Enhancing the seismic performance of high-rise buildings with lead rubber bearing isolators

Ahmet Hilmi Deringöl^{*1}, Esra Mete Güneyisi¹

¹Gaziantep University, Department of Civil Engineering, Türkiye

Keywords

Base isolation
High-rise building
Isolation period
Lead rubber bearing
Time-history analysis

Research Article

DOI: 10.31127/tuje.1026994

Received: 22.11.2021
Accepted: 10.04.2022
Published: 26.04.2022

Abstract

Recent earthquakes have enforced the engineering community to design seismically more efficient buildings through the energy dissipation systems. For this purpose, this paper investigates the seismic behavior of a high-rise building with a series of base isolation systems. Firstly, a 20-storey steel frame is selected as a fixed-base building, and then equipped with lead rubber bearings (LRBs). In the modelling of LRB, isolation period is alternatively varied as 4, 4.5, and 5 sec to evaluate the effectiveness of the isolator characteristic on the seismic performance of the high-rise base-isolated buildings. The seismic responses of the fixed-base and base-isolated buildings evaluated through a series of time-history analyses are performed using natural ground motion records. The analysis results are compared using engineering demand parameters such as storey displacement, isolator displacement, relative displacement, roof drift, interstorey drift ratio, absolute acceleration, base shear, base moment, input energy, and hysteretic curve. It is revealed that adjusting the isolation period in the design of LRB improved the seismic performance of the base-isolated high-rise steel buildings.

1. Introduction

The last devastating earthquakes in Turkey (e.g., Izmir 6.9 Mw, Malatya 5.7 Mw, Bingöl 5.9 Mw, Elazığ 6.8 Mw) reminded the expected major İstanbul earthquake that is to be 7+ Mw, resulted in the rupture of North Anatolian Fault, and caused thousands of fatalities and destructions [1]. Following the Marmara Earthquakes 7.4 Mw in 1999 that had struck off İstanbul, a series of legislative regulations/provisions on the seismic design codes were implemented through TEC (2007) [2] and TBEC (2018) [3]. The latter also includes the specifications for the base isolation systems (BIS). The increase of urbanization leads to the construction of high-rise buildings; however, they are much more susceptible to structural vibration under earthquakes and wind-induced seismic forces [4]. Likewise, the utilization of BIS for the retrofitting of existed buildings and designing of the newly structures significantly reduced the likelihood of casualties and structural damages during even major earthquakes and storms [5].

The idea behind the design of BIS is that decoupling the main structure from the foundation level and implementing a piece of flexible equipment made of either elastomeric or sliding bearings [6].

The BIS are generally categorized according to the energy dissipation mechanism namely rubber or friction-based bearings [7]. Among the former bearings, the lead rubber bearing (LRB) has favorable technique due to providing additional energy dissipation by lead core [8]. LRB is consisted of thin vulcanized steel plates, lead plug perpendicularly centered through the elastomeric rubber sheet as shown in Fig. 1 [9].

The isolator displacement demand of LRB depends on the shear modulus of the rubber material while the bearing capacity of the isolator is based on the vertical stiffness of the lead core consumed the external forces exerted by seismic actions [10]. The bilinear diagram represented in Fig. 2 can be constructed by two different models for rubber layer and lead plug of LRB. The former describes the linear viscoelastic behavior while the latter presents a linear elastic perfectly plastic model [11].

* Corresponding Author

(aderingol@gmail.com) ORCID ID 0000-0002-2665-8674
(eguneyisi@gantep.edu.tr) ORCID ID 0000-0002-4598-5582

Cite this article

Deringöl, A. H., & Güneyisi, E. M. (2023). Enhancing the seismic performance of high-rise buildings with lead rubber bearing isolators. Turkish Journal of Engineering, 7(2), 99-107

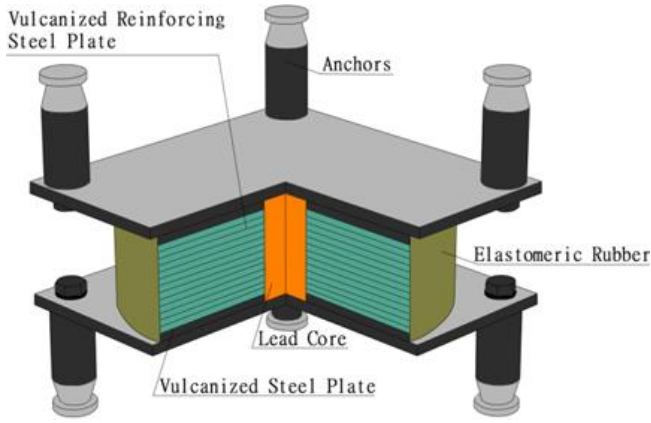


Figure 1. Typical configuration of LRB [9]

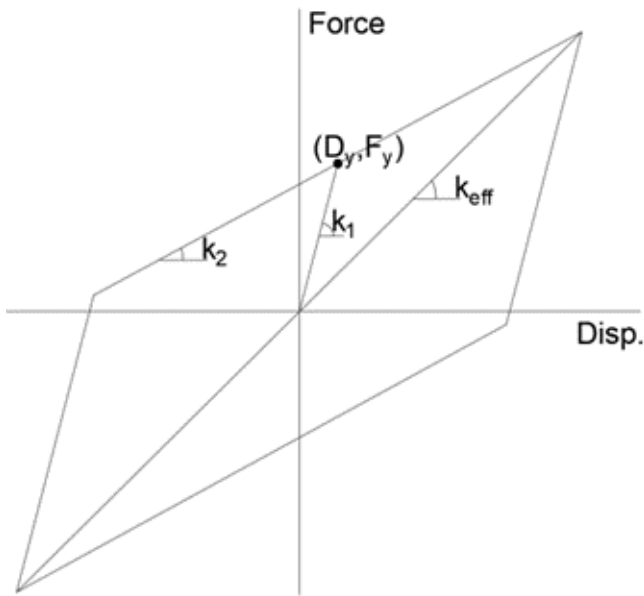


Figure 2. Hysteretic behavior of LRB isolator [11]

Many studies have been performed to the seismic performance of the base-isolated buildings with LRB. Kazeminezhad et al. [12], focused on the designing a new LRB model resisting all possible ground motions using performance point method in which a flowchart was presented to determine the isolation parameters by iterative procedure. The modified procedure decreased the base shear as 82 %. Deringöl and Güneyisi [13] evaluated the seismic performance of the regular and irregular frames with LRB considering such isolation parameters that effect the nonlinear response of the isolator. The use of proper LRB model significantly yielded the great interstorey drift reduction not only regular but also irregular frames. In the study of Shakouri et al. [14], the seismic performances of the base-isolated low and mid-rise buildings with LRB were evaluated trough time-history analyses considering the effect of ductility level and connection type. It was pointed out that both of them remarkably affected the maximum storey drift. But they recommended that the study should be extended for high-rise buildings. Ye et al. [15], proposed a design procedure based on the direct displacement method in order to satisfy the predefined displacement and drift values for the buildings with LRB. The flowchart was presented to simplify the application

steps of the methods. The reliability of the design method was proved using nonlinear time-history analysis whether a series of benchmark buildings with LRB reaching the target values. Gupta et al. [16] investigated the effect of vertical force of the earthquakes on the base-isolated buildings with LRB. The drawbacks such as amplification on the isolator and residual displacements were overcome with additional shape memory alloy bearings. Habib et al. [17], studied on the irregularities (i.e., heavy and soft storey) of the low-rise base-isolated buildings with LRB considering various PGA/PGV ratios of near-fault earthquakes. The soft storey model with lower PGA/PGV ratios introduced the better nonlinear response of LRB. Altalabani et al. [18] proposed a new novel LRB model in which typical form of bearing (i.e., cylindrical) modified as rectangular and increased the number of lead core was evaluated by the seismic reliability analysis. The rectangular type LRB attenuated the first vibration mode and decreased occurrence of the structural damage. Zhang and Li [19] experimentally assessed the loading rate behavior of LRB by means of shear, compression, and relaxation mechanical tests. The stiffness of LRB increased when implemented the shear test with the higher loading rate. Deringöl and Güneyisi [20] evaluated the influence of the damping ratio on the seismic performance of the base-isolated steel frames with rubber bearing through the nonlinear analyses. It was shown that the increase in the effective damping ratio decreased the interstorey drifts.

It can be observed from the previous literature review that LRB is capable of improving the the seismic response of low and mid-rise buildings. On the other hand, there have been limited studies on the conformity of the high-rise buildings with base isolation systems examining the favorable isolation parameters which is still scarce subject especially for LRB. Therefore, this study focused on the effectiveness of LRB characterized with different isolation parameters to design seismically more effective base-isolated high-rise steel buildings. To this, 20-storey steel frame considered as a benchmark fixed-base building, and then upgraded with various LRB having a series of the isolation periods (e.g., $T = 4, 4.5,$ and 5 sec) are produced to enhance the nonlinear response of the high-rise buildings. The seismic performance of the fixed-based and base-isolated buildings are evaluated through nonlinear analyses using a set of earthquakes to compare the seismic response of the high-rise buildings with and without LRB. The obtained analysis results are elaborately presented in terms of engineering demand parameters.

2. Analytical modelling and nonlinear analysis

The considered case study building is 20-storey moment resisting frame originally designed by [21] as high ductility level convenient with Eurocode 8 [22]. The storey height and bay width of the frame are 3.2 and 8 m, respectively, while the height is 4 m at the ground level. The beam and columns are subjected to the gravitational loading, graded with S275 and S355, designed with W sections, respectively, and illustrated in Fig. 3. The first period of the building is 3.75 sec. The building is assumed to be designed with peak ground acceleration of 0.35 g

and constructed in ground type B. The building importance factor and behavior factor are to be II and 6.5, respectively. The inherent damping ratio is considered as 3 %.

20-storey frame considered as fixed-base and then isolated with LRB (see Fig. 3(a) and (b)) considering the relevant standards like [3,22,23]. According to ASCE [24] and FEMA 356 [25], the plastic hinge mechanism is assumed to be formed at nodes of the beam and column. In addition, the panel zones and rigid diaphragm constraints are imposed for each storey for distributing the lateral forces proportionally to the structural members in the design of steel MRF. The nonlinear response of the fixed-base frame characterized with the lumped plasticity method. The modelling of the fixed-base and base-isolated frames are performed through finite element program of SAP2000 (2017) [26]. LRB has steel plates centered at the top and bottom of the bearing, also includes alternating layers, steel shims, and lead core located mid of the elastomeric plate as shown in Fig. 1 [9]. Authors selected the LRB as base isolation systems since the elastomeric rubber material is capable of lateral flexibility, the lead core contributes to the energy dissipation, the inner steel shims support the upcoming immense axial loads from high-rise building [27]. In the design of the base-isolated frame, LRB are modelled with nonlinear link element of “Rubber Isolator” because it perfectly describes the bilinear response (see Fig. 2) of the base isolators as recommended by [28-29].

The isolation parameters of LRB were determined considering the iterative method presented by [30]. First, the isolator displacement was assumed while the yield displacement was omitted, and then the iteration was to be proceeded until reached the presumed displacement value. The post yield stiffness ratio, is the ratio of the post-yield stiffness (k_1) to the initial stiffness (k_2), considered as 21 convenient with the study of [30]. LRB designed with isolation periods of 4, 4.5, and 5 sec. Thus, three base-isolated buildings have been developed to evaluate the isolator characteristics of LRB. The other isolation parameters were calculated and presented in Table 1.

Table 1. Properties of LRB for the outer columns of the base isolated frames

Variables	LRB (4 sec)	LRB (4.5 sec)	LRB (5 sec)
k_{eff} (kN/m)	1442.6	1139.8	641.1
W_d (kJ)	162.6	162.6	112.9
Q (kN)	119.4	106.1	66.3
k_2 (kN/m)	1097.4	867.1	487.7
D_y (mm)	5.4	6.1	6.8
D (m)	0.346	0.389	0.432
F_y (kN)	125.4	111.4	69.6

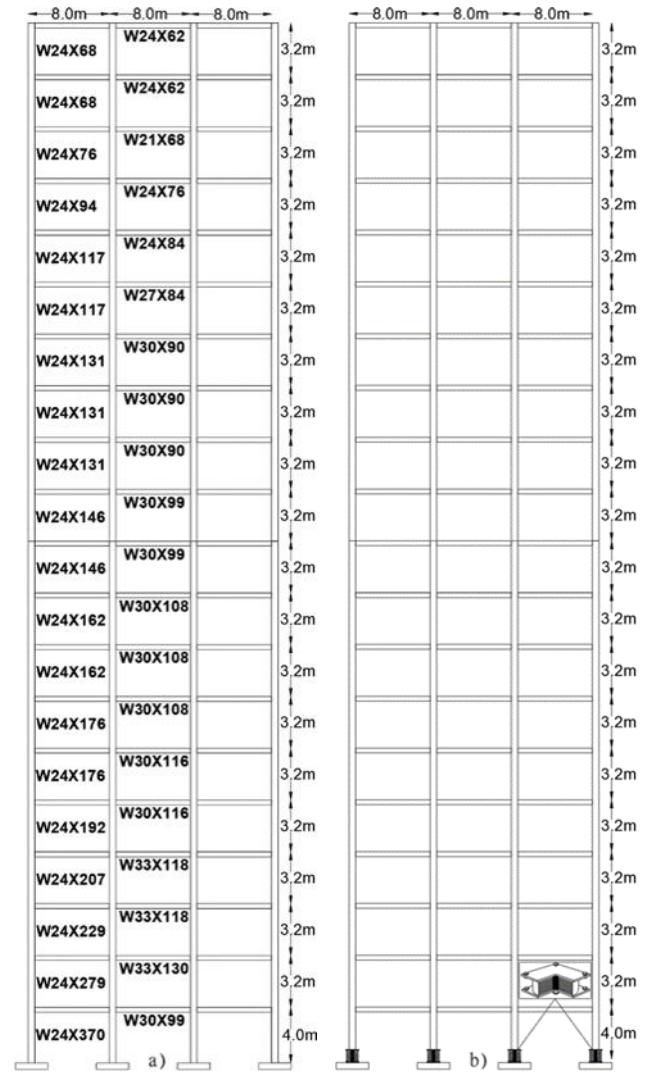


Figure 3. Elevation views of 20-storey; a) fixed-base [21] and b) LRB base-isolated frames

The force-displacement curve of the LRB (see Fig. 2) plotted by the following equations [30]

The effective stiffness, k_{eff} ;

$$k_{eff} = \frac{W}{g} \cdot \left(\frac{2 \cdot \pi}{T} \right) \tag{1}$$

hysteresis loop (the energy dissipated per cycle), W_D ;

$$W_D = 2 \cdot \pi \cdot k_{eff} \cdot \beta_{eff} \cdot D \tag{2}$$

characteristics strength, Q;

$$Q = \frac{W_D}{4(D - D_y)} \tag{3}$$

post-yield stiffness of the isolator, k_2 ;

$$k_2 = k_{eff} - \frac{Q}{D} \tag{4}$$

yield displacement, D_y is given by;

$$D_y = \frac{Q}{(k_1 - k_2)} \quad (5)$$

effective period, T_{eff}

$$T_{eff} = 2. \pi. \sqrt{\frac{W}{k_{eff} \cdot g}} \quad (6)$$

damping reduction factor, B ;

$$\frac{1}{B} = 0.25(1 - \ln\beta_{eff}) \quad (7)$$

displacement of isolation, D

$$D = \frac{g \cdot S_a \cdot T_{eff}^2}{B \cdot 4\pi^2} \quad (8)$$

and yield strength, F_y

$$F_y = Q + k_2 \cdot D_y \quad (9)$$

where target period is T , spectral acceleration is S_a , damping reduction factor is B , gravitational acceleration is g , characteristic strength is Q , total weight on the isolator is W , gravitational force is g , yield displacement is D_y , elastic stiffness is k_1 , post-yield stiffness is k_2 , and effective damping ratio is β_{eff} . The nonlinear response of the presented fixed-base and base-isolated high-rise steel frame models was evaluated by means of SAP 2000 (2017) by which the nonlinear time-history analyses were carried out with direct integration method. The earthquake records of Gazlı 1976, Tabas 1978, Cape Mendocino 1992, Chi-Chi 1999, and San Salvador 1986 presented in Table 2 were obtained from Pacific Earthquake Engineering Research Centre [31].

It is worthy to note that the force transmissibility of the LRB is an important issue and mainly depends on the ratio of dominating earthquake period to LRB base isolated building period. Based on the elastic design spectrum, the lengthening of the period could decrease the pseudo acceleration and therefore the earthquake induced forces in the buildings by increasing the deformation of the isolation systems. For the base isolation systems to be influential in diminishing the forces in the structures, isolated buildings period should be longer than the fixed base building period and similarly the dominant period of the ground motions [32].

Table 2. Characteristics of the ground motions used

Variables	Gazlı	Northridge	Chi-Chi	San Salvador	Supers. Hills
Year	1976	1994	1994	1987	1987
Station	Karakyr	Sylmar-Olive	TCU065	GeotechInvestig	Poe Road
Mechanism	Unknown	Reverse	R.-Oblique	Strike-Slip	Strike-Slip
M_w	6.8	6.69	7.62	5.8	6.54
R_{jb} (km)	3.9	0	0.6	2.1	0.9
R_{rup} (km)	5.5	5.3	0.6	6.3	0.9
V_{s30} (m/s)	659.6	251.2	305.9	545	348.7
PGA (g)	0.59	0.79	0.82	0.84	0.41
PGV (cm/s)	64.94	93.29	127.80	62.23	106.74
PGD (cm)	24.18	53.29	93.22	10.01	50.54

Note: M_w : Magnitude; R_{jb} : Surface projection distance; R_{rup} : Rupture distance; V_{s30} : Mean shear velocity over the top 30 m; PGA: Peak ground acceleration; PGV: Peak ground velocity; PGD: Peak ground displacement.

3. Results and Discussion

The seismic performance of the fixed-base and base-isolated high-rise steel buildings are investigated considering the effect of the isolation period on the nonlinear response of the lead rubber bearing through time history analyses. The analysis results are discussed in terms of storey displacement, isolator displacement, relative displacement, roof drift, interstorey drift ratio, absolute acceleration, base shear, base moment, input energy, and hysteretic curves.

20-storey fixed-base frame and base-isolated frame with LRB having the isolation periods of 4, 4.5, and 5 sec were tested through time history analyses within a series of ground motion records and those maximum storey

displacements were presented in Fig. 4. The maximum storey displacement of the fixed-base frame under Gazlı earthquake was recorded as 100.3 cm, but fortunately it was reduced up to 55.7, 52.7, 51.2 cm by means of LRB with 4, 4.5, and 5 sec, respectively. The reduction effect of LRB on the storey displacement demand of the fixed-base frame was also testified when subjected to Northridge, Chi-Chi, Salvador, and Hills earthquakes. For example, the greatest reductions of 49, 14, 24, 28, and 23 % were experienced when 20-storey base-isolated frame with LRB having isolation period of 5 sec subjected to Gazlı, Northridge, Chi-Chi, Salvador, and Hills earthquakes, respectively. Similarly, the average maximum storey displacement of the fixed-base frame is recorded as 102.64 cm while it was as 77.9, 76.1, and 74.2

cm for the base-isolated frame with LRB of 4, 4.5, and 5 sec, respectively. It was noted that the excessive storey displacements of the fixed-based frame were alleviated by means of equipment of LRB having the greater isolation period.

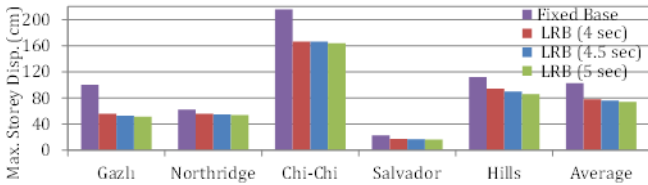


Figure 4. Maximum storey displacement of the case study frames under earthquakes

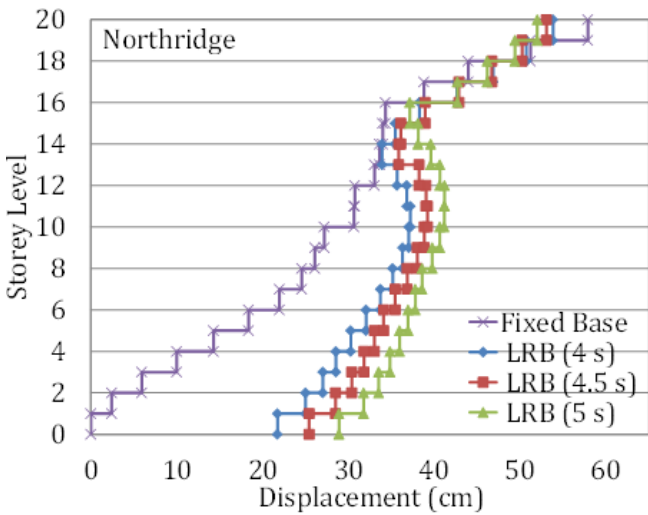


Figure 5. Variation of the storey displacement of the case study frames against storey height

The variation of the maximum storey displacements against storey height of high-rise frame with and without LRB under the effect of Northridge earthquake was illustrated in Fig. 5. The non-uniform storey distribution of the fixed-base frame was regulated if LRB was used. Compared to the lower isolation periods, LRB with 5 sec enhanced the storey displacement demand, in which the most uniform storey displacement pattern was experienced as well. However, the roof storey displacement of the fixed-base frame significantly reduced from 62.4 cm to 55.9, 54.9, and 53.7 cm corresponded to the reductions of 10, 12, 14 % for the isolation periods of 4, 4.5, and 5 sec, respectively.

The maximum isolator displacements of the base-isolated frames under earthquakes were presented in Fig. 6. The utilization of the greater isolation period in the design of LRB induced the lower stiffness for the bearing (see Table 1), thus the base-isolated frame can be easily swayed. For example, when subjected to Northridge earthquake, the maximum isolator displacements were obtained as 21.7, 25.4, and 28.9 cm for LRB with 4, 4.5, and 5 sec as shown in Fig. 6, those isolation periods corresponded to the effective stiffness of the bearing as 1442.6, 1139.8, and, 641.1 kN/m (see Table 1), respectively. As for the average maximum isolator displacement, similar trend was also recorded as 31.9, 35.4, and 38.5 cm (see Fig. 6), which was lower than the isolator displacement capacities as 34.6, 38.9, and 43.2

cm for LRB with 4, 4.5, and 5 sec (see Table 1), respectively.

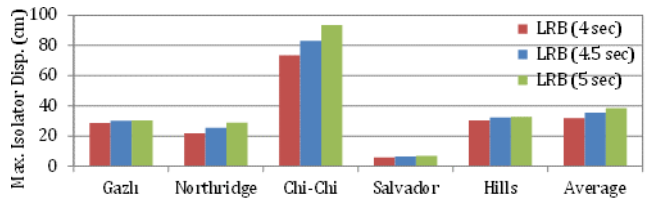


Figure 6. Maximum isolator displacement of the case study frames under earthquakes

The lateral displacement of any storey in the building with respect to the ground level was defined as relative displacement [33]. The maximum relative displacements of the case study frames were computed and presented in Fig. 7.

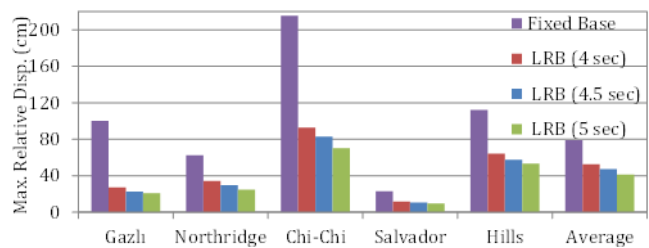


Figure 7. Maximum relative displacement of the case study frames under earthquakes

The utilization of LRB with 4 sec mitigated the excessive relative displacement of the fixed-base frame from 100.3 to 27.2 cm (73 %), 62.4 to 34.2 cm (45 %), 215.4 to 92.7 cm (57 %), 22.9 to 11.8 cm (48 %), 112.1 to 64.2 cm (42 %), furthermore the greatest reductions of LRB with 5 sec were recorded as 80, 60, 67, 58, and 53 % under Gazlı, Northridge, Chi-Chi, Salvador, and Hills earthquakes, respectively. The variation of the relative displacement height of the case study frames under Northridge earthquake was presented in Fig. 8. The relative displacements on the roof storey were as 62.4, 34.2, 29.6, and 24.9 cm for the fixed-base frame, isolated frame with 4, 4.5, and 5 sec, respectively. It can be seen LRB with the greater isolation period performed not only the more uniform pattern but also the lower relative displacement.

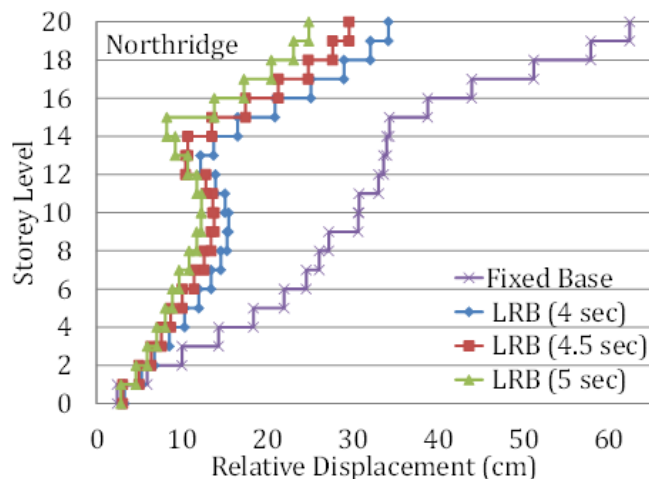


Figure 8. Variation of the relative displacement of the case study frames against storey height

The interstorey drift ratio is a significant index diagnosed the seismic performance of the buildings, which can be computed by subtracting the displacements of the adjacent storey and normalized by the storey height [34]. The maximum interstorey drift ratios of the fixed base frame and isolated frames with LRB were presented in Fig. 9. The former was as 2, 3, 2, 5, 1, and 4 % under Gazlı, Northridge, Chi-Chi, Salvador, and Hills earthquakes, however, they were reduced up to 1, 2, 3, 1, and 1 % by LRB with 5 sec, which corresponded to 64, 23, 44, 50, and 66 % reduction in the maximum interstorey drift ratio, respectively. Moreover, LRB with 4.5 sec provided the interstorey drift reductions as 56, 46, 21, 47, and 63 % compared to the fixed-base frame as shown in Fig. 8. The greatest reductions of 62, 63, and 66 % were observed when used LRB with 4, 4.5, and 5 sec under Hills earthquakes, respectively.

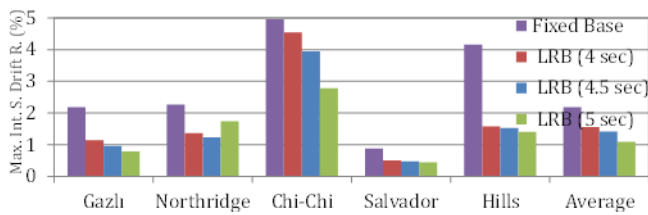


Figure 9. Maximum interstorey drift ratio of the case study frames under earthquakes

The effectiveness of the greater isolation period was also experienced in Fig. 10, which described the variation of the interstorey drift ratio with respect to the height of the case study frames under Northridge earthquake. The scattered interstorey drift pattern of the fixed-base frame was regulated by means of LRB. The most uniform interstorey drift ratio distribution was observed in LRB with the isolation period of 5 sec. The isolation period of 4.5 sec was tended to behave much more uniform trend especially in high-rise/upper storeys as shown in Fig. 10. It is worthy to note that the response of the structures under earthquakes depends on the fundamental period and the spectral acceleration of the ground motions corresponding to the periods, therefore, for different natural earthquakes varying responses were observed.

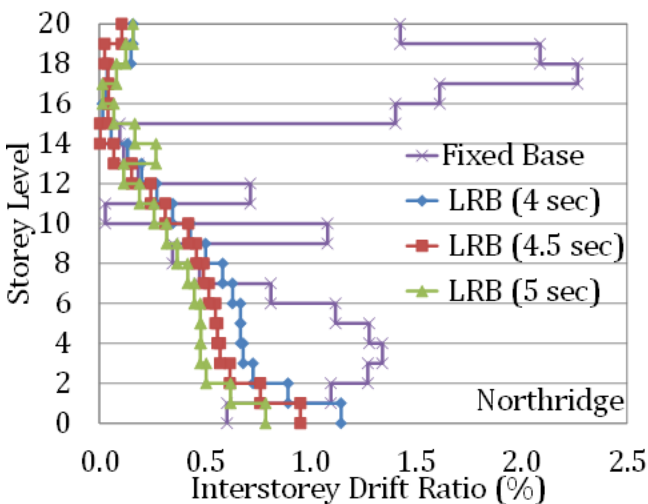


Figure 10. Variation of the interstorey drift ratio of the case study frames against storey height

The maximum absolute accelerations of the case study frames were given in Fig. 11. The fixed-base frame had by far the greatest absolute accelerations as 5.4, 7.2, 7.6, 9.1, and 6.4 m/s² when subjected to Gazlı, Northridge, Chi-Chi, Salvador, and Hills earthquakes, likewise they were reduced up to 3.7, 3.9, 3.5, 4.3, and 4.4 m/s², respectively, by means of LRB with 4 sec. The lowest maximum absolute acceleration of 2.8 m/s² was observed in case of LRB with 5 sec hit by Chi-Chi earthquake, which corresponded to 62 % reduction with respect to the considered fixed-base frame. It was as 54 and 59 % for LRB with 4 and 4.5 sec, respectively.

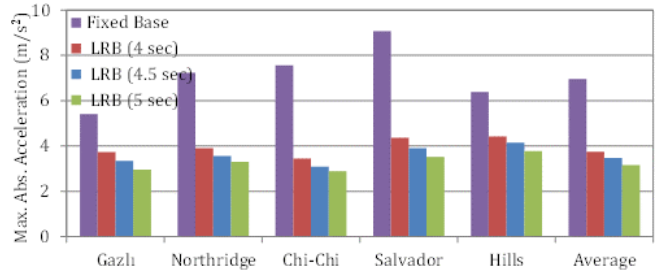


Figure 11. Maximum absolute acceleration of the case study frames under earthquakes

Fig. 12 described the variation of the absolute acceleration toward height of the case studied frames subjected to Northridge earthquake. Similar to the interstorey drift ratio variation, LRB having the greater isolation period tended to describe much more uniform absolute acceleration distribution. For example, the greatest storey acceleration was recorded as 7.2 m/s² at 14th storey, which mitigated to 2.1, 1.8, and 1.6 m/s² through LRB with 4, 4.5, and 5 sec, similarly, they performed the reductions as 39, 44, and 46 % at the roof storey absolute acceleration, respectively.

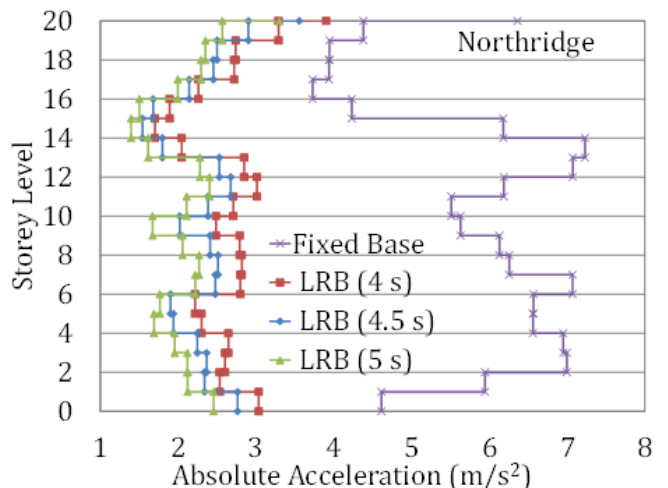


Figure 12. Variation of the absolute acceleration of the case study frames against storey height

The maximum base shears of the fixed base frame and isolated frames with LRB determined under earthquakes, and then normalized by building weight (32090 kN) were presented in Fig. 13. Compared to the fixed-base frame, LRB with 4 sec mitigated the base shears as 60, 63, 39, 66, and 54 %, and LRB with 5 sec satisfied the greatest reductions as 71, 68, 44, 73, and 67 % under Gazlı, Northridge, Chi-Chi, Salvador, and Hills

earthquakes, respectively. In addition, the average reductions were recorded as 54, 58, and 62 % through LRB with 4, 4.5, and 5 sec, respectively.

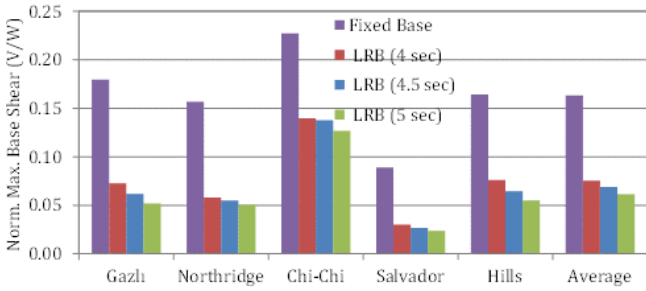


Figure 13. Maximum base shear of the case study frames under earthquakes

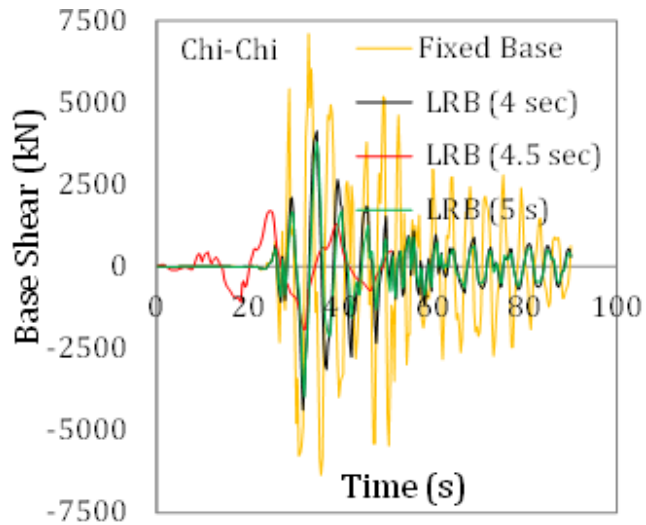


Figure 14. Time history response of base shear

The time history response of the base shear for the fixed-base frame and base-isolated frame with LRB having T of 4, 4.5, and 5 sec under the effect of Chi-Chi earthquake were presented in Fig. 14. The ranges of the base shear were observed to be between -6342 and 7097 kN, -4361 and 4139 kN, -4300 and 4194 kN, -3959 and 3807 kN for the fixed-base, LRB with 4, 4.5, and 5 sec respectively. It was shown that the utilization of the greatest isolation period was not only decreased the base shear but also narrowed the scatter time history response of the fixed-base.

Also, the maximum base moments were computed and presented in Fig. 15. Similar to the base shear demands, the use of LRB with 4 sec reduced the maximum base moment of the fixed-base frame as 57, 22, 30, 38, and 12 % when subjected to Gazli, Northridge, Chi-Chi, Salvador, and Hills earthquakes, while they were as 71, 27, 41, 50, and 25 % for LRB with 5 sec, respectively.

The input energy dissipated by regular structural members (beam, column) for fixed-base frame, while the most of the input energy nearly 90 % consumed by energy dissipation device for the isolated frame. Therefore, the input energy of the base-isolated frame was much lower than that of fixed-base frame [35]. The input energy of the fixed-base frame and base-isolated frame with LRB were determined under earthquakes and presented in Fig. 16. The input energy of the base-

isolated frames with LRB having greater isolation periods (i.e., 4.5 and 5 sec) was less than fixed-base frame and base-isolated frame with LRB of 4 sec. Compared to the fixed-base frame, LRB with 4.5 sec mitigated the input energy as 31, 18, 30, 20, and 8 % under Gazli, Northridge, Chi-Chi, Salvador, and Hills earthquakes, respectively. As for LRB with 5 sec, the reductions were 38, 20, 42, 22, and 16 %, respectively.

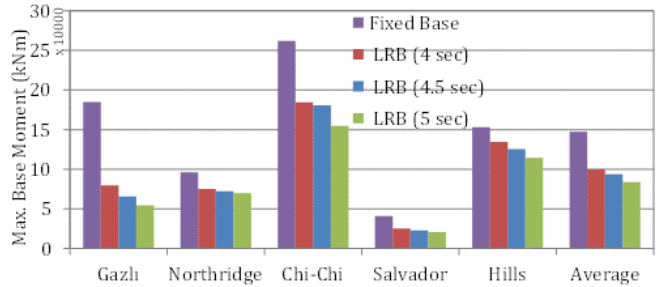


Figure 15. Maximum base moment of the case study frames under earthquakes

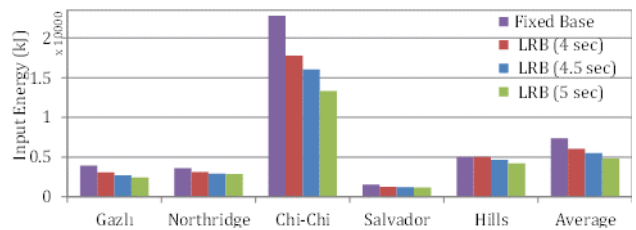


Figure 16. Input energy of the case study frames under earthquakes

When the fixed-base and base-isolated frames were hit by Chi-Chi earthquake, the time history responses of input energy were computed and presented in Fig. 17. The maximum input energies were recorded as 22808, 17767, 160033, and 13348 kJ for the fixed-base frame, base-isolated frame with LRB of 4, 4.5, and 5 sec, respectively.

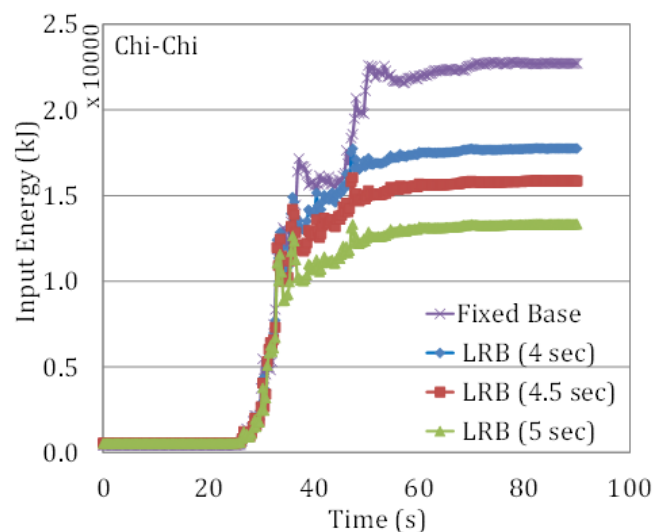


Figure 17. Time history response of input energy

The force-displacement cycles of the base-isolated frames with LRB of 4, 4.5, and 5 sec obtained through time-history analysis with Gazli earthquake were presented in Fig. 18. The hysteretic curve of outer LRB with 4, 4.5, and 5 sec produced the yield forces (F_y) as

122.4, 110.6, and 82.5 kN proved the design values of the bearings (see Table 1). The maximum forces of 417.5, 346.6, 298.3 kN and the maximum isolator displacements of 0.285, 0.292, and 0.299 m were experienced in the base-isolated frames with LRB of 4, 4.5, and 5 sec under Gazlı earthquake, respectively.

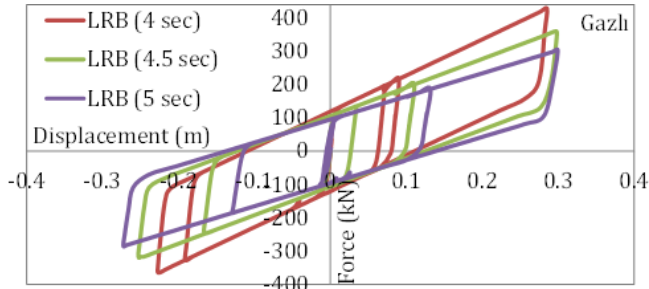


Figure 18. The force-displacement cycles of LRB with T of 4, 4.5, and 5 sec under Gazlı earthquake

4. Conclusion

Based on the results of the nonlinear analysis, a number of conclusions can be drawn as follows:

1. The use of greater isolation period reduced the lateral stiffness of LRB while the maximum storey displacements were significantly reduced. Compared to fixed-base frame, on average, the maximum displacement reductions occurred as 24, 26, and 28 % for the base-isolated frame with LRB of 4, 4.5, and 5 sec, respectively. The latter also successfully tended to behave the most uniform storey displacement.

2. The greatest average maximum isolator displacements were as 38.5 cm by the base-isolated frames with LRB of 5 sec.

3. The greatest reductions on the average maximum relative displacement were as 33, 40, and 48 % when high-rise frame isolated with LRB of 4, 4.5, and 5 sec, respectively. The greatest isolation period (T = 5 sec) presented the most uniform relative displacement distribution compared to the others.

4. The greater T not only reduced the maximum interstorey drift ratio but also showed the more uniform drift distribution. For example, LRB with T of 5 sec reduced in over half of the the average maximum interstorey drift ratio.

5. The use of LRB with 4, 4.5, and 5 sec mitigated the average maximum absolute acceleration as 46, 50, 55 %, respectively. LRB with T of 5 sec exhibited the best distribution pattern height of the base-isolated frames.

6. LRB with the greatest T was responsible both for mitigating the base shear and base moment as 62, 43 %, respectively.

7. The greatest average input energy mitigations of 18, 25, and 35 % were experienced when isolated with LRB with T of 4, 4.5, and 5 sec, respectively.

8. Among the ground motions, Chi-Chi being the most decisive earthquake revealed great difference response through LRB with 4, 4.5, and 5 sec, while Salvador earthquake was the steady.

9. The force-displacement cycles proved that the isolator could be displaced much more as T increased.

Author contributions

Ahmet Hilmi Deringöl: Conceptualization, Methodology, Software, Writing, Original draft preparation, Validation. **Esra Mete Güneysisi:** Visualization, Investigation, Writing-Reviewing and Editing.

Conflicts of interest

The authors declare no conflicts of interest.

References

- Murru, M., Akinci, A., Falcone, G., Pucci, S., Console, R., & Parsons, T. (2016). $M \geq 7$ earthquake rupture forecast and time-dependent probability for the Sea of Marmara region, Turkey. *Journal of Geophysical Research: Solid Earth*, 121(4), 2679-2707.
- TEC-2007, Turkish Earthquake Code, Ministry of Public Works and Settlement, Republic of Turkey, Ankara.
- TBEC 2018 – Turkish Building Earthquake Code 2018, Republic of Turkey Ministry of Interior Disaster and Emergency Management Presidency, Ankara, Turkey.
- Xu, Y., Becker, T. C., & Guo, T. (2021). Design optimization of triple friction pendulums for high-rise buildings considering both seismic and wind loads. *Soil Dynamics and Earthquake Engineering*, 142, 106568.
- Markou, A. A., Stefanou, G., & Manolis, G. D. (2018). Stochastic response of structures with hybrid base isolation systems. *Engineering Structures*, 172, 629-643.
- Skinner, R. I., Robinson, W. H., & McVerry, G. H. (1993). *An introduction to seismic isolation*. Wiley.
- Park, K. S., Jung, H. J., & Lee, I. W. (2002). A comparative study on aseismic performances of base isolation systems for multi-span continuous bridge. *Engineering Structures*, 24(8), 1001-1013.
- Kurino, S., Wei, W., & Igarashi, A. (2021). Seismic fragility and uncertainty mitigation of cable restrainer retrofit for isolated highway bridges incorporated with deteriorated elastomeric bearings. *Engineering Structures*, 237, 112190.
- Zordan, T., Liu, T., Briseghella, B., & Zhang, Q. (2014). Improved equivalent viscous damping model for base-isolated structures with lead rubber bearings. *Engineering Structures*, 75, 340-352.
- Ahmadipour, M., & Alam, M. S. (2017). Sensitivity analysis on mechanical characteristics of lead-core steel-reinforced elastomeric bearings under cyclic loading. *Engineering Structures*, 140, 39-50.
- Pant, D. R., Constantinou, M. C., & Wijeyewickrema, A. C. (2013). Re-evaluation of equivalent lateral force procedure for prediction of displacement demand in seismically isolated structures. *Engineering Structures*, 52, 455-465.

12. Kazeminezhad, E., Kazemi, M. T., & Mirhosseini, S. M. (2020). Modified procedure of lead rubber isolator design used in the reinforced concrete building. *Structures*, 27, 2245-2273.
13. Deringöl, A. H., & Güneyisi, E. M. (2020). Effect of lead rubber bearing on seismic response of regular and irregular frames in elevation. *Pamukkale Üniversitesi Mühendislik Bilimleri Dergisi*, 26(6), 1076-1085.
14. Shakouri, A., Amiri, G. G., & Salehi, M. (2021). Effects of ductility and connection design on seismic responses of base-isolated steel moment-resisting frames. *Soil Dynamics and Earthquake Engineering*, 143, 106647.
15. Ye, K., Xiao, Y., & Hu, L. (2019). A direct displacement-based design procedure for base-isolated building structures with lead rubber bearings (LRBs). *Engineering Structures*, 197, 109402.
16. Gupta, P. K., Ghosh, G., & Pandey, D. K. (2021). Parametric study of effects of vertical ground motions on base isolated structures. *Journal of Earthquake Engineering*, 25(3), 434-454.
17. Habib, A., Hourri, A. A., & Yildirim, U. (2021). Comparative study of base-isolated irregular RC structures subjected to pulse-like ground motions with low and high PGA/PGV ratios. *Structures*, 31, 1053-1071.
18. Altalabani, D., Hejazi, F., Rashid, R. S. B. M., & Abd Aziz, F. N. A. (2021). Development of new rectangular rubber isolators for a tunnel-form structure subjected to seismic excitations. *Structures*, 32, 1522-1542.
19. Zhang, R. J., & Li, A. Q. (2021). Experimental study on loading-rate dependent behavior of scaled high performance rubber bearings. *Construction and Building Materials*, 279, 122507.
20. Deringöl, A. H., & Güneyisi, E. M. (2021). Effect of Using High Damping Rubber Bearings for Seismic Isolation of the Buildings. *International Journal of Steel Structures*, 21(5), 1698-1722.
21. Karavasilis, T. L. (2016). Assessment of capacity design of columns in steel moment resisting frames with viscous dampers. *Soil Dynamics and Earthquake Engineering*, 88, 215-222.
22. CEN, C. E. D. N. (2004). Eurocode 8: Design of structures for earthquake resistance Part 1. *General rules, seismic actions and rules for buildings (EN 1998-1)*, Brussels.
23. American Society of Civil Engineers, ASCE. (2010). Minimum design loads for buildings and other structures. ASCE/SEI 7-10, Reston, VA.
24. ASCE 7-05. (2005). Minimum Design Loads for Buildings and Other Structures. American Society of Civil Engineers, Reston, Virginia.
25. FEMA (Federal Emergency Management Agency) (2000). Prestandard and commentary for the seismic rehabilitation of building. FEMA-356, D.C.
26. Computers and Structures, Inc. SAP 2000 v20.0.0 (2017). Static and dynamic finite element analysis of structures, Berkeley, California.
27. Markou, A. A., & Manolis, G. D. (2016). Mechanical models for shear behavior in high damping rubber bearings. *Soil Dynamics and Earthquake Engineering*, 90, 221-226.
28. Park, Y. J., Wen, Y. K., & Ang, A. H. S. (1986). Random vibration of hysteretic systems under bi-directional ground motions. *Earthquake engineering & structural dynamics*, 14(4), 543-557.
29. Wen, Y. K. (1976). Method for random vibration of hysteretic systems. *Journal of the engineering mechanics division*, 102(2), 249-263.
30. Naeim, F., & Kelly, J. M. (1999). *Design of seismic isolated structures: from theory to practice*. John Wiley & Sons.
31. PEER (2011). The Pacific Earthquake Engineering Research Center. User's Manual for the PEER Ground Motion Database Application. Berkeley: University of California.
32. Chopra, A. K. (1995). Dynamics of Structures: Theory and Applications to Earthquake Engineering. Englewood Cliffs, N.J: Prentice Hall.
33. Guan, Y., Zhou, X., Yao, X., & Shi, Y. (2020). Seismic performance of prefabricated sheathed cold-formed thin-walled steel buildings: shake table test and numerical analyses. *Journal of Constructional Steel Research*, 167, 105837.
34. Avila, L., Vasconcelos, G., Lourenço, P. B. (2018). Experimental study on loading-rate dependent behavior of scaled high performance rubber bearings. *Engineering Structures*, 155, 298-314.
35. Gajan, S., & Saravanathiiban, D. S. (2011). Modeling of energy dissipation in structural devices and foundation soil during seismic loading. *Soil Dynamics and Earthquake Engineering*, 31(8), 1106-1122.





An alternative method for the particle size distribution: Image processing

Mert Aydın ^{*1} , Talas Fikret Kurnaz ² 

¹ Mersin University, Department of Civil Engineering, Türkiye

² Mersin University, Department of Transportation Services, Türkiye

Keywords

Image processing technique
Particle distribution
Particle size
Sieve analysis

Research Article

DOI: 10.31127/tuje.1053462

Received: 04.01.2022

Accepted: 11.02.2022

Published: 26.04.2022

Abstract

Granular soils are used in different areas of civil engineering due to their easy accessibility and low cost as a material. The sieve analysis method, which has been conducted in rock physics measurements for many years, has been practicing determining the particle size distributions for those materials. In this study, a method based on image analysis technique has been developed as an alternative to traditional sieve analysis method for determining the particle size distribution in granular soils. This technique based on image processing to determine particle distributions via the experimental setup that consist of a camera, tripod, light box and mechanical shaking apparatus. In order to assess the reliability of this technique, each sample was subjected to traditional sieve analysis and the results of both analysis methods were compared. In conclusion, it was observed that the results obtained with the image processing technique had a minimum 95.22% closeness with the sieve analysis experiment data.

1. Introduction

Digital image processing method is simply the process of transferring the sample that willing to be analysed with an image capture instrument in a suitable format for digital media and by processing the raw image making it suitable for further analysis, and lastly collecting and storing the desired data. This method, whose foundations were laid with the examination of microscope images in the 1960s, has increased the areas of use day by day with the development of both computers and microscopes technologies. Digital image processing method has been used in many fields such as the analysis of cells, organelles, organisms in medical-based research, weather forecast in meteorology, the derivation of technologies such as fingerprint, retina scanning, night vision in the defence industry, tracking the habitats in environmental science, observing and controlling in industrial production lines [1-3].

Digital image processing technique within the scope of civil engineering has been used for various purposes since the 90's such as strength, permeability, compressibility of soils, shape parameters and deformations of materials, examining cross sections of concrete samples, measuring the maximum strength

non-destructively, correlating the performance of coatings with the materials used. Obaidat [4], aimed to measure void ratios of mineral aggregates in bituminous mixtures using image processing mechanism and planimeter. Gaydecki et al. [5], proposed to find the location of the reinforcements in the reinforced concrete samples, in a non-destructive way through image analysis. Soroushian et al. [6], used digital image processing techniques to detect voids and micro cracks in the concrete sample. Soroushian and Elzafraney [7], studied the microstructure of concrete samples with the images they obtained with scanning electron microscopy and fluorescence microscopy. Felekoğlu and Güllü [8], scanned clinker samples using an optical microscope and performed areal phase and porosity distribution analysis with image processing techniques. Sinha and Fieguth [9], investigated the usability of image processing techniques to detect deformations in concrete pipes used as infrastructure elements and developed algorithms to detect deformations in underground concrete pipes that can work with image processing techniques. Park et al. [10], aimed to develop an algorithm that allows the detection of air gaps with image processing technique by examining the colored images of the polished sections of concrete samples.

* Corresponding Author

^{*}(mertaydin180@gmail.com) ORCID ID 0000-0003-0620-0954
(fkurnaz@mersin.edu.tr) ORCID ID 0000-0003-2079-8315

Cite this article

Aydın, M. & Kurnaz, T. F. (2023). An alternative method for the particle size distribution: Image processing. Turkish Journal of Engineering, 7(2), 108-115

Granular materials are used in many areas due to their easy accessibility and low costs within the scope of civil engineering. They are being used as the main materials in both reinforced concrete and masonry structures, in addition to that they can be used for load transfer in steel and wooden structures. Concrete, one of the most common products, consists of aggregates between 60% -80% by volume, depending on the purpose of use. As result of that when evaluating the final strength of concrete, the importance of both physical and chemical parameters of the aggregate used reveals its importance. The wide area of usage of granular materials -in the scope of excavation / filling in various infrastructure and superstructure works, dam foundations and bodies, the leveling and filling area on bituminous hot-coated roads, applications such as jetcrete and grout in slope stabilization or tunnel applications- require the appropriate material selection. This selection happens with the help of a wide range of parameters such as specific gravity, chemical structure, mineralogical properties, permeability, cohesion values, internal friction angles [11-13]. The grain diameter size is the most common filter in making this kind of material selection. Sieve analysis method is used to determine the grain diameter distribution of grained materials. The sieve analysis, which has taken its final form today, is a universal method of classifying granular materials according to their size and weight. Testing procedures, that accepted by organizations such as ASTM, BS, AASHTO are being carried out with ISO standard equipment and instruments. The information which obtained from the sieve analysis results are the most important parameters in processing and classifying the grained material [14]. Some researchers have used image processing technique to determine grain diameter distributions as an alternative to the sieve analysis method, which can be described as relatively difficult and inconvenient. Yue et al. [15] studied the distribution, orientation and grain shape concepts of coarse particles in asphalt-added samples and concrete samples with the help of image processing technique. NG [16], studied the post-compaction microscopic structures of grained soils using the split element method. Masad and Button [17], examined the possibility of analyzing the grains' shape parameters with two different methods with using image processing technique by photographing the grained samples at different resolutions. Mora and Kwan [18], developed a method that analyzes the sphericity, convexity and shape parameters of the coarse aggregate using image processing technique. Yue et al. [19], used image processing techniques and the finite element method together to perform comprehensive analysis of two-dimensional shape of grained materials. Al Rousan [20], aimed to classify the grained materials according to their shape parameters with a computer-aided automation system. Alshibli and Alsalah [21], examined the sand soil samples under a microscope and statistically analyzed by their surface roughness, sphericity and roundness values. Yang [22], claimed that image processing researches in scope of soil mechanics were two-dimensional and aimed to make a three-dimensional analysis by filling the voids of the soil samples with epoxy. Hu et al. [23], researched the

behavior of clay fillings under dynamic compaction using image processing techniques. Edizer [24], explained the image processing technique comprehensively and performed grain size analysis with this technique by using an open-source software. Sezer [2], used image analysis techniques to determine the microstructural properties of granular soils. Önal (2008), developed algorithms to directly use image processing technique in the scope of geotechnical engineering. Vangla et al. [25], claimed that digital image processing technique for size and shape analysis of sand particles would be more consistent than traditional sieve analysis method. Ehsan et al. [26], used image processing techniques for grain size analysis of granular soils. Dipova [13], arranged a new experimental setup to examine the grain distribution of grained soils with the image processing technique.

In this study, digital image processing technique has used as an alternative to sieve analysis method for the determination of the particle distribution in granular soils. In order to capture the images, an experimental setup has developed and images have taken to determine the particle distribution of samples of different volumes and different origins. The same samples have examined by sieve analysis method and the results of the two methods have compared. Inspired by the extensive literature study and its predecessors, the experimental setup was arranged in the light of the antecedent theories and it was aimed to conduct an experimental study. By using a simple mechanism and user-friendly software, a system that is compatible with automation and does not require the intervention and interpretation of the user has been designed.

2. Image Processing Technique

Digital image processing is the examination of the image captured within the scope of the intended analysis by using a processor. The sample to be analysed has transferred to the digital environment under suitable conditions, with a suitable tool that allows analysis, in the desired file extension, with the desired visual properties (brightness, resolution, colour, contrast, etc.). The tool should be capable of capture images such as digital or analog cameras, microscopes, telescopes, and video recorders and transfer the captured image to the analysing environment. The captured image could be filtered by parameters such as colour, brightness, contrast, sharpness, size, if necessary. The purpose of this process is to eliminate noises on image that occurs during or post-image capturing phase and to prepare optimized input for analysis. Analysis has performed by existing software or algorithms developed by the user. In subjects such as classification, measurement, statistical studies, database creation; It is essential to use a purposeful analysis algorithm in this method, which can be used for several fields such as medicine, genetics, industry, electronics, textile and space research. For example, since cell organelles were willing to be examined, it was necessary to capturing images in microscopic dimensions, in black and white or colour according to the purpose to examine the organelle

shapes or textures and making comprehensive and appropriate choices for correct analysis results [24,27-29].

Image processing technology is the conversion of data into various readable format and processing after capturing, measuring and evaluating. The concept of image is defined as a two-dimensional function in the format "f (x, y)". Here, x and y values are representing coordinates, while f function represents the intensity of the parameter [30].

It could be said that the different stages of the digital image processing process take place together or independently from each other, that different targeted methods may be created and associated with algorithms. The method, which allows working multidisciplinary, also allows to include desired available parameters to the analysis.

3. Particle Size Distribution

Particles that have evaluated within the scope of the soil mechanics could be examined with the help of a naked eye or a magnifying glass over a diameter of 0.075 mm, while particles above this diameter are considered as coarse materials. Particles smaller than 0.075 mm in diameter have classified as fine grains. It is possible to examine the particles between 0.075 mm and 2 µm in diameter with the help of a microscope. Particles with a diameter range of 2 µm to 0.1 µm could also be examined with a microscope, but for accurate analysis of the texture and shape parameters of the grains, it is recommended to examine the particles under 1 µm particle diameter by electron microscope. Examination of the molecular structure of the particles is possible with X-ray analysis [2].

The part of the soil that could be classified as coarse consists of sand and aggregates. While gravels, which has defined as rock particles, may consist of one or more minerals, sand particles generally consist of a single mineral, quartz. When the particles of sand and gravel have examined in terms of shape details, they were divided into five sub-groups; angular, semi-angular, semi-round, round, fairly round. Silt and clay particles may be angular, flat or needle shaped.

The sieve analysis method is a widely used technique for determining the particle size distribution of granular materials. By the particle size distribution information of the soil sample, it is able to gauge properties of soil such as the water permeability, strength, compressibility of the soil, determination of capillary water movements, frost effect, compression speed under load.

The sieves used in the sieve analysis consist of square grids of equally spaced wires. The aperture size varies inversely with the sieve number [31]. Sieve analysis starts with stacking of sieves one on top of the other in decreasing aperture order. The sieve set has shaken uniformly for 15 minutes, preferably with the shaking device. The sample remaining on each sieve has weighed separately after shaking process. Precise shaking time is needed, the short shaking process does not allow small particles to pass into the lower sieves, on the other hand the long shaking process may cause deformation of the particles and deflects the results [31].

Even though particle size distributions are determined by sieve analysis method, there were still some uncertainties about the shape of the grains. The size of a spherical particle may be described in one dimension; however, the grains' shapes in the soil sample are generally irregular, not uniform. In a sieve analysis test, the size of a particle is related to the size of the square apertures at mesh which the particle passes through. Since all axial sizes of a particle cannot be measured and the shape of the particle is not taken into account, the method also has some limitations [32-36].

4. Materials and Methods

4.1. Soil Samples

Six different test samples from four different origins have created for the study (Figure 1). The samples have obtained from different regions of Mersin province (Turkey). The first three samples have consisted of crushed stones taken from Mersin/Silifke region. Three different samples containing different particle diameter ranges have prepared by separating them manually. Thus, soil batches with the same surface and shape parameters have examined in different particle diameter ranges. Sample No.4 has prepared with crushed stone taken from Mersin/Toroslar region, and this sample's shape parameters and surface texture distinguish itself from the first three samples. Sample No.5 is a white-colored, grained material have taken from marble quarries in Mersin/Erdemli region. By using this material, also known as mosaic powder, the suitability of image processing techniques for analysis of different colored materials has been investigated. The sixth sample contains particles that could be regarded as more round, taken from the Mersin/Adanalioğlu region and has consisted of particles with lower unit weight and higher porosity than other samples. After the samples have grouped manually, they were washed and dried in a 110±5 degree celsius stove for 24 hours. After the drying process each sample has weighted and recorded as batch weight. The index properties of the samples are given in Table 1.

Table 1. The index properties of the samples

Sample No	D10 (mm)	D30 (mm)	D60 (mm)	Cu	Cr	Soil Classes
1	6.60	9.93	15.20	2.30	2.82	GP
2	0.57	1.45	2.08	3.65	0.28	SP
3	2.01	5.44	7.81	3.89	0.98	GP
4	4.31	5.72	7.94	1.84	2.24	GP
5	1.82	3.03	4.68	2.57	0.76	GP
6	1.29	1.86	3.02	2.34	0.49	GP



Figure 1. Samples prepared for the study

4.2. Particle Size Distribution with Image Processing

An experimental setup has developed within the scope of determining the particle distribution in granular soils by image processing technique. In the method, each sample whose weights have recorded was laid on a 60 * 60 cm lightbox. Images have captured with a Nikon D90 body, 18-55mm Vr Nikon lens with 4288*2848 resolution in 24 bits. Images have taken in dark room conditions with the help of a tripod by adjusting the height of the camera for proper framing (Figure 2). In order to prevent the contact and overlap of the particles in the sample laid on the lightbox, a shaking device has placed under the lightbox during image capturing, the photos were taken simultaneously by shaking the lightbox with a spring mechanism's impact. The image capturing setup has shown in Figure 3. All photos have taken at f/5.6 aperture, 1/1250 shutter speed, 105mm focal length and without flash. Denser samples have needed more than single shot for more accurate analysis. The number of shots taken for the samples and the number of particles analyzed in the samples have given in Table 2. In cases where more than one photo needed to be analyzed, the algorithm that used for single analysis has exported and rearranged to recall and analyze different photos sequentially. With a simple macro arrangement, it has ensured that more than one photograph was analyzed in a single sample, and results were obtained as a single document.

Image Pro Plus version 5.1.0.20 software has used for image processing. The first step in the program was opening the photograph to be analyzed from the program interface. A pixel to millimeter conversion has required in order to obtain the results in the metric system in the analysis made on the photograph. This requirement was met by an extra shot after a length measuring tool (ruler, tape measure, etc.) has placed on the lightbox. Unit distance-pixel conversion has performed using the measurement tool from the program interface. The opened photo was in 24-bit RGB format, but since 8-bit grayscale would be sufficient for analysis, reduction process has performed through the software. Afterwards, this grayscale photo has masked and

reduced to a format that contains two values in the range selection that the program automatically assigns. Pixels above the entered threshold value and pixels below the threshold were separated and particles and the background has reduced to binary code. From the program interface, the values requested by the user were selected and outputs have obtained at the end of the analysis. MS Excel has used for further analysis in the study.

Table 2. Numerical information of the samples

Sample No	Weight (g)	Number of Grain	Number of Shot	Fmax (mm)	Fmin (mm)
1	1768.00	1459	2	41.418	2.580
2	158.42	121162	5	8.393	0.166
3	646.07	31507	4	22.050	0.500
4	1440.96	7987	5	27.404	0.478
5	326.71	17766	7	14.119	0.302
6	104.25	24217	5	18.823	0.401



Figure 2. Image acquisition environment

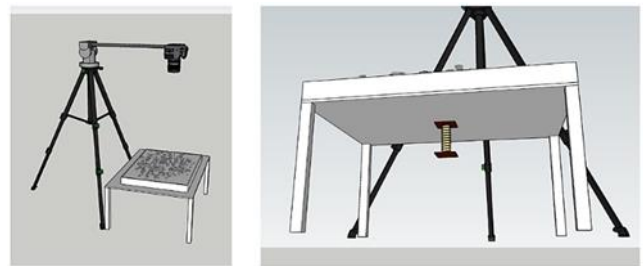


Figure 3. The setup for image capturing

Since the analysis was related to the particle size, the parameters have examined in the analysis are related to the size. The area covered by the particle in the photograph has examined in square millimeter. In addition, Fmax and Fmin values, which are the side lengths of the smallest size surrounding quadrilateral, were the parameters used in the analysis (Figure 4). The fact that the image was transferred to the digital environment in two dimensions and the reference experiment being a three-dimensional mechanical experiment have posed a problem that must be overcome for further comparisons. The data obtained by image processing were information covering two dimensions as shown in Figure 4. Researchers who have previously

conducted similar studies have derived different correction coefficients using various parameters to make the method consistent [1,18]. Even if it was accepted that the particles of the sieves are limited by two axes, one more parameter has included in the analysis with the weight measurements made after the sieving process. Within the scope of this information, it was predicted that the data obtained from image processing, including two dimensions, may not be sufficient for an accurate dimensional analysis, and a new parameter has investigated [1,15].

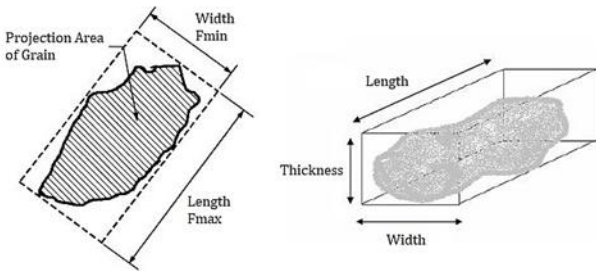


Figure 4. Image processing analysis parameters and display of three dimensions of particle [1,37]

Mora et al. [1] encountered the necessity of shifting the gradation curves for each sample when comparing the results of mechanical analysis and image processing. In this context, they ensured that the curves have approximated to the sieve analysis curves by assigning a "C" correction coefficient. The fact that the correction coefficient assigned here was at the user's initiative for each sample could lead to subjective errors. For consistent analysis this variable, which was not based on a constant and allows interpretation and abuse, have had to be excluded from the analysis [1,18].

The results were obtained from the image processing performed within the scope of the experiments in this study have included in the further analysis by using the raw data without using any correction coefficient. By following this method, the possibility of data interpretation and intervention has eliminated during processing. A value related to the shape (sphericity, angularity) and surface parameters of the particles has not been included in further investigations. This has led to the elimination of user intervention.

The obtained image processing data were filtered by accepting the hypotenuses of the meshes in the sieves as the limit, by using the standard sieve sizes. The aim here was to classify the particle diameters by using the sieve diameters and Fmax parameters, as in the process of weighing the materials remaining on the sieve in the sieve analysis. Theoretically this approach has made the comparison possible between image processing and sieve analysis in scale of sieve by sieve. By commenting on comparison results, evaluation of rate of success has been made.

$$\% \text{ Sieve Passing} = \frac{\sum_{i=1}^p (\text{Area} * F_{min})}{\sum_{i=1}^n (\text{Area} * F_{min})} \quad (1)$$

Calculations has made for each particle individually in all particle samples by using Equation 1, and then grading

curves have drawn for all sample batches. In the equation, the projection area of the particle has multiplied by the value of Fmin and the possibility of adding a third dimension to the equation is examined and the results have evaluated.

4.3. Sieve Analysis

The samples have examined by image processing technique were subjected to the sieve analysis test with the traditional sieve analysis test procedure without any loss. The sieve analysis results have recorded with standard procedures and forms, and the gradation curves of the samples have drawn. Since the particle size distribution of the samples as different, the experiments have carried out by selecting the most suitable sieve set for each batch. The selection was made by the operator. The use of different sieve sets made it possible to compare and interpret the results of the image processing method in various diameters and grain distributions. Applications using sieve set, washing container, oven, scales and shaking devices have carried out in accordance with the descriptions and procedure given in TS 3530 [31].

5. Results

Both sieve and image processing results of 6 samples have obtained at the end of the study and the results have analyzed comparatively. While the gradation curves of the samples subjected to traditional sieve analysis have drawn following the standard procedure, the data related to the visuals examined with the Image Pro Plus software have transferred to the MS Excel program for further analysis. Grading curves were drawn by using MS Excel after filtering and basic calculations. The sieve analysis results have taken as a reference, and the results obtained by image analysis techniques have displayed on a single graphic to compare both curves (Figure 5-10).

6. Conclusion

In the scope of the study, an experimental setup has been designed to apply the image processing technique as an alternative to the relatively complicated and challenging sieve analysis method. As a result, the image processing technique, which could analyze without the need for sieve analysis equipment and laboratory, has yielded similar results to traditional sieve analysis. When the results have evaluated on the basis of sieves, a maximum absolute difference of 4.78% was encountered and the validity of the applied image processing technique has shown.

When the materials of different origins used in the study have examined in different diameters and volumes and compared with the traditional method, it has observed that curves consistent with the reference curves were drawn in all six samples. This proves that the image processing technique is valid for all the particles in different texture, color, unit weight and shape used within the scope of the research.

While the image processing method benefits the researcher from time and labor, the algorithms used

were not valid for every sample and a repeat loop have has to be created for each sample. Nevertheless, this was not preventing the creation of a database according to sample types and transition to automation. In addition to the necessity of the presence of computers, cameras and lighting equipment, the researcher's has to be familiar and able to use of these equipment was another requirement.

It is possible to develop an automation for particle analysis with image processing techniques with a database created by statistical analysis including previous studies. With the developed automation, an experimental method which excludes user intervention and manipulation may be derived.

Sieve		Image Processing Results	% Passing	Absolute Difference
No.	Opening (mm)			
3/4"	19.000	100.00	100.000	0.00
5/8"	16.000	69.16	70.249	1.09
0.530"	13.500	49.32	50.339	1.02
3/8"	9.510	26.55	27.602	1.06
5/16"	8.000	17.59	18.213	0.62
1/6"	6.350	8.03	8.258	0.23
No. 5	4.000	0.00	0.000	0.00

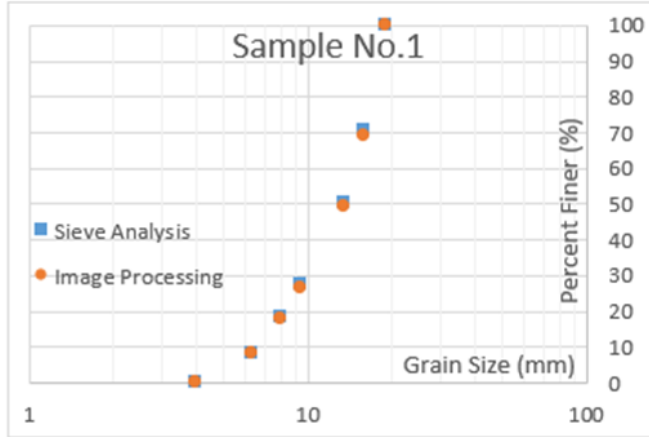


Figure 5. Comparison of results for Sample No.1

Sieve		Image Processing Results	% Passing	Absolute Difference
No.	Opening (mm)			
No. 5	4.000	100.00	100.00	0.00
No. 10	2.000	55.86	56.99	1.13
No. 12	1.680	36.72	37.26	0.54
No. 16	1.190	22.03	22.58	0.55
No. 20	0.841	15.35	16.11	0.76
No. 30	0.595	10.43	10.99	0.56
No. 35	0.500	5.60	6.29	0.69
No. 40	0.420	2.09	2.32	0.23
No. 50	0.297	0.00	0.00	0.00

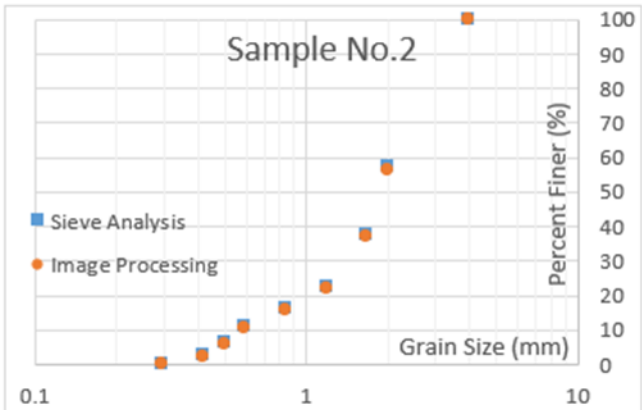


Figure 6. Comparison of results for Sample No.2

Sieve		Image Processing Results	% Passing	Absolute Difference
No.	Opening (mm)			
3/8"	9.500	100.00	100.00	0.00
5/16"	8.000	62.60	64.93	2.33
1/4"	6.350	33.69	35.72	2.03
No. 5	4.000	19.58	18.82	0.76
No. 10	2.000	11.87	10.05	1.82
No. 12	1.680	9.45	6.31	3.14
No. 16	1.190	5.27	3.71	1.56
No. 18	1.000	3.33	2.44	0.88
No. 20	0.841	1.67	1.37	0.30
No. 30	0.595	0.79	0.61	0.18
No. 35	0.500	0.00	0.00	0.00

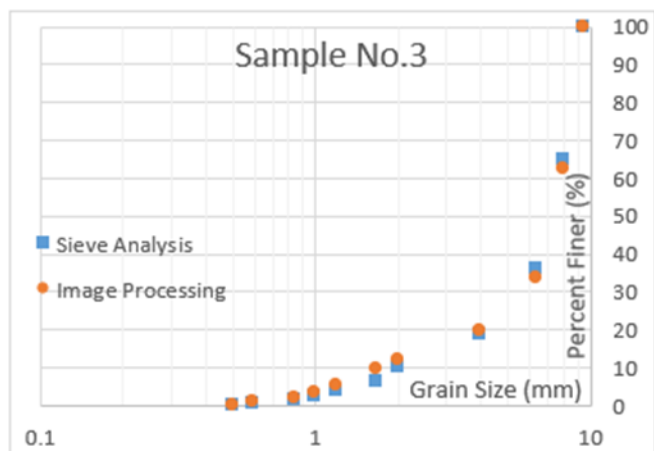


Figure 7. Comparison of results for Sample No.3

Sieve		Image Processing Results	% Passing	Absolute Difference
No.	Opening (mm)			
0.530"	13.500	100.00	100.00	0.00
3/8"	9.500	82.18	81.64	0.54
5/16"	8.000	62.68	61.79	0.89
1/4"	6.350	39.45	38.87	0.58
No. 5	4.000	5.22	5.09	0.13
No. 10	2.000	0.69	0.70	0.00
No. 12	1.680	0.43	0.45	0.02
No. 16	1.190	0.13	0.14	0.01
No. 20	0.841	0.00	0.00	0.00

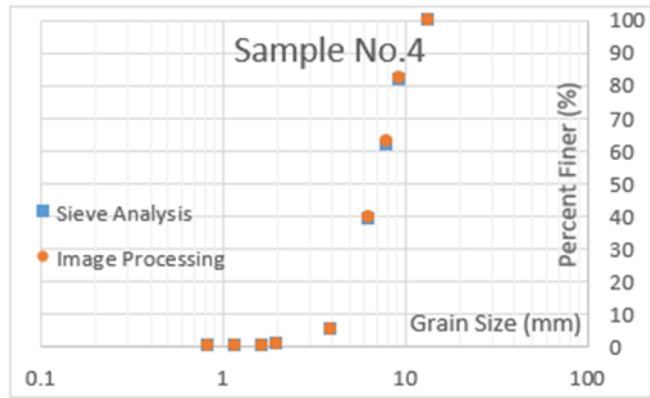


Figure 8. Comparison of results for Sample No.4

Sieve		Image Processing Results	% Passing	Absolute Difference
No.	Opening (mm)			
5/16"	8.000	100.00	100.00	0.00
1/4"	6.350	97.20	97.69	0.49
No. 5	4.000	35.63	40.27	4.63
No. 10	2.000	10.45	14.08	3.62
No. 12	1.680	5.49	7.84	2.35
No. 16	1.190	2.57	3.91	1.33
No. 20	0.841	0.66	1.05	0.39
No. 35	0.500	0.00	0.00	0.00

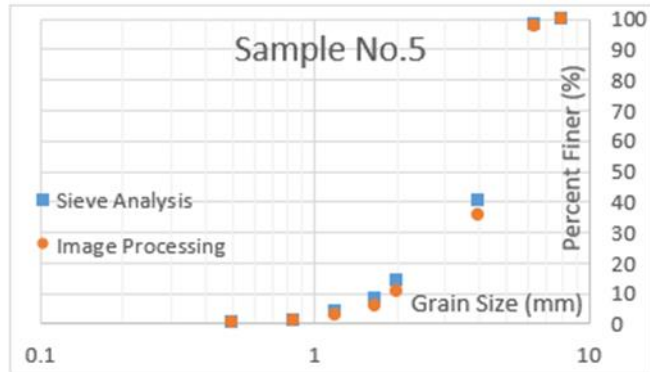


Figure 9. Comparison of results for Sample No.5

Sieve		Image Processing Results	% Passing	Absolute Difference
No.	Opening (mm)			
5/16"	8.000	100.00	100.00	0.00
1/4"	6.350	91.28	93.90	2.62
No. 5	4.000	73.81	74.92	1.11
No. 10	2.000	34.43	38.56	4.13
No. 12	1.680	18.05	22.83	4.78
No. 16	1.190	6.37	9.77	3.40
No. 20	0.841	1.30	2.27	0.97
No. 35	0.500	0.00	0.00	0.00

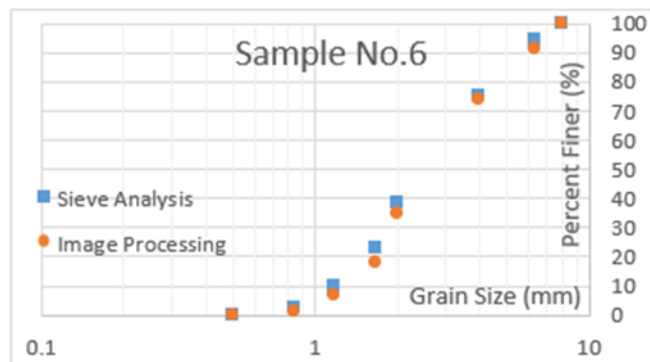


Figure 10. Comparison of results for Sample No.6

Acknowledgement

The authors are thankful to Bünyamin Demir and Bahadır Sayinci for the contributions for the study.

Author contributions

Mert Aydin: Methodology, Software **Talas Fikret Kurnaz:** Writing-Original draft preparation, Investigation, Writing-Reviewing and Editing.

Conflicts of interest

The authors declare no conflicts of interest.

References

1. Mora, C., Kwan, A., Chan, H. (1998). Particle Size Distribution Analysis of Coarse Aggregate Using

Digital Image Processing. Cement and Concrete Research, 28 (6), 921-932.
 2. Sezer, A. (2008). Determination of Microapical Properties of Different Types of Soils Using Image Processing Techniques, PhD Thesis, İzmir: Ege University Graduate School of Sciences, Department of Civil Engineering (in Turkish).
 3. Murthy, V. N. S. (2002). Geotechnical Engineering, Principles and Practices of Soil Mechanics and Foundation Engineering, CRC Press.
 4. Obaidat, M. T., Al-Masaaid, H. R., Gharaybeh, F., & Khedaywi, T. S. (1998). An Innovative Digital Image Analysis Approach to Quantify the Percentage of Voids in Mineral Aggregates of Bituminous Mixtures. Canadian Journal of Civil Engineering, 25:1041-1049.
 5. Gaydecki, P., Silva, I., Fernandes, B. T., Yu, Z. Z. (2000). A Portable Inductive Scanning System for Imaging Steel-Reinforcing Bars Embedded Within Concrete. Sensors and Actuators, 84:25-32.

6. Soroushian, P., Elzafraney, M., Nossoni, A. (2003). Specimen preparation and image processing and analysis techniques for automated quantification of concrete microcracks and voids. *Cement and Concrete Research*, 33:1949-1962.
7. Soroushian, P., Elzafraney, M. (2005). Morphological operations, planar mathematical formulations, and stereological interpretations for automated image analysis of concrete microstructure. *Cement & Concrete Composites*, 27:823-833.
8. Felekoglu, B., Güllü, D. (2006). Use of optical microscope and image processing techniques in clinker analysis. *IMO Technical Journal*, 247, 3761-3770.
9. Sinha, S. K., & Fieguth, P. W. (2006). Automated detection of cracks in buried concrete pipe images. *Automation in Construction*, 15, 58-72.
10. Park, S. H., Kim, H. K., Morales, A., & Ko, S. J. (2007). Air-void analysis system of polished concrete using image processing. *Journal of Applied Computer Science*, 15 (2), 19-25.
11. Ozen, M. (2007). Investigation of Relationship Between Aggregate Shape Parameters and Concrete Strength Using Imaging Techniques, Master's Thesis, Ankara: Middle East Technical University, The Graduate School of Natural and Applied Sciences.
12. Comak, B., Beycioğlu, A., Başıyigit, C., Kılınçarslan, S. (2011). Use of Image Processing Techniques in Concrete Technology. 6th International Advanced Technologies Symposium (IATS'11), Elazığ.
13. Dipova, N. (2017). Determining The Grain Size Distribution of Granular Soils Using Image Analysis. *Acta Geotechnica Slovenica*, 1, 29-37.
14. German, R. M. (1994). *Powder Metallurgy Science*, New Jersey: Metal Powder Industries Federation.
15. Yue, Z. Q., Bekking, W., Morin, I. (1995). Application of digital image processing to quantitative study of asphalt concrete microstructure. *Transportation Research Record*, 1492:53-60.
16. NG, T. T. (1999). Fabric Study of Granular Materials After Compaction. *ASCE Journal of Engineering Mechanics*, 125 (12), 1390-1394.
17. Masad, E., & Button, J. (2000). Unified Imaging Approach for Measuring Aggregate Angularity and Texture. *Computer-Aided Civil and Infrastructure Engineering*, 15(4), 273-280.
18. Mora, C. F., & Kwan, A. K. H. (2000). Sphericity, shape factor, and convexity measurement of coarse aggregate for concrete using digital image processing. *Cement and concrete research*, 30(3), 351-358.
19. Yue, Z. Q., Chen, S., & Tham, L. G. (2003). Finite element modeling of geomaterials using digital image processing, *Computers and Geotechnics*, 30, 375-397.
20. Rousan, T. M. A. (2004). Characterization of Aggregate Shape Properties Using a Computer Automated System, Phd Thesis, USA: Texas A&M University.
21. Alshibli, K., & Alsaleh, M. (2004). Characterizing surface roughness and shape of sands using digital microscopy. *ASCE Journal of Computing in Civil Engineering*, 18 (1), 36-45.
22. Yang, X. (2005). Three Dimensional Characterization of Inherent and Induced Sand Microstructure, Phd Thesis, Georgia Institute of Technology.
23. Hu, R., Yue, Z., Tham, L., & Wang, L. (2005). Digital image analysis of dynamic compaction effects on clay fills. *ASCE Journal of Geotechnical and Geoenvironmental Engineering*, 131 (11), 1411-1422.
24. Edizer, E. (2006). Particle Size Distribution with Digital Image Processing Method, Master Thesis, Adana: Çukurova University, Institute of Science and Technology.
25. Vangla, P., Roy, N., Mendu, K., & Latha, G. M. (2014). Digital Image Analysis for the Determination of Size and Shape Parameters of Sand Grains. Golden Jubilee Conference of the IGS Bangalore Chapter, Geo Innovations, Bangalore India.
26. Ehsan, K. M., Hossain, M. R., Manzur, T., Shohag, A., & Tabassum, N. (2016). Particle Size Analysis by Image Processing Technique. 1st Bangladesh Civil Engineering Summit, Dhaka, Bangladesh.
27. Jahne, B. (2005). *Digital Image Processing*, Germany: Springer.
28. Gonzales, R. C., & Woods, R. E. (2001). *Digital Image Processing*, USA: Prentice Hall.
29. McAndrew, A. (2004). *An Introduction to Digital Image Processing with MATLAB*, Melbourne: Victoria University of Technology.
30. Gonzales, R. C., & Woods, R. E. (2008). *Digital Image Processing*, Upper Saddle River, NJ: Pearson Prentice Hall, 1-3.
31. Turkish Standards Institute TS 3530 EN 933-1/April (1999). Experiments for Geometric Properties of Aggregates Part 1: Determination of Particle Size Distribution-Sieving Method
32. Mertens, G., & Elsen, J. (2006). Use of computer assisted image analysis for the determination of the grain-size distribution of sands used in mortars. *Cement and Concrete Research* 36:1453-1459 DOI: 10.1016/j.cemconres.2006.03.004.
33. Fernlund, J. M. R., Zimmerman, R. W., & Kragic, D. (2007). Influence of volume/mass on grain-size curves and conversion of image-analysis size to sieve size. *Engineering Geology*, 90:124-137 DOI: 10.1016/j.enggeo.2006.12.007.
34. Allen, T. (1968). *Particle size measurement*, Chapman and Hall, London.
35. Pettijohn, F. J. (1984). *Sedimentary Rocks*. S.K. Jain, India.
36. Fernlund, J. M. R. (1998). The effect of particle form on sieve analysis: a test by image analysis. *Engineering Geology* 50:111-124 DOI: 10.1016/S0013-7952(98)00004-0.
37. Erdogan, S., & Fowler, D. (2005). Determination of aggregate shape properties using x-ray topographic methods and the effect of shape on concrete rheology. International Center for Aggregate Research, ICAR:106-1.





A comparative assessment for efficient oleuropein extraction from olive leaf (*Olea europaea* L. folium)

Yaşar Kemal Recepoğlu¹, Gülin Gümüşbulut¹, Aslı Yüksel Özşen^{*1,2}

¹Izmir Institute of Technology, Department of Chemical Engineering, Türkiye

²Izmir Institute of Technology, Geothermal Energy Research and Application Center (GEOCEN), Türkiye

Keywords

Extraction
Phenolic compound
Oleuropein
Olive leaf
Soxhlet

Research Article

DOI: 10.31127/tuje.1058500

Received: 16.01.2022

Accepted: 06.03.2022

Published: 26.04.2022

Abstract

Since oleuropein has long been known in the health sector and is abundant directly in our country as the fourth largest olive producer, oleuropein, the predominant phenolic ingredient in olive leaves, was recovered in this study using Soxhlet extraction. The effects of different solvent types (acetonitrile, ethanol, methanol, and water), extraction period (4 cycles, 4 h, and 8 h), particle size (250-500 µm and 900-2000 µm), and pretreatment of olive leaves on the yield of oleuropein were examined to determine the maximum yield. A greater oleuropein yield was obtained when the particle size of olive leaves utilized for extraction was lowered. Furthermore, aqueous solvents revealed a higher yield of oleuropein than pure solvents and prolonging the extraction duration resulted in a significant increase in the amount of oleuropein extracted. On the other hand, pretreatment of olive leaves resulted in a reduction in oleuropein output. As a result, with 36% extraction efficiency in terms of olive leaf conversion, the highest oleuropein extraction yield was obtained as 13.35 mg g⁻¹ dry leaf for 8 h of extraction time using olive leaves with a particle size of 250-500 µm and an 80% methanol solution as solvent.

1. Introduction

Phenolic substances are prevalent in plants and serve a crucial role in plant growth, development, and reproduction by combating diseases and harmful bacteria. They are also responsible for plants and fruits' sensory qualities like color, bitterness, taste, and odor [1]. There is a wide variety of polyphenols in nature because phenolic compounds may take on a variety of structural shapes depending on their bonding state. As a result of a comprehensive survey, more than 8000 polyphenol structures have been found [2]. Owing to their potential health advantages for humans, polyphenols are of tremendous interest in the functional food, nutraceutical, and pharmaceutical industries [3]. According to research and the use of polyphenols, olive leaves are known to be a good source of polyphenols [4]. One of the principal phenolic substances found in olive fruits and leaves is the o-dihydroxyphenol glycoside oleuropein [5].

Oleuropein is a bitter glycoside found throughout the olive tree, but primarily in the leaves [6,7], and studies suggest that this phenolic substance has significant anti-inflammatory [8], antimicrobial [9,10], and antiviral activities [11], among others. Consumers are increasingly seeking natural goods or products that incorporate natural chemicals in their composition, pushing researchers in the food and cosmetic fields to investigate replacing synthetic antioxidants with those derived from plants [12,13]. Phenolic ingredients can be extracted by several methods including the use of cold solvents [14], filtration [15], microwave [16], microfluidic system [17], pressurized fluid [18], Soxhlet [19,20], supercritical fluids [21], and ultrasound [22,23]. Soxhlet extraction is well known and preferred as an extraction method that offers much higher efficiency than other methods in obtaining the desired target compounds (antioxidant and phenolic compounds) [24]. In addition, it has some advantages over other methods, such as ease of operation, less costly, constant operating conditions (e.g., temperature), no need for additional

* Corresponding Author

* (yasarrecepoglu@iyte.edu.tr) ORCID ID 0000-0001-6646-0358
(glingumusblt@gmail.com) ORCID ID 0000-0002-5595-3074
(asliyuksel@iyte.edu.tr) ORCID ID 0000-0002-9273-2078

Cite this article

Recepoglu, Y. K., Gümüşbulut, G., & Özşen, A. Y. (2023). A comparative assessment for efficient oleuropein extraction from olive leaf (*Olea europaea* L. folium). Turkish Journal of Engineering, 7(2), 116-124

filtration and product purification, and constant contact of solvent and sample [25,26]. On the other hand, various experimental parameters dependent on these approaches, such as time, temperature, and solvent type, affect the extraction of phenolic compounds such as oleuropein. To generate this molecule, researchers studied to optimize the process and identify "clean" technologies that use non-toxic solvents and are low-cost. Japón Luján et al. [27] investigated the identification and quantification of phenolic chemicals in olive tree material extracts (olive oil, olive pomace, leaves, olive pits, and branches). Oil was extracted using liquid-liquid extraction, leaves, stones, and twigs were filtered using micro-assisted filtration, and olive pomace was filtered using pressure-liquid filtration. Oleuropein, which has a concentration of 2% (w/w) in olive leaves, was the highest phenolic component in olive tree materials. Oleuropein concentrations in leaves and branches were around 19 mg g⁻¹ and 0.6 mg g⁻¹, respectively. Yateem et al. [19] evaluated parameters such as pH, temperature, and solvent type for the extraction of oleuropein from olive leaves, and the highest content of oleuropein as 13 mg g⁻¹ dry olive leaf was obtained using 80% ethanol followed by 20% acetonitrile as 10 mg g⁻¹ dry olive leaf. In another study, to enhance extraction yield, oleuropein content, and antioxidant activity, olive leaves were subjected to a pressurized liquid extraction (PLE) using environmentally friendly solvents such as water and ethanol. An ethanolic extraction at 190°C for three consecutive cycles was determined to be best regarding extraction yield. In terms of extracted oleuropein content, 43:57 mixtures of H₂O/EtOH at 190°C for 1 extraction cycle produced the optimum results [28]. Zunquiu et al. [29] compared the yields of oleuropein in leaves harvested at various dates during the harvest season. According to the findings, oleuropein levels dropped during flower bud differentiation and olive fruit ripening, with January having the highest oleuropein concentration (19.58%) and July having the lowest (1.56%). Lamprou et al. [30] studied a new low-cost acid hydrolysis process for extracting phenolic components from olive leaves (H₂SO₄). After hydrolysis, the resultant extract yielded an optimal level of oleuropein of 43.2 mg g⁻¹ (dry weight basis). Recently, Cho et al. [31] examined the impact of the extraction solvent type (water, aqueous acetone, ethanol, and methanol) on various extract parameters to find the best conditions for olive leaf conversion to obtain phenolic. With 90% (by volume) methanol, the greatest extraction yield of 20.41% was obtained. The olive tree (*Olea europaea*) and its by-products, such as a leaf, have also been studied by utilization of microwave-assisted extraction to create an extract high in total phenolics (TPI), flavonoids (TFI), and antioxidant activity (AA) using a variety of common solvents (ethanol, methanol, acetonitrile, and acetone solutions) (MAE). On the other hand, the response surface method (RSM) was used to establish the best experimental conditions of the parameters that were effective on a limited number of tests using a 3-factor and 3-level central composite design (CCD). Under ideal conditions, the best results for TPI, TFI, and AA were 10.45 mg GAE/g DL, 9.69 mg CE/g DL, and 96.34% (230

W, 1.5 min, and 63.16 mL of 30% acetonitrile solution) [32].

The main objective of this study is to investigate and compare oleuropein extraction yield in a wide range of solvents (acetonitrile, ethanol, and methanol) in pure and aqueous concentrations under different parameters (extraction time, particle size, and pretreatment) by Soxhlet technique. Since Turkey ranks fourth in world olive production after Spain, Italy, and Greece in terms of botanical properties, ecophysiology, and phytochemical aspects [33], obtaining extracts such as oleuropein from the leaves of olive trees grown in large quantities can contribute considerably to the economy of Turkey.

2. Experimental

2.1. Chemicals

The olive leaves employed as a raw material source in this study were obtained from olive trees on the Izmir Institute of Technology's campus (Izmir, Turkey). Oleuropein (98%) and sodium carbonate (99.5%) were purchased from Sigma Aldrich, while methanol (99.8%), ethanol (99.9%), acetonitrile (99.9%), acetic acid (99%), gallic acid (97.5%) and Folin-Ciocalteu's phenol reagent were provided from Merck.

2.2. Method

Before usage, olive leaves were thoroughly cleaned with tap water to remove dust and debris, sprinkled with deionized water, and dried for 24 hours in a vacuum oven (JSR JSVO-60T) at 55°C. After drying, the leaves were ground into a fine powder between 250 and 2000 microns using a laboratory-scale grinder. To avoid frictional heating of the sample, the grinding procedure was repeated every 5 minutes.

Oleuropein was extracted from olive leaves using a Wisd brand Soxhlet extraction apparatus (DH.WHM 12295). The filter paper was used to weigh 10 g of pulverized olive leaves, which were then put in an extractor with a 250 mL solvent capacity. In this context, to obtain the highest oleuropein yield, the effects of different parameters were studied, namely solvent type (methanol, ethanol, acetonitrile) and their aqueous forms, extraction period (4 cycles, 4 h, and 8h), particle size (250-500 µm, 900-2000 µm). In addition, the effect of pretreatment on the amount of oleuropein in the extract and the efficiency of extraction was studied in such a way that the particle size was set between 250 and 500 microns, and the solvents were chosen based on the best results of the preceding parameters: 80% methanol and 80% ethanol. The treatments were carried out in an ultrasonic bath at 40 kHz on 25-30°C for 1 hour. After the 1-hour pretreatment in the ultrasonic bath, the olive leaves were placed on filter paper and placed in the Soxhlet extractor. The extraction took place in 4 hours and 8 hours.

A rotary evaporator was used to separate the extract from the solvent when the extraction was completed (Laborota 4001, Heidolph). The rotary evaporator's water bath temperature was set at 40°C, and the rotation frequency was set to 60 rpm. The remaining solid residue, on the other hand, was placed in a vacuum oven

for 24 hours at 50°C to remove moisture. The overall olive leaf conversion (X , wt%) was calculated based on the initial dry olive leaf amount (W_i , g) and the amount of remaining solid residue (W_s , g) according to the Eq. (1):

$$X \text{ (wt\%)} = \frac{W_i - W_s}{W_i} \times 100 \quad (1)$$

To assess the quantity of oleuropein in the olive leaf extract, a high-performance liquid chromatography (HPLC) instrument was used to evaluate the concentrated liquid product. A C18 Inerstil column (5 m, 250 mmx4.6 mm) and an Agilent 1100 series detector are included in the HPLC system. The mobile phase was acetonitrile/water (20:80, v/v) containing 0.1% acetic acid, and it was fed with a flow rate of 1 mL min⁻¹ at a column temperature of 30°C.

The extracted amount of oleuropein was calculated by the Eq. (2):

$$q = \frac{C_{oleuropein} \times V}{W_i} \quad (2)$$

where q is the amount of oleuropein per total gram of dry olive leaf (mg g⁻¹ dry leaf), $C_{oleuropein}$ is the concentration of oleuropein transferred to the solvent phase (mg L⁻¹) and V is the extracted volume (L).

Folin-Ciocalteu's method was also used to determine the total phenolic content of the liquid extract. Folin-Ciocalteu's reagent was diluted 10-fold in this procedure, and a 7.5 percent (75 g L⁻¹) sodium carbonate solution was prepared. After combining 0.5 mL of Folin-Ciocalteu's reagent, 0.5 mL of liquid product, and 1 mL of saturated sodium carbonate solution, the volume was adjusted to 10 mL with distilled water. After mixing, the liquid was kept at room temperature for 45 minutes in the dark. Thermo's Multiscan UV spectrophotometer was used to detect the absorbance at 765 nm, and the phenolic content was defined in gallic acid equivalents (mg GAE/mL).

3. Results and Discussion

3.1. Effect of extraction solvent on conversion of olive leaf and oleuropein yield

Solvent selectivity has great importance in extraction processes to obtain the desired compound from the plant material. To obtain a high yield of the desired compound in the extraction process, the extracted compound and the solvent must have similar polar properties. Because oleuropein, the most abundant phenolic ingredient in olive leaf extract, is a polar substance, a solvent with a high polarity is required to get oleuropein efficiently [34,35]. Polar protic solvents are solvents with polar features that release hydrogen into the environment and feed hydrogen to the environment via -OH bonds, resulting in increased extraction efficiency [36,37].

The effect of solvent type on the conversion of olive leaf and oleuropein yield under 10 g of dry olive leaf with a particle size of 250-500 μm, in the presence of different solvents (pure, 80%, 70%, 50%, and 20% ethanol, pure, 80% and 50% methanol, 20% acetonitrile and water) and extraction time of 8 hours' conditions are shown in

Fig. 1. The content of oleuropein varied from 0.48 to 13.35 mg g⁻¹ dry olive leaf. The amount of oleuropein obtained in tests using methanol as a solvent was often higher than that obtained in experiments using other solvents. The highest amounts of oleuropein were found with 13.35 mg g⁻¹ dry leaf with 80% methanol as solvent and 12.44 mg g⁻¹ dry leaf with 80% ethanol as solvent. Meanwhile, 37.55 mg g⁻¹ dry leaf was reported as the highest yield of oleuropein using pure methanol as solvent, while this value was found to be 18.58 mg g⁻¹ dry leaf using methanol/hexane (3/2:v/v) as solvent [38].

The quantity of oleuropein normally increases as the polarity of the solvents utilized increases. When compared to water (1), the polarity of methanol (0.762) and ethanol (0.654) is lower, resulting in a drop in the solvent's dielectric constant, which improves the solubility and diffusion of the desired target molecules in the solvent. However, the use of solvents in their pure form leads to dehydration and the collapse of plant cells. Proteins and phenolic chemicals in the cell wall are also denatured. The extraction of phenolic compounds becomes harder as a result of these factors [39]. In our case, the lowest extraction efficiency was 17.6% in water, while the highest extraction efficiency was 36% in 80% methanol and 29.8% in 20% acetonitrile by volume, respectively. Pure ethanol and its aqueous solutions produced nearly identical findings, however, tests using methanol as a solvent yielded higher oleuropein yields. This can be explained by the higher polarity value of methanol compared to other solvents. Moreover, there is a big difference in oleuropein yield between the solvents in pure form (ethanol and methanol) and their aqueous solvents. This can also be explained by the higher polarity value of aqueous solvents as compared to pure solvents. Although water is the most polar solvent used, it does not seem to perform well in the extraction of oleuropein. The reason could be that the Soxhlet method's long boiling period at high temperatures decreases the extract's oleuropein concentration. The absence of such a situation in methanol extracts may be explained by the fact that the boiling point of methanol (64.7°C) is lower than that of water.

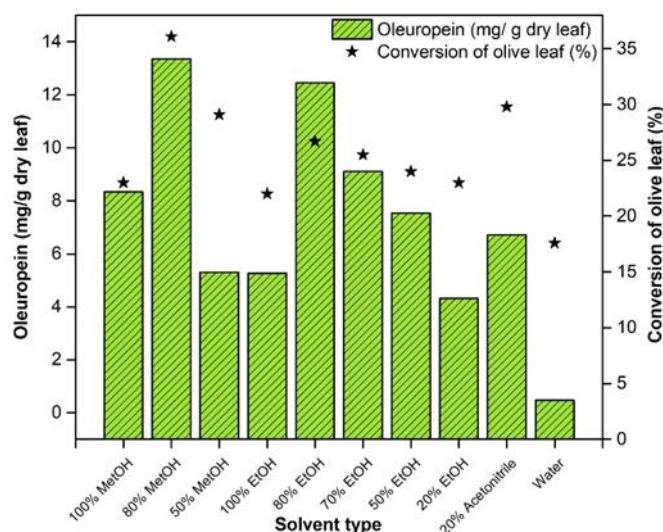


Figure 1. Effect of solvent type on the quantity of oleuropein extracted per gram of dry leaf and olive leaf conversion after an 8-hour Soxhlet extraction

3.2. Effect of extraction time on conversion of olive leaf and oleuropein yield

To minimize energy and cost, one of the most significant aspects to study in the extraction process is extraction time. The data obtained from 10 g of olive leaves with size 250-500 μm in 4 h and 8 h by Soxhlet extraction using pure, 80%, and 50% methanol, pure, 80%, 70%, 50% and 20% ethanol, 20% acetonitrile and water are shown in Figs. 2a and 2b.

The highest extracted amount of oleuropein was recorded as 13.35 mg g^{-1} of dry leaves after 8 hours of extraction with 80% methanol. The use of 80% ethanol as solvent for 8 hours of extraction resulted in a remarkable amount of oleuropein of 12.44 mg g^{-1} dry leaf as well. When comparing extraction times, 8-hour tests yielded significantly more oleuropein than 4-hour experiments. Methanol outperformed ethanol at different times (4.13 mg g^{-1} dry leaf for 4 h with pure methanol, 3.7 mg g^{-1} dry leaf for 4 h with pure ethanol). In addition, Pure solvents extracted less oleuropein from olive leaves than aqueous solvents, according to the findings. Xie et al. [40] also investigated the effect of varied ethanol-water mixture proportions on the yield of oleuropein extract. The maximum oleuropein yield was discovered to be between 55 and 75% ethanol, and the mixture of ethanol and water was shown to be a good solvent. Because it combines polarity and penetration properties, this feature is particularly essential. The affinity of the solvent and solute, as well as the increased surface area of contact between the solvent and solute, were also thought to boost the yield of the target molecule. Therefore, the oleuropein yield and ethanol

concentration fell between 75 and 85% before remaining unchanged between 85 and 95%. The content of ethanol increased while its polarity reduced as a result of the observations. This property was discovered to be detrimental to oleuropein yield, and the optimum ethanol concentration was set at 75%.

Furthermore, both 80% methanol and 80% ethanol gave higher yields of oleuropein under different experimental conditions. The amounts of oleuropein in the solvent 20% acetonitrile were almost the same for different extraction times. For example, 6.4 mg g^{-1} dry leaf was obtained with 20% acetonitrile for 4 hours while 6.72 mg g^{-1} dry leaf was obtained with 8 hours. The oleuropein amount of 20% acetonitrile solvent gave better results than the 20% ethanol solvent in the 4- and 8-hours extraction experiments. Although acetonitrile gives good results in oleuropein amount, it was not used in other experiments because of its high boiling point and because it is an expensive solvent. The boiling temperature of acetonitrile is 81.6°C and similar oleuropein yields were obtained as it is close to the boiling point of water. Since the boiling points of ethanol or methanol are lower than the boiling temperature of water, higher oleuropein yields were observed in the presence of these solvents.

On the other hand, the highest extraction efficiency in terms of olive leaf conversion was found to be 36% using 80% methanol for 8 hours. The following highest conversion efficiencies were obtained using 80% ethanol and 70% ethanol for 4 hours' extraction with 30% and 32.3% respectively. The extraction yields at two different extraction times were very close even at 50% ethanol.

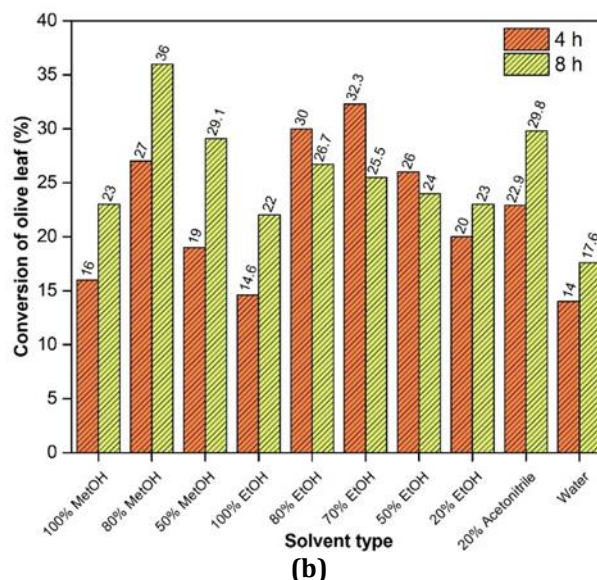
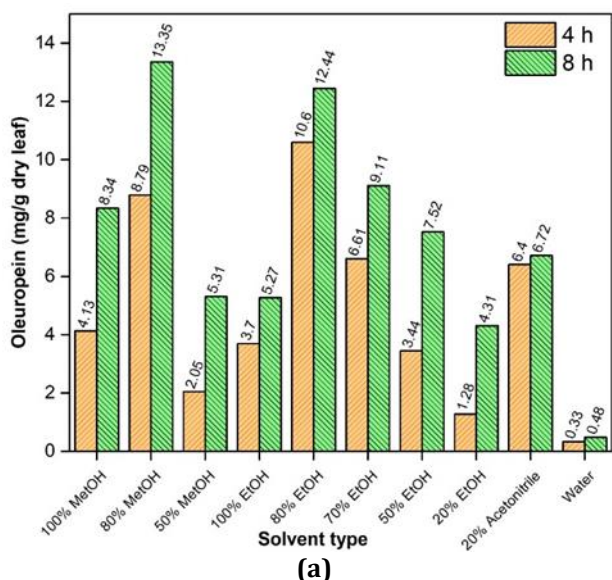


Figure 2. Effect of extraction time on (a) the amount of oleuropein extracted per gram of dry leaf and (b) the conversion of olive leaves by Soxhlet extraction

3.3. Effect of particle size on conversion of olive leaf and oleuropein yield

Pre-treatments, such as separation techniques or particle size reduction, could be applied to raw materials to achieve a great improvement in the extraction

efficiency of phenolic compounds [41]. Physical processes such as drying and grinding are of great importance in obtaining herbal extracts. The values of oleuropein and extraction yield at various particle sizes were attempted to be determined in this section. Oleuropein was aimed to be extracted from 10 g of olive

leaves in four cycles using pure methanol and ethanol, 80% ethanol, and water solvents (1 cycle = 45 min for methanol, 40 min for ethanol, and 75 min for water). The operating conditions were kept the same in all experiments, the particle sizes of olive leaves (250-500 μm , 900-2000 μm) were changed to understand the effect of particle size on oleuropein yield. Figs. 3a and 3b show the determined oleuropein and extraction yields by Soxhlet extraction of particles of various sizes, respectively. Particle size was found to significantly affect oleuropein yield. In an 80% ethanol extract, the yield of oleuropein obtained with a size of 250-500 μm was about 5 times higher than that obtained with a size of 900-2000 μm . The highest oleuropein yield was 5.4 mg g^{-1} dry leaf with 80% ethanol, 250-500 μm , while the lowest oleuropein yield was 0.03 mg g^{-1} dry leaf with

water, 900-2000 μm . This is due to the fact that as particle sizes are reduced, the surface area rises, making oleuropein extraction considerably easier and efficient. Additionally, the highest yield in terms of olive leaf conversion (26.7%) was also found when 80% ethanol was used as solvent and particle size was 250-500 μm , while the lowest yield (9.5%) was obtained when water was used with a particle size of 900-2000 μm of olive leaves. In general, it was observed that the solvents used (ethanol, methanol, and water) showed higher extraction efficiency for particles with size of 250-500 μm . Overall, the results are in good agreement with the literature, namely, Nagy & Simándi, (2008) studied the impact of particle size and moisture content on supercritical fluid extraction of chili peppers and found that using smaller particle sizes resulted in greater extraction yields [42].

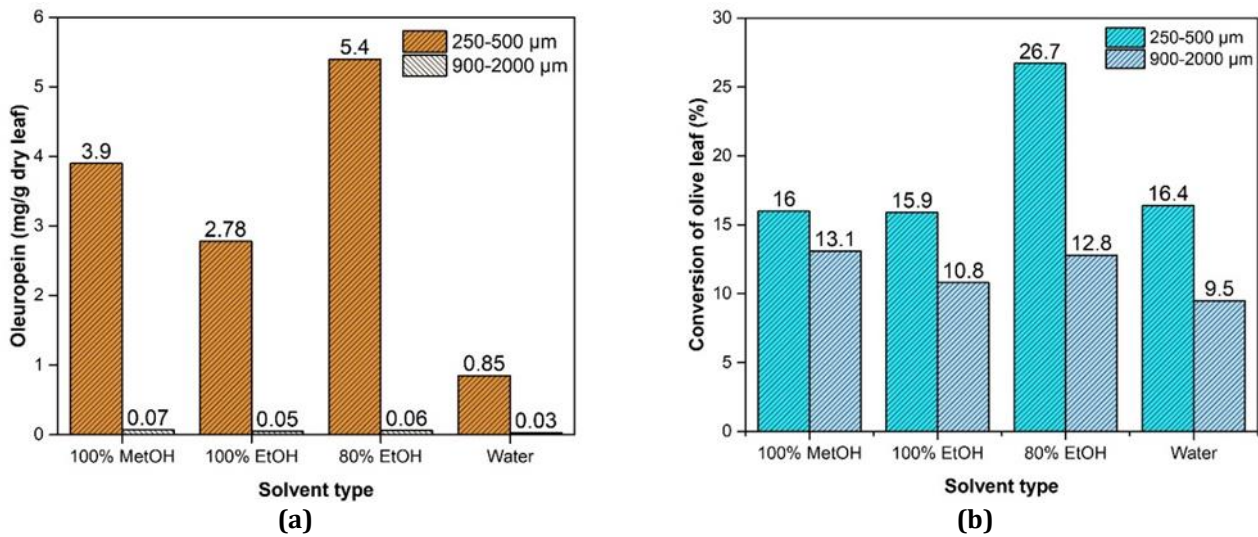


Figure 3. Effect of particle size on (a) the amount of oleuropein extracted per gram of dry leaf and (b) the conversion of olive leaves by Soxhlet extraction in four cycles extraction

3.4. The effect of pre-treatment on oleuropein yield and extraction efficiency

The data regarding the effect of pretreatment on oleuropein yield and extraction efficiency are presented in Table 1. For better differentiation, the results were compared with Soxhlet extraction experiments without pretreatment carried out under the same conditions (250-500 μm , 80% MetOH (4 h and 8 h) and 80% EtOH (4 h and 8 h)). As expected, a decrease in the extracted amount of oleuropein was observed due to the degradation of phenolic compounds in olive leaf during the sonication for 1 h. Nevertheless, among the pretreatment experiments, the highest oleuropein content was found to be 5.57 mg g^{-1} dry leaf when 80% MetOH was used for 8 h, while the lowest oleuropein content was 3.17 mg g^{-1} dry leaf when 80% EtOH was used for 4 h. According to a recent investigation of ultrasound-assisted extraction for the yield of oleuropein and hydroxytyrosol with extraction times of 10 min, 30 min, 60 min and 120 min, the highest yield of oleuropein, was obtained in the first 10 min of extraction with a value of 10.65 mg g^{-1} dry leaf. However, a steady decrease in the oleuropein yield was observed when extraction times of more than 10 min were applied in the experiment [43]. In another study, olive leaves were also extracted by

ultrasound assisted and low-pressure extraction of 1, 2, 3, 4, 5, 10 and 15 min duration. The maximum oleuropein yield was obtained after 3 min but then stabilized with increasing time, indicating that oleuropein extraction was completed after 3 min [44]. Overall, pretreatment by sonication had a negative effect on oleuropein yield, as part of the phenolic content might have degraded by the temperature rise during heating in the ultrasonic bath.

Table 1. The effect of ultrasonic pre-treatment on oleuropein yield

Solvent Type	Extraction Time	Oleuropein Yield (mg/g dry leaf)
80% methanol (Without pre-treatment)	4 h	8.79
	8 h	13.35
80% methanol (With pre-treatment)	4 h	4.85
	8 h	5.57
80% ethanol (Without pre-treatment)	4 h	10.6
	8 h	12.44
80% ethanol (With pre-treatment)	4 h	3.17
	8 h	5.06

3.5. Total phenolic content assay (Folin-Ciocalteu's method)

The effect of pure ethanol and its aqueous forms such as 20%, 50%, 70% and 80% with different extraction times (4 h, 8 h) on total phenolic content and the comparison of extraction with ethanol and methanol with 4 h duration in terms of phenolic content is shown in Figs. 4a and 4b, respectively. The highest phenolic content was observed with 80% ethanol for 8 h (0.082 mg GAE mL⁻¹), while extraction for 4 h with pure ethanol gave the lowest value for phenolic content (0.02 mg GAE mL⁻¹). Pure ethanol did not show to be a viable solvent

for olive leaf extraction for both the amount of oleuropein and total phenolic content, but 20% ethanol appears to produce better results than pure ethanol for both oleuropein and total phenolic content. This finding implies that water is required to improve polyphenol extraction from plant tissue diffusion, making extraction easier and more effective. The total phenolic content was almost comparable in terms of the amount of oleuropein when used ethanol and methanol and their aqueous solutions as solvent type. The highest yield was obtained using 80% ethanol solution and the phenolic content was found to be 0.068 mg GAE mL⁻¹.

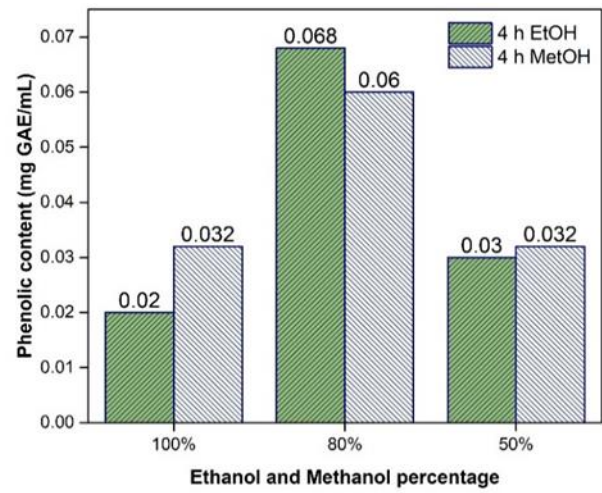
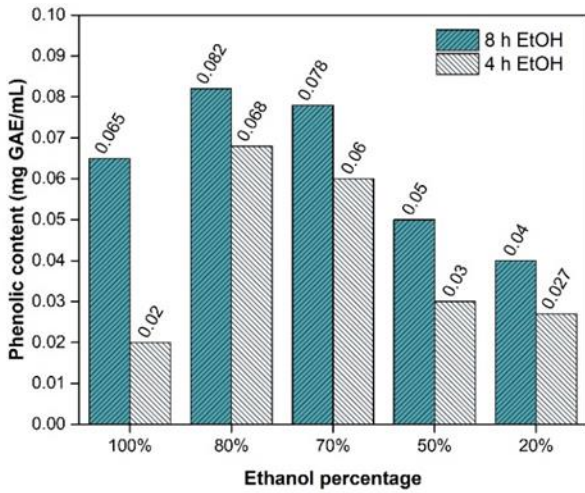


Figure 4. The influence of **(a)** extraction time (4 h, 8 h) with different ethanol content and **(b)** solvent type (ethanol, methanol) with 4 h extraction on total phenolic content.

4. Conclusion

This study contributes to the valorization of olive leaves by extracting polyphenols from them using different types of solvents and parameters. Oleuropein, the major phenolic compound in olive leaves, was obtained by Soxhlet extraction, which has long been known in the health field and is a crucial raw material with high availability in our country, as Turkey is the fourth largest olive producer in the world. In this context, the type of solvent and aqueous solutions (ethanol, acetonitrile, methanol, and water), extraction time (4-8 h), particle size (250-500 μm and 900-2000 μm) and pre-treatment of olive leaves on the amount of oleuropein and extraction yield were investigated. The summary of the experiments and obtained oleuropein amounts is given in Table 2.

When aqueous solvents were used instead of their pure forms, a larger quantity of oleuropein was produced. This is explained by the fact that water distends the cells of plants and facilitates diffusion. Higher oleuropein yield was obtained when the particle size of the raw material to be utilized for extraction was lowered. Increasing the extraction time and using 80% methanol as solvent resulted in significant improvement in oleuropein yield. In contrast, the use of pre-processed olive leaves in the extraction process resulted in a serious decrease in the oleuropein yield. The largest quantity of oleuropein and extraction efficiency were obtained from olive leaves with a particle size of 250-500 μm during an 8-h extraction with an 80 percent methanol solution as the solvent. Under these circumstances, the greatest oleuropein concentration was found to be 13.35 mg g⁻¹ of dried leaves, with a 36% extraction efficiency.

Table 2. Comparison of oleuropein amounts obtained in different experiments

ExpNo.	Solvent type	Time	Particle size (µm)	Oleuropein amount (mg/g dry leaf)
1	80% MetOH	8 h	250-500	13.35
2	80% EtOH	8 h	250-500	12.44
3	80% EtOH	4 h	250-500	10.60
4	70% EtOH	8 h	250-500	9.11
5	80% MetOH	4 h	250-500	8.79
6	Pure MetOH	8 h	250-500	8.34
7	50% EtOH	8 h	250-500	7.52
8	20% ACN	8 h	250-500	6.72
9	70% EtOH	4 h	250-500	6.61
10	20% ACN	4 h	250-500	6.40
11	80% EtOH	4 cycles	250-500	5.40
12	50% MetOH	8 h	250-500	5.31
13	Pure EtOH	8 h	250-500	5.27
14	20% EtOH	8 h	250-500	4.31
15	Pure MetOH	4 h	250-500	4.13
16	Pure MetOH	4 cycles	250-500	3.90
17	Pure EtOH	4 h	250-500	3.70
18	50% EtOH	4 h	250-500	3.44
19	Pure EtOH	4 cycles	250-500	2.78
20	50% MetOH	4 h	250-500	2.05
21	20% EtOH	4 h	250-500	1.28
22	Water	4 cycles	250-500	0.85
23	Water	8 h	250-500	0.48
24	Water	4 h	250-500	0.33
25	Pure MetOH	4 cycles	900-2000	0.07
26	80% EtOH	4 cycles	900-2000	0.06
27	Pure EtOH	4 cycles	900-2000	0.05
28	Water	4 cycles	900-2000	0.03

Acknowledgement

The authors greatly acknowledge “Environmental Research and Development Center” for HPLC analyses and “Center for Materials Research” for characterization analyses at Izmir Institute of Technology Integrated Research Center.

Author contributions

Yaşar Kemal Receptoğlu: Writing – Original draft preparation, Visualization. **Gülin Gümüşbulut:** Investigation, Writing-Original draft preparation. **Aslı Yüksel Özsen:** Supervision, Writing-Reviewing and Editing.

Conflicts of interest

The authors declare no conflicts of interest.

References

1. Chikezie, P. C., Ibegbulem, C. O., & Mbagwu, F. N. (2015). Bioactive Principles from Medicinal Plants. *Research Journal of Phytochemistry*, 9(3), 88–115.
2. Del, D., Rodriguez-mateos, A., Spencer, J. P. E., Tognolini, M., Borges, G., & Crozier, A. (2013). Dietary (Poly)phenolics in Human Health: Structures, Bioavailability, and Evidence of Protective Effects Against Chronic Diseases. *Antioxidants & Redox Signaling*, 18(14), 1818–1892.

3. Bayraktar, O., Köse, M. D., & Baspinar, Y. (2019). Development of olive leaf extract loaded fibroin microparticles by spray drying. *The Open Drug Discovery Journal*, 13, 39–45.
4. Wissam, Z., Ali, A., & Rama, H. (2016). Optimization of extraction conditions for the recovery of phenolic compounds and antioxidants from Syrian olive leaves. *Journal of Pharmacognosy and Phytochemistry*, 5(5), 390.
5. Nenadis, N., Vervoort, J., Boeren, S., & Tsimidou, M. Z. (2007). Syringa oblata Lindl var. alba as a source of oleuropein and related compounds. *Journal of the Science of Food and Agriculture*, 87(1), 160–166.
6. Omar, S. H. (2010). Oleuropein in olive and its pharmacological effects. *Scientia Pharmaceutica*, 78(2), 133–154.
7. Soler-Rivas, C., Espiñ, J. C., & Wichers, H. J. (2000). Oleuropein and related compounds. *Journal of the Science of Food and Agriculture*, 80(7), 1013–1023.
8. Puerta, R. De, Gutierrez, V. R., & Hoult, J. R. S. (1999). Inhibition of Leukocyte 5-Lipoxygenase by Phenolics from Virgin Olive Oil. *Biochemical Pharmacology*, 57(4), 445–449.
9. Bisignano, G., Tomaino, A., Cascio, R. L. O., & Crisafi, G. (1999). On the In-vitro Antimicrobial Activity of Oleuropein and Hydroxytyrosol. *Journal of Pharmacy and Pharmacology*, 51(8), 971–974.
10. Maria, P., Marino, A., Saija, A., Uccella, N., & Bisignano, G. (2002). In vitro antimycoplasmal activity of oleuropein. *International Journal of Antimicrobial Agents*, 20(4), 293–296.

11. Lee-huang, S., Lin, P., Zhang, D., Wook, J., Bao, J., Sun, Y., Chang, Y., Zhang, J., & Lee, P. (2007). Discovery of small-molecule HIV-1 fusion and integrase inhibitors oleuropein and hydroxytyrosol: Part I. Integrase inhibition. *Biochemical and Biophysical Research Communications*, 354(4), 872–878.
12. Visioli, F., Galli, C., & Galli, G. (2002). Biological activities and metabolic fate of olive oil phenols. *European Journal of Lipid Science and Technology*, 104(9-10), 677–684.
13. Visioli, F., Bogani, P., & Galli, C. (2006). Healthful Properties of Olive Oil Minor Components. *Olive Oil (Second Edition) Chemistry and Technology*, Editor(s): Dimitrios Boskou, AOCS Press, 173–190.
14. Ghelichkhani, G., Modaresi, M. H., Rashidi, L., Shariatifar, N., Homapour, M., & Arabameri, M. (2019). Effect of the spray and freeze dryers on the bioactive compounds of olive leaf aqueous extract by chemometrics of HCA and PCA. *Journal of Food Measurement and Characterization*, 13(4), 2751–2763.
15. Piacentini, E., Mazzei, R., Bazzarelli, F., Ranieri, G., Poerio, T., & Giorno, L. (2019). Oleuropein aglycone production and formulation by integrated membrane process. *Industrial & Engineering Chemistry Research*, 58(36), 16813–16822.
16. da Rosa, G. S., Vanga, S. K., Garipey, Y., & Raghavan, V. (2019). Comparison of microwave, ultrasonic and conventional techniques for extraction of bioactive compounds from olive leaves (*Olea europaea* L.). *Innovative Food Science & Emerging Technologies*, 58, 102234.
17. Naleini, N., Rahimi, M., & Heydari, R. (2015). Oleuropein extraction using microfluidic system. *Chemical Engineering and Processing: Process Intensification*, 92, 1–6.
18. Jaski, J. M., Barão, C. E., Liao, L. M., Pinto, V. S., Zanoelo, E. F., & Cardozo-Filho, L. (2019). β -Cyclodextrin complexation of extracts of olive leaves obtained by pressurized liquid extraction. *Industrial Crops and Products*, 129, 662–672.
19. Yateem, H., Afaneh, I., & Al-Rimawi, F. (2014). Optimum conditions for oleuropein extraction from olive leaves. *Applied Science and Technology Magazine*, Corpus ID: 212474866
20. Yasemi, M., Heydarinasab, A., Rahimi, M., & Ardjmand, M. (2017). Microchannels effective method for the extraction of oleuropein compared with conventional methods. *Journal of Chemistry*, 2017.
21. Baldino, L., Della Porta, G., Osseo, L. S., Reverchon, E., & Adami, R. (2018). Concentrated oleuropein powder from olive leaves using alcoholic extraction and supercritical CO₂ assisted extraction. *The Journal of Supercritical Fluids*, 133, 65–69.
22. del Mar Contreras, M., Lama-Muñoz, A., Espínola, F., Moya, M., Romero, I., & Castro, E. (2020). Valorization of olive mill leaves through ultrasound-assisted extraction. *Food Chemistry*, 314, 126218.
23. Lama-Muñoz, A., Contreras, M. del M., Espínola, F., Moya, M., Romero, I., & Castro, E. (2019). Optimization of oleuropein and luteolin-7-O-glucoside extraction from olive leaves by ultrasound-assisted technology. *Energies*, 12(13), 2486.
24. Dal, O., Şengün, D., Yüksel-Özşen, A. (2020). Ultrasound assisted extraction for the recovery of phenolic compounds from waste hazelnut shell. *Environmental Research and Technology*, 3(3), 135–146.
25. Azmin, S. N. H. M., Manan, Z. A., Alwi, S. R. W., Chua, L. S., Mustafa, A. A., & Yunus, N. A. (2016). Herbal processing and extraction technologies. *Separation and Purification Reviews*, 45(4), 305–320.
26. Luque de Castro, M. D., & Priego-Capote, F. (2010). Soxhlet extraction: Past and present panacea. *Journal of Chromatography A*, 1217(16), 2383–2389.
27. Japón Luján, R., Priego Capote, F., Marinas, A., & Luque De Castro, M. D. (2008). Liquid chromatography/triple quadrupole tandem mass spectrometry with multiple reaction monitoring for optimal selection of transitions to evaluate nutraceuticals from olive-tree materials. *Rapid Communications in Mass Spectrometry*, 22(6), 855–864.
28. Xynos, N., Papaefstathiou, G., Gikas, E., Argyropoulou, A., Aligiannis, N., & Skaltsounis, A.L. (2014). Design optimization study of the extraction of olive leaves performed with pressurized liquid extraction using response surface methodology. *Separation and Purification Technology*, 122, 323–330.
29. Zun-qiu, W. U., Gui-zhou, Y. U. E., Qing-ping, Z. H. U., You-jun, J., & Kai-yu, T. (2015). Purification, Dynamic Changes and Antioxidant Activities of Oleuropein in Olive (*Olea Europaea* L.) Leaves. *Journal of Food Biochemistry*, 39(5), 566–574.
30. Lamprou, G. K., Vlysidis, A., Tzathas, K., & Vlyssides, A. G. (2020). Statistical optimization and kinetic analysis of the extraction of phenolic compounds from olive leaves. *Journal of Chemical Technology & Biotechnology*, 95(2), 457–465.
31. Cho, W.Y., Kim, D.H., Lee, H.J., Yeon, S.J., & Lee, C.H. (2020). Evaluation of Effect of Extraction Solvent on Selected Properties of Olive Leaf Extract. *Journal of Food Quality*, 2020.
32. Kirbaşlar, Ş.İ., & Şahin, S. (2021). Recovery of Bioactive Ingredients from Biowaste of Olive Tree (*Olea europaea*) using Microwave-Assisted Extraction: A Comparative Study. *Biomass Conversion & Biorefinery*, 1–13.
33. Ozturk, M., Altay, V., Gönenç, T. M., Unal, B. T., Efe, R., Akçiçek, E., & Bukhari, A. (2021). An Overview of Olive Cultivation in Turkey: Botanical Features, Eco-Physiology and Phytochemical Aspects. *Agronomy*, 11(2), 295.
34. Le Floch, F., Tena, M. T., Ríos, A., & Valcárcel, M. (1998). Supercritical fluid extraction of phenol compounds from olive leaves. *Talanta*, 46(5), 1123–1130.
35. Lee, M. R., Lin, C. Y., Li, Z. G., & Tsai, T. F. (2006). Simultaneous analysis of antioxidants and preservatives in cosmetics by supercritical fluid extraction combined with liquid chromatography-mass spectrometry. *Journal of Chromatography A*, 1120(1–2), 244–251.
36. Demirkaya, E., Dal, O., & Yüksel, A. (2019). Liquefaction of waste hazelnut shell by using sub-and

- supercritical solvents as a reaction medium. *The Journal of Supercritical Fluids*, 150, 11–20.
37. Mazaheri, H., Lee, K. T., Bhatia, S., & Mohamed, A. R. (2010). Sub/supercritical liquefaction of oil palm fruit press fiber for the production of bio-oil: effect of solvents. *Bioresource Technology*, 101(19), 7641–7647.
 38. Şahin, S., Bilgin, M., & Dramur, M. U. (2011). Investigation of oleuropein content in olive leaf extract obtained by supercritical fluid extraction and soxhlet methods. *Separation Science and Technology*, 46(11), 1829–1837.
 39. Garcia-Castello, E. M., Rodriguez-Lopez, A. D., Mayor, L., Ballesteros, R., Conidi, C., & Cassano, A. (2015). Optimization of conventional and ultrasound assisted extraction of flavonoids from grapefruit (*Citrus paradisi* L.) solid wastes. *LWT-Food Science and Technology*, 64(2), 1114–1122.
 40. Xie, J.-H., Dong, C., Nie, S.-P., Li, F., Wang, Z.-J., Shen, M.-Y., & Xie, M.-Y. (2015). Extraction, chemical composition and antioxidant activity of flavonoids from *Cyclocarya paliurus* (Batal.) Iljinskaja leaves. *Food Chemistry*, 186, 97–105.
 41. Medina-Torres, N., Ayora-Talavera, T., Espinosa-Andrews, H., Sánchez-Contreras, A., & Pacheco, N. (2017). Ultrasound assisted extraction for the recovery of phenolic compounds from vegetable sources. *Agronomy*, 7(3), 47.
 42. Nagy, B., & Simándi, B. (2008). Effects of particle size distribution, moisture content, and initial oil content on the supercritical fluid extraction of paprika. *The Journal of Supercritical Fluids*, 46(3), 293–298.
 43. Irakli, M., Chatzopoulou, P., & Ekateriniadou, L. (2018). Optimization of ultrasound-assisted extraction of phenolic compounds: Oleuropein, phenolic acids, phenolic alcohols and flavonoids from olive leaves and evaluation of its antioxidant activities. *Industrial Crops & Products*, 124, 382–388.
 44. Xie, P., Huang, L., Zhang, C., & You, F. (2013). Reduced pressure extraction of oleuropein from olive leaves (*Olea europaea* L.) with ultrasound. *Food and Bioproducts Processing*, 93, 29–38.



© Author(s) 2023. This work is distributed under <https://creativecommons.org/licenses/by-sa/4.0/>



Determination of optimum design parameters of glow plug and experimental verification

Muciz Özcan *¹, Muhammed Fahri Ünlerşen ¹, Mehmet Şen ²

¹Necmettin Erbakan University, Department of Electric and Electronics, Türkiye

²Social Sciences University of Ankara, Distance Education Application and Research Center, Türkiye

Keywords

Glow plug
Mutually inductance
Resistive element
Thermal imaging

Research Article

DOI: 10.31127/tuje.1062681

Received: 25.01.2022

Accepted: 10.03.2022

Published: 26.04.2022

Abstract

In Diesel Engines, the heat energy obtained from the glow plug increases the engine's ability to start up in cold climatic conditions and significantly reduces emissions of harmful gases leaving the exhaust. In cold climatic conditions, before the start off of diesel vehicles it is necessary to wait for about 10 s the cylinder block heating. This period negatively affects driving comfort. In this study, the mathematical results of the processes to optimize the time required for the glow plug to reach the required temperature have been experimentally proven. A test apparatus was developed to confirm experimentally the theoretical results. Thanks to these improvements concerning the manufacture of the glow plug, the time period to reach 850 °C has been reduced by approximately 5 s. The proposed design is in accordance with the glow plug present in the market. Currently the whole glow plug must be changed at the end of lifetime, with our improvement only the inner tube resistance can be easily changed involving a cost reduction by about 60%.

1. Introduction

Diesel engines are becoming increasingly widespread in transportation and freight transport due to their high efficiency and development torque [1-3]. They have an internal combustion ignition system where fuel is sprayed on compressed air heated at approximately 700 °C - 900 °C inside the cylinder. In cold climate countries among the numerous problems that can affect the operation of diesel vehicles, one of the most important is the start off. Especially in the winter months, the cold engine block prevents the first run. In fact, the external low temperature affects the temperature of the cylinder block, which must be preheated to trig the fuel ignition [4-5]. The unburned mixture with a high fuel mixture ratio is release to atmosphere by the exhaust. Gas released to the atmosphere causes the release of toxic greenhouse gases to the environment [6-10]. At this moment, the burning event does not take place properly causing engine knockings [11]. In order avoid the mechanical abrasions between the motor and the

transmission components and also to improve the driving comfort, diesel vehicles use a Glow Plug (GP).

Before the diesel engine start off, the heating element within the GP must be activated during about 10 to 20 s depending on the volume of combustion chambers. At the end of this time, the tip surface of the GP reaches a temperature between about 800 to 1000 °C allowing a comfortable engine start [12]. By using the GP, the smoke released from the engine during the start off is reduced from about 49 % to 60% [13-14]. Since the GP transforms the electrical energy of the battery to a thermal energy, prolonging the preheating temperature is shortening the lifetime of the car battery.

The diesel engine consists on at least four-cylinder blocks which contains a separate GP. Each of them must have the same properties to allow approximately the same ignition conditions for insuring the driving comfort. If not mechanical snags and exhaust gas emissions can be occurred.

In this study, GP used in diesel cars using 12 V supply voltage was targeted and product improvement studies that can be done in GP manufacturing.

* Corresponding Author

(mozcan@erbakan.edu.tr) ORCID ID 0000-0001-5277-6650
(mfunlersen@erbakan.edu.tr) ORCID ID 0000-0001-7850-6712
(mehmet.sen@asbu.edu.tr) ORCID ID 0000-0001-7609-2210

Cite this article

Özcan, M., Ünlerşen, M. F., & Şen, M. (2023). Determination of optimum design parameters of glow plug and experimental verification. Turkish Journal of Engineering, 7(2), 125-133

2. Technical Background of GP

The GP contains four main elements; Glowing Tube (GT), Electrical Insulator (between heating resistance

and GT), Insulator Ring (between connection terminal and body) and Heating Element (HE). The former consists of Heating Resistor (HR) and a Regulating Resistor (RR). These parts are shown in Fig. 1.

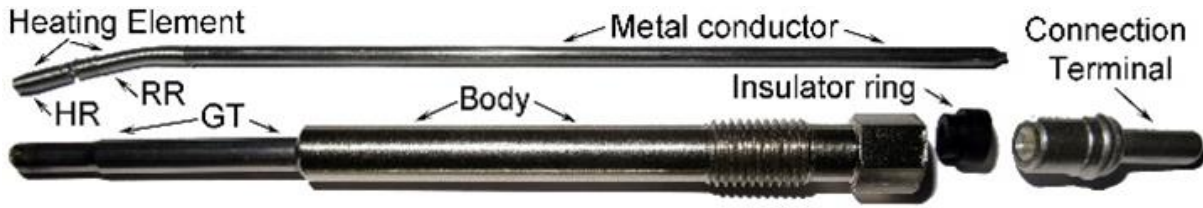


Figure 1. The basic parts of the GP and the assembly sequence

2.1. Selection of GT Material

The most important task of GT is to transfer the heat coming from the HR into the engine block with the lowest energy loss. This is the most important feature expected from GT in GPs. During the engine working, the GT must be resisted to high the internal temperature (1500-2000°C) and without being corroded.

In order to switch on and to enable the working of the HE (positive), the GP is connected the chassis (negative). For this reason, the protective sheath must be

an electrically conductive material. A hollow rod tube made of Inconel ASTM / UNS 310 / 310S stainless steel material was selected as material meeting the requirements specified in this study. Physical properties of 310S Stainless Steel are in Table 1 [15]. If the protective sheath is an insulating material (e.g., ceramics), it must be removed from the protective jacket and must be connected at both ends of the HE. This will involve an additional workmanship and cost.

Table 1. Physical properties of 310S stainless steel

Density (at 25°C)	Thermal Conductivity (at 100°C)	Melting Point	Specific Heat Capacity	Electrical Resistivity (at 25°C)
8 g.cm ⁻³	14.2 W.m ⁻¹ .°C ⁻¹	1400°C	500 J.kg ⁻¹ .°C ⁻¹	0.78 Ω.m

2.2. Electrical Insulation between Heating Coil and GT

The electrical insulating material between the HE and the GT in the GP should be thermally conductive. Moreover, it must be able to prevent oxidation of the heating wire, maintain its insulating property at high temperatures, and easily enter between the GT and the

HE. In this study, magnesium oxide (MgO) was chosen as the material providing these properties. Its physical properties are shown in Table 2 [16]. Since MgO absorbs ambient moisture very quickly, it must be dried in the oven at about 100 °C before using. Unless the GT can be oxidized and be deformed resulting in shortening of the lifetime of the resistance element.

Table 2. Physical properties of MgO

Appearance	Melting point (°C)	Density (g.cm ⁻³)	Thermal conductivity (W.m ⁻¹ .K ⁻¹)
White Powder	2830	3.58	45-60

2.3. The Insulator Ring

The insulation material inside the GT must not only avoid the conductivity between the positive lead and the vehicle's chassis (negative lead), but also withstand the motor temperature. In this study, a ring-insulation element is made of a polypropylene-based material which melting temperature is at about 160 °C.

2.4. Heating Element

The HE is used to heat the GT up to 800 °C - 1000 °C in optimum time. It consists of two resistance elements (HR and RR) connected in series showing in Fig.2. The heating temperature is provided by the HR, while the RR is used to limit the current in the circuit. The RR is essential to prevent the GT from reaching its melting

temperature. The total resistance values of the HR and the RR must be initially small, so that the GT can quickly reach the desired temperature value. When a voltage is applied to these HEs, a large current flows through the first switch.

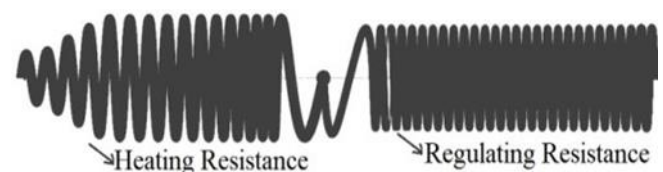


Figure 2. Scheme of heating element (HR and RR)

If the GPs are permanently switched on, they will draw more current than the battery (each GP draws a current of about 12 A), which shortens the life of the battery and negatively impacts the charge. In order to

overcome this drawback, the resistance of the HR should slightly change, while the resistance of the RR should increase more rapidly. In order to provide the necessary features in this work, it is considered suitable to use

Kantal A [17] or D [18] as HR and Nickel 201 as RR. Physical properties of the materials used in the study are presented in Table 3.

Table 3. Physical properties of Kanthal A and Nickel 201

Items	Kanthal A	Nickel 201
Density (g.cm ⁻³)	7.15	8.89
Electrical resistivity at 20°C (μΩ.m)	1.39	0.096
Melting point	1500 °C	1435 °C
Thermal conductivity (W.m ⁻¹ .K ⁻¹)	11 (at 50°C)	67.1 (at 100°C)
Temperature factor of resistivity at 800°C	1.05	0.46

3. Material and Method

The design parameters of the HR and RR must be determined appropriately to ensure that the GT reaches the required temperature. It is necessary to determine the cross-section and length of the RR and HR conductors and how they should be wrapped around the winding diameter. First of all, it is necessary to determine the total resistance value to reach the required temperature of the GT to be generated by the current that will flow through the HR. The amount of heat required to reach the desired temperature of the GT can be calculated from Eq. (1).

$$Q = m.c.(T_f - T_s) \tag{1}$$

Where; Q: the amount of heat (cal) to be supplied to the GT; m: mass of the heating zone (gr); c: specific heat of the GT (cal.gr⁻¹.°C⁻¹); Tf and Ts are the final and starting temperatures (°C) of the metal sheath. Initially, the HR must be able to generate this amount of heat in a very short time. From here, the amount of power that the HR must give every second can be calculated from Eq. (2).

$$P = 0,239 \cdot Q \text{ (1 W = 0,239 cal/s)} \tag{2}$$

The value of the HR to obtain the required heat can be calculated from Eq. (3).

$$R = U^2/P \tag{3}$$

Where; P is the amount of power that the HE must produce (W); U is the operating voltage of the HR (U is the battery voltage of the vehicle to be used). The length of the conductor required to obtain the heating resistance can be calculated from Eq. (4).

$$L = R \cdot A/\rho \tag{4}$$

Where; ρ is the resistivity (Ω.m), R is the electrical resistance of the material (Ω), L is the size of the material (m), A is the cross-sectional area of the material (m²).

In practice, the operating voltages of the GPs are 5, 12 or 24 V. In Sea vehicles and small vehicles 5 V, automobiles 12 V, trucks, large vehicles such as TIR 24 V is used. For cars with a 12 V battery supply, an energy of about 150 W.s⁻¹ must be provided in the GP cylinder. In this case, the total resistance of each HE can be calculated as R = 122/150 = 0.96 from Eq. (3). This study was done for 12 V GP used in automobile. When calculating the values for the HE, the heat transfer losses of the metal air heating and insulation materials were not taken into account at the beginning. In order to accurately estimate the value of the correction coefficient, a sample was first generated according to the data obtained from the calculations. A correction coefficient is obtained from the experimental results of the sample. The values of both HE and RR were re-determined with the obtained coefficient. The values obtained by taking the correction coefficient into account are given in Table 4.

Table 4. Technical values of HR and RR according to 12 V GP

Element	Material diameter (mm)	Number of turns	Winding diameter (mm)	Resistance (Ω; at 20 °C)	Resistance (Ω; at 800 °C)	Resistance (Ω; at 1100 °C)
HR	0.40	10	1.95	0.677	0.697	0.706
RR	0.25	26	2	0.319	1.530	1.797
HE	-	-	-	0.997	2.228	2.503

The resistance of the HR is slightly increasing while the one of RR increases abruptly with temperature. The change values of the total resistance 12 V GP of HE values depending on the temperature are given in Tab. 4.

The diffusion of heat along the GT induces the flow down of the current on both resistances; therefore, the

temperature is decreasing with time. This is the reason why the melting temperature of the GT is never reached.

In Fig. 2, each of the elements used as resistors in the heating have a self-inductive value. It is well known that a solenoid inductor can be calculated from low frequencies, we can calculate the inductance using as Eq. (5) [19].

$$L = \frac{N^2 \cdot \mu_0 \cdot \mu_r \cdot A}{l} \quad (5)$$

The electrical equivalent circuit of the GP is shown in Fig. 3.

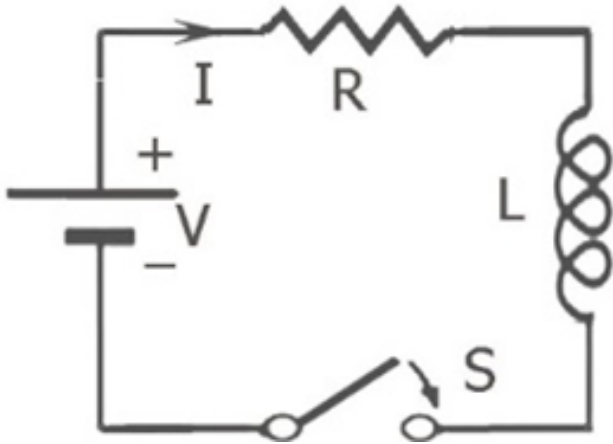


Figure 3. Electrical equivalent circuit of the GP

In Fig. 3, R represents the total resistance of the HEs and L represents the total inductance of the HEs. Using the modified Kirchhoff's rule for increasing current, dI/dt , the R-L circuit is described by the following differential Eq. (6).

$$V - I \cdot R - L \frac{dI}{dt} = 0 \quad (6)$$

Integrating over both sides and imposing the condition $I(t=0) = 0$, the solution to the differential equation is given in (7).

$$I(t) = \frac{V}{R} (1 - e^{-t \cdot L/R}) \quad (7)$$

In order to reach the V / R value in a very short time the circuit current must be as low as possible and R value as large as possible. If this time is too high, the heat generated by the HE in the GP will cause the heating tube to travel along the metal jacket to the body of the engine block. In this case, the heat to be delivered into the engine block will cause the desired temperature to reach a much longer time. As a result, the heat generated from the HTs cannot be used in a desired manner, which will cause unnecessary power retraction from the battery that will reduce the efficiency of the system and cause the vehicle to operate for a longer period of time. Reducing the minimum inductor value of the GT ensures that the current through the heating coil reaches its nominal value in a very short time, thus eliminating the above-mentioned drawbacks. The connection forms of the resistance wires to reduce the total inductor value as much as possible are shown in Fig. 4. Cumulatively Coupled Series Inductors (CCSI) are shown in Fig. 4(a), Differentially Coupled Series Inductors (DCSI) are shown in Fig. 4(b), and Proposed Method Inductors (PMI) are shown in Fig. 4(c).

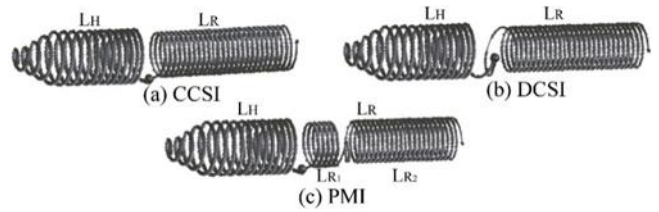


Figure 4. Winding patterns of HR and RR a) CCSI, b) DCSI, c) PMI

The process to reduce the total inductance value of the HR and the RR is as follows.

3.1. CCSIs

If the HR and the RR are wound in the same direction and are connected in series as shown in Fig. 4(a), the total ohmic resistances are $R = RR + RH$. Where: R: Total resistance, RR: Regulating coil of Resistance (Ω) and RH: Heating coil of Resistance (Ω). Because the form of winding does not affect the values of the HR and RR, other winding methods do not change the impedance values. Therefore, this equation will be the same for the three winding methods.

The total inductance is $L = LR + LH$. Where, LR is the regulating coil of inductor value (H) and LH is the heating coil of inductor (H). Since these resistors are placed in a conductive metal tube, mutual inductance between LR and LH occurs. In this study, the size and cross-section of the conductor to be used in the HR and RR are predetermined. As can be understood from the Eq. (4), while winding the resistors in the form of a coil, the winding radius should be kept as small as possible so that the inductor values are small. If the winding directions of the heating resistance wire and the balancing resistance wire are the same, the total inductance value can be calculated from Eq. (8) [20].

$$L \frac{dI}{dt} = L_R \frac{dI}{dt} + L_H \frac{dI}{dt} + 2M \frac{dI}{dt} \quad (8)$$

$$L = L_R + L_H + 2M$$

Where; 2M represents the influence of coil LR on LH and likewise coil LH on LR. Eq. (8) can be written as in Eq. (9) in accordance with the operating parameters.

$$L_{Ta} = L_H + L_R + 2M_{HR} = L_H + L_R + 2\sqrt{L_H \cdot L_R} \quad (9)$$

Where; $M_{HR} = \sqrt{L_H \cdot L_R}$; $L_H = \mu N_H^2 \cdot A_H / l_H$; $L_R = \mu N_R^2 \cdot A_R / l_R$; $A_R = \pi D_R^2 / 4$; $A_H = \pi D_H^2 / 4$; $l_H = N_H s_H$; $l_R = N_R s_R$;

LTa; Total inductor of structures, LH: HR's inductor, LR: RR's inductor, MHR: Mutually inductance between HR and RR, NH: Turn number of heating resistance, NR: Turn number of RR, AH: Cross section area of HR (m^2), AR: Cross section area of RR (m^2), lH: Length of HRs (m), lR: Length of RRs (m), DH: Winding diameter of HR, DR: Winding diameter of RR, SH: Resistance diameter of HR, SR: Resistance diameter of RR. The inductor values for this winding type are given in Table 5. This method is not

suitable for winding because our aim in this study is to decrease the total inductor value. Because the mutually inductor value further increases the total inductor value.

3.2. DCSIs

If the HR is wound in one direction and the RR is wound in the opposite direction of the winding resistance and the series is connected as shown in Fig. 4(b). Since the winding directions of the HR wire (LH)

and the RR wire (LR) are different, the total inductance value (LTb) can be calculated from the Eq. (10).

$$L_{Tb} = L_H + L_R - 2M_{HR} = L_H + L_R - 2\sqrt{L_H \cdot L_R} \quad (10)$$

The inductor values for this winding type are given in Table 5. Because our aim in this study is to reduce the total inductor value, this method may also be suitable for winding, because mutually reducing the value of the total inductor value of the inductors.

Table 5. 12 V GP Total inductance values of the HR and the RR in relation to the winding direction

Mutually inductors (μH)	CCSI (μH)	DCSI (μH)
0.196	0.700	0.112

3.3. PMIs

In this study, we aim to approximate the total inductor value to zero, so we propose a new form of winding as shown in Fig. 4(c) as a third method. As seen in Table 6, the total inductor value of the resistors decreases inversely with one another. If we want to reduce this value further, we can further reduce the total inductor value by reversing some of the RR in itself. In

this technique, the heating coil is wound with the winding direction and part of the RR coil being in the same direction. The remaining part of the RR coil is wound in the opposite direction to the first part. When LR in Eq. 10 is substituted by $LR=LR1+LR2-2\sqrt{LR1.LR2}$, the total inductance value (LTc) presented in Eq. (11) can be obtained.

$$L_{Tc} = L_H + \left(L_{R1} + L_{R2} - 2\sqrt{L_{R1} \cdot L_{R2}} \right) - 2\sqrt{L_H \cdot \left(L_{R1} + L_{R2} - 2\sqrt{L_{R1} \cdot L_{R2}} \right)} \quad (11)$$

$$L_{R1} = \mu N_{R1}^2 \cdot A_R / l_{R1}; \quad L_{R2} = \mu N_{R2}^2 \cdot A_R / l_{R2}$$

LTc; Total inductor of proposed structures, LR1: First part of RR’s inductor in proposed model, LR2: Second part of RR’s inductor in proposed model.

The purpose here is to set the mutual impedance value to be $M = (LR + LH) / 2$. Table 6 of the proposed method gives the mutually inductor values for the 12V HR to be formed when the RR is wound in the same direction as the 5-turn HR. The table for the recommended method for 12V GP is given in Table 6.

Resistance values and total inductor values are given in Table 7. Depending on the temperature of 12V GP from Eq. (5), it can be said that the value of the inductor does not significantly depend on the temperature.

Table 6. 12 V GP Inductor values for the proposed method

Resistance	Material diameter (mm)	Winding diameter (mm)	Number of turns	Winding and direction	Mutually Inductors (μH)
HR	0.40	1.95	10	10 same direction	0.0938
RR	0.25	2	26	21 reverse direction	0.3358
RR	0.25	2	26	5 same direction	0.0746

Table 7. Resistance values and total inductor values depending on the temperature of 12 V GP

Temperature (°C)	HR (Ω)	RR (Ω)	HE (Ω)	CCSI (μH)	DCSI (μH)	PMWI (μH)
20	0.677	0.319	0.997	0.896	0.111	≅0
800	0.697	1.530	2.228	0.896	0.111	≅0
1100	0.706	1.797	2.503	0.896	0.111	≅0

Conductor cross-sections of HR and RR are different and are made from different materials. The series connection of the two groups of winding is performed by the welding method shown in Fig. 5(a). The welding process was performed with the laser diode pumped Nd:YAG laser device shown in Fig. 5(b) because the conductor's cross-sections are small and require precise welding operation [21-22].

In this study, the HE was made in the form of a replaceable tube as shown in Fig. 6. Thus, the GP can be easily replaced without removing the part that is mounted on the cylinder block. Therefore, both labor and material savings are provided.



Figure 5. a) Welding of resistance wires b) Laser device



Figure 6. GP's mounting style for changing the HE

3.4. Experimental GP Test Setup

In order to obtain the experimental test results of the designed and manufactured GP, the test setup block diagram is given in Fig. 7.

The assembly of the manufactured sample GP to the test assembly is shown in Fig. 8(a). The voltage and current values applied to the GP the Human Machine

Interface (HMI) screen display is shown in Fig. 8(b). Fig. 8(c) shows the thermal camera image of the end of the GP.

Pyrometer shown in Fig. 8(a) is used for GP tip temperature measurement in this study.

One of the pyrometers (Dias Company's Pyrospot DG 10N / DG 10NV) was used to measure the temperature distribution of the GP end region as shown in Fig. 8(a). This pyrometer has display output and analog output. As can be seen in Fig. 8(c), the temperature distribution of the measurement area can be measured from a display connected to the screen output. The GP tip temperature measurement data was transferred from this pyrometer analogue output to the Programmable Logic Controller (PLC).

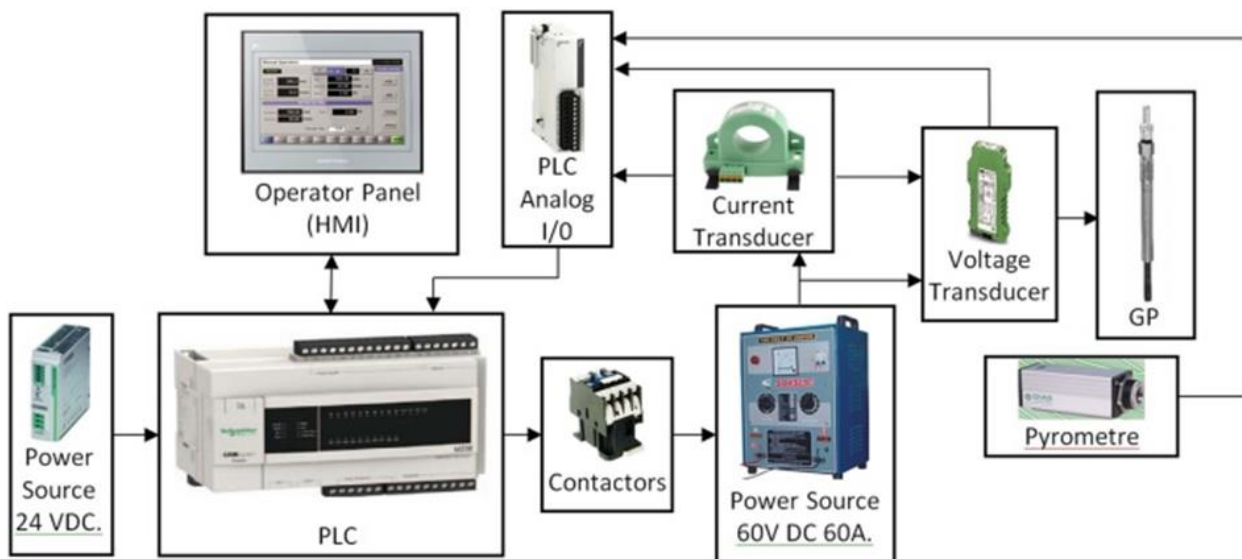


Figure 7. Block diagram of test setup

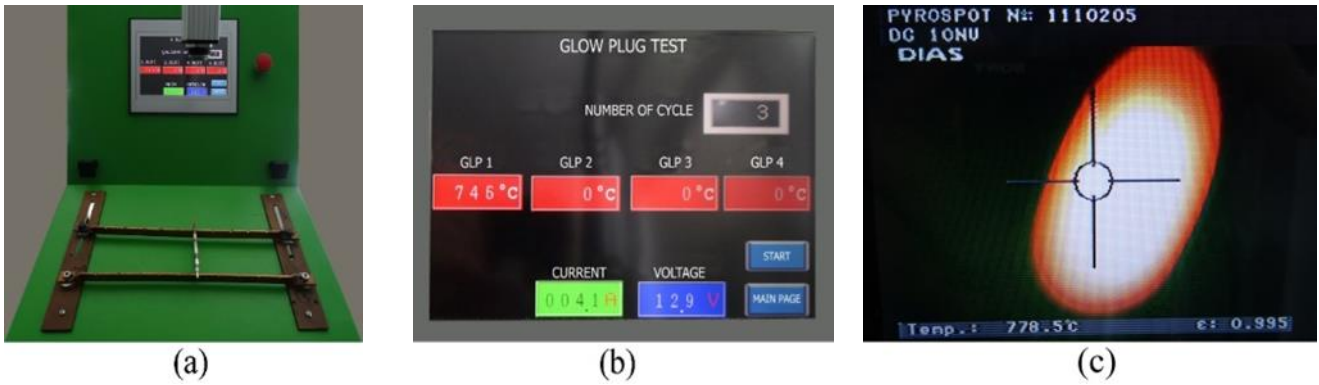


Figure 8. a) Test setup, b) HMI image of test data, c) Thermal camera image

4. Results and Discussion

A 12 V GP was manufactured with three winding techniques, corresponding to the parameters given in the study (Tab. 4 and Tab. 6). The variation of the current and total power consumption of the HE is shown in Fig. 9(a) and Fig 9(b) respectively.

In the proposed novel method, which is understandable from the interpretations of the graph, the current reaches the nominal value very quickly. By using this proposed novel method, it is possible to reach the nominal value of the current in a very short time like 1µs by reducing the total inductor value of the HEs as much as possible. In this case, the temperature of the zone where the glow tube HR is located can reach 800-1000 °C in a short time like 6s without allowing the heat obtained from the HR to spread through the GT. In this study, it was tried to approximate the total value to zero by considering the series connected inductors in the mutually inductor values. Whatever is done, this value cannot be really zero due to even electric power cables that feed GPs have an inductive value. In this study, it was tried to reduce this value as much as possible by the winding method developed.

The pulling of the total inductor value of the GP resistors may be possible by reducing the coil surface area as understood from the Eq. (4). However, it is possible to reduce the surface area of the HR only with a winding of smaller diameter. In this case, it is difficult to transfer the heat from the HR to the GT trough. In this case, the result is that the material used for making the HR reaches the melting point of the material and deteriorates. Therefore, this method is not preferred in this study.

Experimental images of the proposed method and the other methods of GP at the same time are given in Fig. 8. GPs produced with these three methods have been tested together, after applying 12 A at start and waiting 6 s, it can be seen that the heating is low for GP prepared with CCSI, while highly heated but short area is observed with DCSI method and finally highly heated on large area is observed with PMI. Samples are presented in Fig. 10.

In order to obtain the test results according to the three methods mentioned in this study, 4 pieces of GP according to each method were manufactured. The test results of the GPs were obtained as a result of testing the experimental setup one by one. The test results were obtained using the experimental setup given in Fig. 8. When we applied voltage to the GP’s, we started up a chronometer in PLC and recorded the instantaneous temperature time change values depending on the time with the pyrometer which we mounted on the test system. We selected sampling time of 50 ms for this study. The temperature change of each GP was recorded in PLC for a sampling time of 0.5 s. The averages of the test results obtained for each method are shown in the graph of Fig. 11. There are very small temperature changes between GP’s temperatures. This can be interpreted as the sum of a number of errors that can occur up to the time when the resistive wire section used in the production stage of the product is not homogeneous, the delay in PLC sampling time and etc. As can be understood from Fig. 11, at the end of 5 seconds, the GP tip temperature was 670 °C at the CCSI technique, 800 °C at the DCSI technique, and 850 °C at the PMI technique.

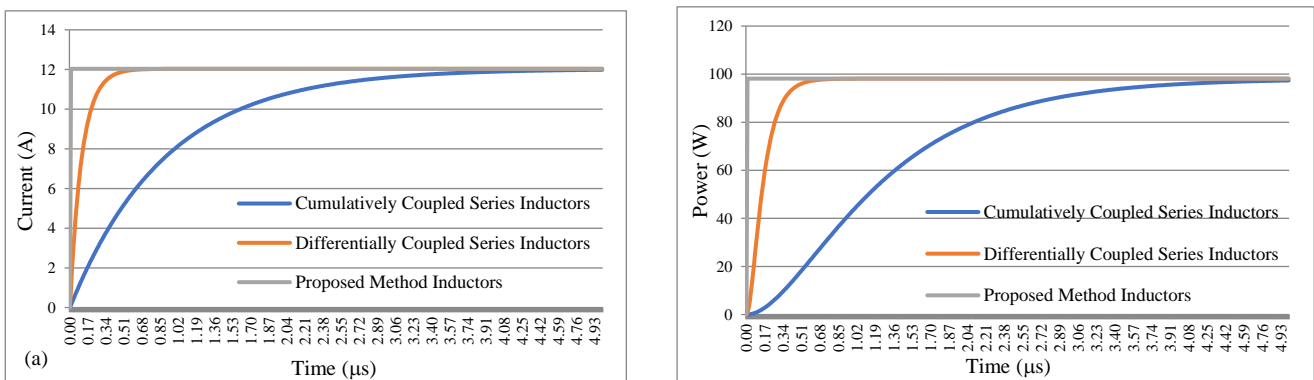


Figure 9. Shows the time-dependent; a) Current b) total power consumption on HE of 12 V GPs manufactured according to three methods

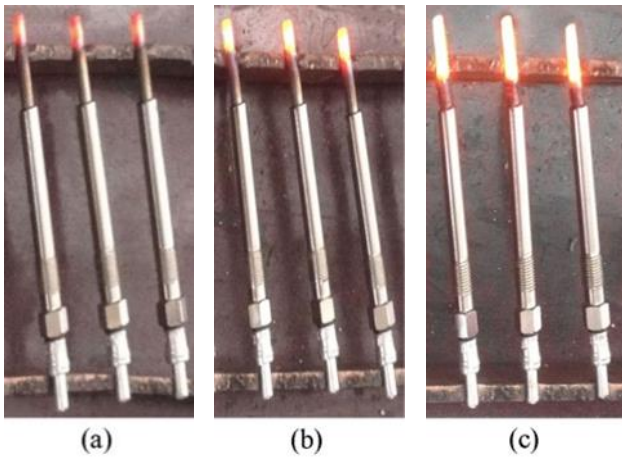


Figure 10. GP of; (a) CCSIs, (b) DCSIs, (c) PMIs.

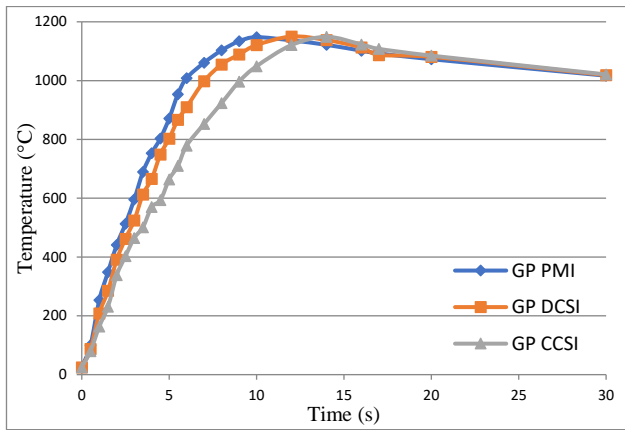


Figure 11. Change of the tip temperatures of the four GP produced by three methods depending on the time

5. Conclusion

In this study, the work to be done on the product was investigated and the results were observed experimentally in order to reduce the duration of warming and to produce standard GP's. With the product improvement work made, the electrical properties of the GP's are made identical and the production GP are provided at 850 ° C for 5 seconds. The standard product is obtained to ensure the combustion of each cylinder block at the same time, preventing greenhouse gas emissions from causing unnecessary mechanical knocking and unnecessary greening of the environment. During the delay in achieving the desired temperature of the GP's during the required time, the heat generated by the GP is absorbed by the cylinder volume, causing the GP to heat up longer and to consume more power from the battery. Thanks to the work done, optimal heat is obtained from reaching the optimum temperature during the optimum time, which prevents unnecessary power consumption from the battery and shortening the battery life. Considering that there are millions of vehicles in the world, the positive effect of any improvement in exhaust emissions on global warming is so important that it cannot be ignored.

Deterioration of the GP's is usually caused by exposure of the outer surface of the HE to corrosive effects or breakage of the resistance material contained

therein. In the event of a malfunction in this work, the GP is replaced by a tube, which requires the most workmanship to replace it. In this case, it is manufactured in such a way that this tube can be easily changed so that maintenance can be done quickly and easily, and the service cost are reduced by 60%. The part of the GP mounted on the engine block has been reduced to prevent the adverse effects on the environment.

Acknowledgement

This study was supported by TUBITAK 1507, 7131171 under Project Number 3080487 from the Industry R&D support program, and by the Scientific Research Projects (BAP) Coordinatorship Office of Necmettin Erbakan University.

Author contributions

Muciz Özcan: Determining the aim and creating the methodology of the study and coordinating the study. Conducting experiments and interpreting the results obtained. **Muhammed Fahri Ünlerşen:** Calculating the indicator value and helping with some calculations. **Mehmet Şen:** Conducting experiments and interpreting the results obtained. Writing-Reviewing and Editing the manuscript.

Conflicts of interest

The authors declare no conflicts of interest.

References

- Özcan, M., & Günay, H. (2013). Control of diesel engines mounted on vehicles in mobile cranes via CAN bus. *Turkish Journal of Electrical Engineering and Computer Science*, 21(Sup. 2), 2181-2190.
- Siskos, P., Capros, P., & De Vita, A. (2015). CO₂ and energy efficiency car standards in the EU in the context of a decarbonisation strategy: A model-based policy assessment. *Energy Policy*, 84, 22-34.
- Peng, B. B., Fan, Y., & Xu, J. H. (2016). Integrated assessment of energy efficiency technologies and CO₂ abatement cost curves in China's road passenger car sector. *Energy conversion and management*, 109, 195-212.
- Last, B., Houben, H., Rottner, M., & Stotz, I. (2008, March). Influence of modern diesel cold start systems on the cold start, warm-up and emissions of diesel engines. Paper presented in Proceedings of the 8th Stuttgart International Symposium, Stuttgart, Germany.
- Weilenmann, M., Favez, J. Y., & Alvarez, R. (2009). Cold-start emissions of modern passenger cars at different low ambient temperatures and their evolution over vehicle legislation categories. *Atmospheric environment*, 43(15), 2419-2429.
- Qi, D. H., Bian, Y. Z., Ma, Z. Y., Zhang, C. H., & Liu, S. Q. (2007). Combustion and exhaust emission characteristics of a compression ignition engine using

- liquefied petroleum gas–diesel blended fuel. *Energy conversion and management*, 48(2), 500-509.
7. Kökkülünk, G., Akdoğan, E., & Ayhan, V. (2013). Prediction of emissions and exhaust temperature for direct injection diesel engine with emulsified fuel using ANN. *Turkish Journal of Electrical Engineering & Computer Sciences*, 21(Sup. 2), 2141-2152.
 8. Mrzljak, V., Medica, V., & Bukovac, O. (2017). Quasi-dimensional diesel engine model with direct calculation of cylinder temperature and pressure. *Tehnički vjesnik*, 24 (3), 681-686. <https://doi.org/10.17559/TV-20151116115801>.
 9. He, B. Q. (2016). Advances in emission characteristics of diesel engines using different biodiesel fuels. *Renewable and Sustainable Energy Reviews*, 60, 570-586.
 10. Barna, L., & Lelea, D. (2017). Low pressure injection of oxyhydrogen in turbocharged compression ignition engines. *Tehnički vjesnik*, 24 (Supplement 2), 287-294. <https://doi.org/10.17559/TV-20150921183805>.
 11. Payri, F., Broatch, A., Salavert, J. M., & Martín, J. (2010). Investigation of Diesel combustion using multiple injection strategies for idling after cold start of passenger-car engines. *Experimental Thermal and Fluid Science*, 34(7), 857-865
 12. Endiz, M. S., Özcan, M., Erişmiş, M. A., Yağcı, M., & Günay, H. (2015). The simulation and production of glow plugs based on thermal modeling. *Turkish Journal of Electrical Engineering & Computer Sciences*, 23(Sup. 1), 2197-2207.
 13. Sakunthalai, R. A., Xu, H., Liu, D., Tian, J., Wyszynski, M., & Piaszyk, J. (2014). Impact of cold ambient conditions on cold start and idle emissions from diesel engines (No. 2014-01-2715). SAE Technical Paper.
 14. Bosch, R., & Peter, (Tr.) G. (1996). *Automotive handbook*. Society of Automotive Engineers, US.
 15. Cobb, H. M. (2010). *The history of stainless steel*. ASM International.
 16. Lee, B., Liu, J. Z., Sun, B., Shen, C. Y., & Dai, G. C. (2008). Thermally conductive and electrically insulating EVA composite encapsulants for solar photovoltaic (PV) cell. *eXPRESS Polymer Letters*, 2(5), 357-363.
 17. Kanthal, A. B. (2008). *Thermostatic bimetal handbook*. Hallstahammar, Sweden.
 18. Davis, J. R. (Ed.) (2000). *Nickel, cobalt, and their alloys*. ASM international.
 19. Soohoo, R. (1979). Magnetic thin film inductors for integrated circuit applications. *IEEE Transactions on Magnetics*, 15(6), 1803-1805.
 20. Nilsson, J. W., & Riedel, S. A. (2015). *Electric Circuits*. 10th ed. New Jersey, USA: Pearson.
 21. Siewert, T., Samardžić, I., Kolumbić, Z., & Klarić, Š. (2008). On-line monitoring system-an application for monitoring key welding parameters of different welding processes. *Tehnički vjesnik*, 15(2), 9-18.
 22. Özcan, M. (2003). *The design and application of an effective power supply for Nd:YAG laser used on machining of various materials*. Doctoral Thesis, Selçuk University, Council of Higher Education Thesis Center, Konya, 157p



© Author(s) 2023. This work is distributed under <https://creativecommons.org/licenses/by-sa/4.0/>



A four-wall virtual reality visualization of patient-specific anatomy: Creating full user immersive experience from computed tomography scans

Hesham Tanbour¹, Emad Tanbour*²

¹University of Illinois at Chicago, College of Medicine, USA

²Eastern Michigan University, School of Engineering, USA

Keywords

Virtual Reality in Medicine
Patient-Specific Anatomy Simulation
Tomography
Tracking
Simulation

Research Article

DOI: 10.31127/tuje.1072285

Received: 12.02.2022

Accepted: 30.03.2022

Published: 26.04.2022

Abstract

Virtual reality is the future of medical imaging diagnosis. Previous studies have introduced virtual reality rendering of anatomical models while others have mentioned processes to extract 3D models from Computed Tomography (CT) images. In this study, we provide a detailed workflow to transforming patient-specific two-dimensional (2D) CT dicom format imaging files to three-dimensional (3D) immersive, dynamic and interactive anatomical assembly models while incorporating them into a four-wall virtual reality environment system. Our study implemented 3D CAD and virtual reality capacities through software and engineering design tools to transform 2D medical images into interactive 3D models in our system. In doing so, the user was able to gain a sense of depth, scale, and dimensionality while immersed in the environment and while implementing interactive tools to investigate patient-specific hip-femur dynamics. At the same time, users were able to identify key anatomical landmarks in the patients' hip joints. Applications of the VR system to the medical field and orthopedics, in particular, were discussed.

1. Introduction

In this paper, we present the unique set-up we developed to visualize and produce medical imaging into the VR environment. The difference between our 4-wall VR system and head mounted displays HMD VR experience is demonstrated. The presented 4-wall virtual environment is a fully immersive virtual reality (VR) environment that consists for a collection of screens with rear projection of content visualized in space through the use of head mounted devices or 3D glasses, an integration system of software, and multiple projector-screen apparatuses. The presented 4-wall VR system submerses the viewer in the constructed virtual world allowing for interaction, body/head tracking, haptic feedback and visualization capabilities unlike any other. In addition, the presented system systems give users room to move physically and further experience the immersive environment compared to head-mounted display (HMD) virtual reality systems. The 4-wall VR

system presented in this paper is also a collaboration environment. Since the 3D LCD shutter glasses used do not block the room view of the user, collaboration and group visualization are possible. Efforts have been made to immerse surgeons and patients in renderings of abdominal CT scan data using HMD VR capabilities through their desktop display system were difficult for surgeons. Tcha-Tokey et al., [1] concluded that CAVE VR experiences, similar to our 4-wall VR environment, presented significantly greater user experience (UX) based on both subjective questionnaires and completion time test data that measured presence, engagement, flow, skill, and judgement compared to HMD systems. Another advantage to the 4-wall VR system compared to the HMD setup is the wand, an interactive tool with six degrees-of-freedom, that allows the user to move in space with full tracking and haptic feedback capability during VR simulation person-object interactions as mentioned in [2].

* Corresponding Author

(htanbo2@uic.edu) ORCID ID 0000-0002-0791-3377

(etanbour@emich.edu) ORCID ID 0000-0003-2095-8534

Cite this article

Tanbour, H., & Tanbour, E. (2023). A four-wall virtual reality visualization of patient-specific anatomy: Creating full user immersive experience from computed tomography scans. *Turkish Journal of Engineering*, 7(2), 134-140

2. The case for immersive visualization

Until recently, virtual reality applications have not been used to simulate medical procedure nor conduct medical research to further our understanding of human anatomy and physiology, let alone introduce patient-specific technological capabilities in the world of medicine. Sigitov et al., [3] mention in their work that although most medical professionals use modern three-dimensional (3D) imaging equipment like Computed Tomography (CT) and magnetic resonance imaging (MRI) scanners, most of the information reviewed is in a “slice-wise manner” on a “2D medium” which does not give medical professionals the, sometimes, necessary opportunity to immerse themselves nor interact with the data in an informative manner. While some efforts have been made to immerse users in 3D anatomical structures like blood vessels, Long et al., [4] chose only to provide volume rendering to stop depth perception from being lost and disorienting the user.

Witkowski et al., [5] present work on patient-specific musculoskeletal models of lower limbs for surgical planning interventions with a semi-immersive system, not fully-immersive as with the 4-wall VR system presented, and planning functionality using 2-D display and standard mouse, as opposed to a haptic feedback capable VR wand with full-motion tracking demonstrated in our work. Finally, Al-khalifah et al., [6] present a CAVE experience navigating volumetric medical datasets, yet based on their results, visualization was conducted with only one wall. In our work, we provide a 4-wall immersive and active VR system with head tracking for improved 3D stereoscopic vision capabilities as well as motion tracking to enhance the user’s sense of movement and floating models in space with SolidWorks computer-aided design (CAD) implementation to create joints between members for user interaction. The 4-wall VR demonstrated here provides multi-user interactive and collaborative environment. This is expected to be useful for medical staff collaboration as well as surgeon-patient review of planned procedures. The following paragraph describes the term “Patient-specific personalized medicine” according to the US National Institute of Health, NIH.

As technological advancements in the field of medical data visualization expand, in 2015, all of US research programs known as the Precision Medicine Initiative cohort program were created and are geared on making advancements in individualized treatment plans. The general idea behind precision medicine is the utilization of multiple data streams in analytical work in order to develop better treatments for individuals. This is not to say that certain patients will receive special treatment, rather technological innovation will allow medical professionals to tailor treatment plans to an individual of interest seeking medical attention [7]. Arnold et al., [8] express the fact that there exists little literature on the subject of patient- specific procedure planning and practice, especially efforts aimed at improving patient outcomes. Our work provides a novel step-by-step procedure to creating patient-specific 3D anatomical models from CT scan information and

visualizing these models in a fully immersive 4-wall active VR environment.

3. Methods

In approaching this project, a system of integration mapping out the processes involved in creating the intended virtual reality experience was produced and is shown in Figure 1. Each process is elaborated on in this paper with feedback loops and their justification for incorporation is detailed. In the end, this apparatus allows health care workers and medical professionals to translate vital medical imaging information in virtual reality experiences to extract more information from obtained images.

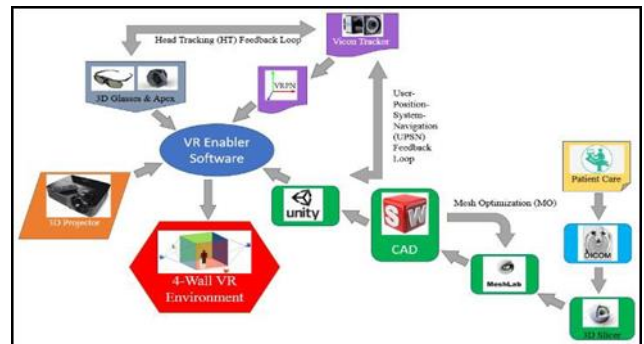


Figure 1. Data and software system integration flowchart for the 4-Wall VR environment.

4. CT Scan Segmentation and Model Development

Publicly available CT scans of patient donors at the University of Iowa Carver College (UICC) of Medicine “Visible Female CT Dataset” was used. With that dataset, CT scans of hip and pelvis body parts were utilized in hopes to recreate the human (female) hip joint, creating an assembly of the two components and utilizing 3D measurement tools to create a coordinate system and point of origin to locate the necessary data points to create a “mate” or 3D connection between the two parts (pelvis and head of femur). More on this matter is discussed further in the document.

For an accurate, high-resolution model to be constructed through 3D slicing software, CT scan files with a larger quantity of slices were of interest. As part of the Magnetic Resonance Research Facility at the UICC,

400 CT scan (.dcm) files were utilized for a female individual hip while 150 CT scan (.dcm) files were obtained which was a total of 550 CT slices that were used in the creation of the 3D model.

3D Slicer® is an open-source software used for bio-imaging informatics, imaging processing, and 3D visualization applications. Through the support of the National Institutes of Health (NIH) and other worldwide developers, the 3D slicer was made possible. The 4.10.2 version was used. The following steps were taken to translate the 2D CT scan (.dcm) scan files to create a 3D model, which was taken to other software platforms for further analysis and adjustment while preserving the integrity of anatomical features of the UICC female hip joint:

1. After launching 3D Slicer, load DICOM files from desktop (after saving the files from UICC website).
2. Go to the Segment Editor module and add a segment
3. Under Effects, select “Threshold” and adjust the intensity range using the slide bar until only human bone is highlighted in the sagittal, coronal and axial views, then click Apply
4. Click “Show 3D” to see the highlighted portions of the CT scan put together into a 3D model shown in the program
5. Next, click “Islands” and under Edit Islands select “Keep largest island”, this will delete all volumes smaller than the largest volume that is intact in the newly created 3D model. As a result, the 3D model now only includes the two-femur head and the pelvis.
6. Add a new segment in order to highlight the femur bone and segment it from the main pelvic structure
7. In order to separate the ball from the socket in this hip-femur joint, the “Paint” tool under “Effects” in the Segment Editor module must be used.
8. Under “Paint”, select the “Sphere brush” and use the shift key and wheel button on the mouse to increase or decrease the diameter of the sphere brush that will be used in the sagittal, coronal, and axial views of 3D Slicer
9. Use the scroll button on the mouse in all three views to find the section where the diameter of the femur head is largest, place the cursor with the sphere brush tool selected, and click to highlight that spherical area in the 3D view
10. Next, select the “Islands” feature under effects and select “Add selected island” and select in any of the three views any part of the femur bone that is highlighted in designated color. The software will add the rest of the femur bone to the isolated femur head
11. The above procedure can be done to the other femur head and bone in add yet another part to the assembly
12. Export the parts individually using the “Export to files” feature in the Segmentations module. The default file format is STL which works well with SolidWorks and MeshLab, two software that will be elaborated on later in the document.
13. In addition to exporting individual parts, export the entire assembly which will be used as one solid model to retrieve necessary dimensions to establish ball and socket joint in SolidWorks Assembly.

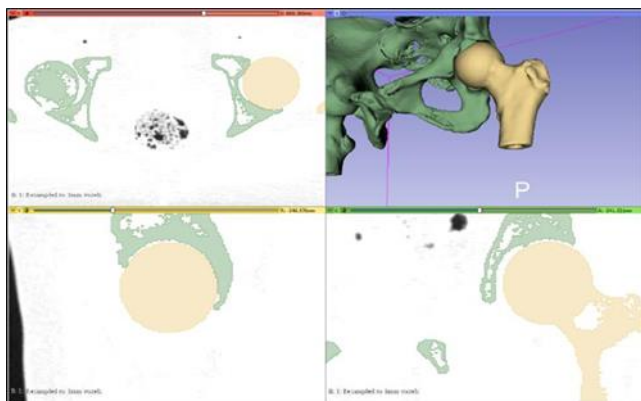


Figure 2. 3D Slicer top-side-front panels and 3D rendering of hip-joint post segmentation process.

STL models exported from 3D Slicer having been created from 550 slides has a high mesh resolution that causes the file size to be anywhere from 30-40 Mb in size. This can burden the user with time waiting for the software to handle such a high- resolution mesh. In order to decrease the file size, re- mesh works and filtering processes must go underway through the MeshLab software, another open-source software designed to edit mesh models along with other capabilities.

In MeshLab, complete the following steps:

- A. Go to File and click on “Import Mesh”
- B. Find the STL file that was created from 3D Slicer
- C. Post-Open Processing window will pop up, click OK to “Unify Duplicated Vertices”
- D. On the top of the menu program, click on the “Wireframe” icon to display the import part as wireframe with the mesh in full display.
- E. Next, go to “Filters” at the top of the window and expand the “Re-meshing, Simplification, and Reconstruction” tab, then select the “Simplification: Quadric Edge Collapse Decimation” option. This option will make polygonal reduction or mesh decimation to decrease the number of faces that complies the model, in order to decrease the total amount of data needed to operate with such model Under “Percentage reduction”, type 0.5 (or 50%) and click Apply. This will tell the software to cut down the total number of faces that complies the model by 50% which preserving the overall geometry of the pelvis or hip, thus keeping the models anatomically accurate and fairly easier to use in other software
- F. Step 6 can be repeated several times until an optimal face count and overall geometrical appearance is met
- G. Export the mesh by going to File and Export mesh. Use STL as the file type to be used in the last software in this integrated CT scan to 3D assembly process: SolidWorks.

5. The Solid-modeling CAD Joint Assembly

Before mating the femur head with the pelvic acetabulum can occur, three-dimensional coordinates and measurements relative to the fixed point of origin must first be established for the assembly of the two to result in an anatomically accurate manner. In order to set up a coordinate system, three planes must be assembled using the 3-2-1 rule of fixturing.

The non-segmented pelvis and femur whole body was imported into SolidWorks. Three points on the top surface of the L4 vertebrae was used to create the Top Plane (z-axis). For the Right Plane (x-axis), the first reference was a perpendicular callout when the Right Plane and the Top Plane. Two additional vertices were chosen along the entire span of the cross-section plane (created by Cropping in 3D Slicer) were used in addition to the perpendicular callout to fix and define the Right Plane. Next, an axis was created from the two above planes. The last plane (Front Plane, y axis) was created using a perpendicularity callout relative to the newly created Axis and a vertex point created on the

superior and anterior portions of the L4 vertebrae. Then, a point was created from the intersection of the Axis line and Front Plane. This point will be used to define the point of origin in the model. Finally, the coordinate system was defined using the three planes mentioned previously and the point of origin previously defined.

Before measurements can be conducted, a uniform spherical surface of the femoral head must be constructed. A handful of triangular faces on the surface of the femoral head mesh were selected to define the new “perfect” spherical surface. Next, a point was defined as the center of the newly formed sphere in order to locate the center coordinates of the femoral head during the measurements.

The measuring tool was used as shown in Figure 3 to define three-dimensional distance from the point of origin and the center of the femoral head. The following coordinates were calculated, with the diameter of the femur head being approximately 23mm: X = 91.882 mm, Y = 42.148 mm, Z = 160.711 mm.

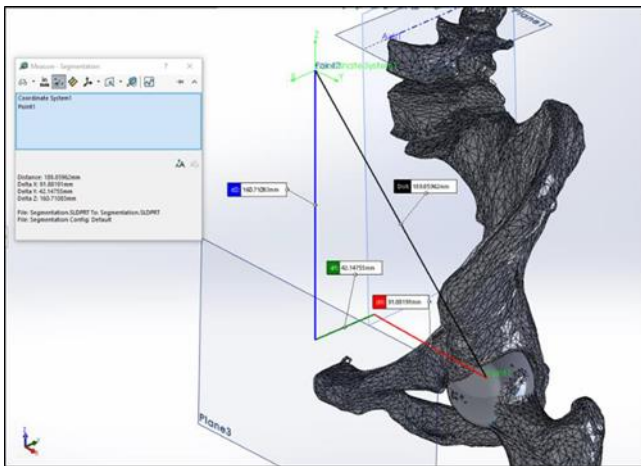


Figure 3. X-Y-Z coordinate system and 3D distance calculation of hip-joint in the solid-modeling software

The same procedure can be applied to the individual hip and femur head components. After the theoretical center of the femoral head is located on the bare pelvis bone, an assembly can be conducted where mating between the theoretical center point of the head and the actual center of the head occurs, thereby joining the two entities back in their original anatomical relative locations, except now allowing freedom of rotation of the femur bone in the socket of the pelvic acetabulum.

In order to return the main axis of the femur bone back to the correct anatomical position found in the CT scans, a cylinder was extruded from a Plane created from 3 points located at the bottom of the section found on the femur bone. An Axis was created from the cylinder. In addition, Right Plane and Front Plane were both used to create another Axis. Angularity between these two axes was determined to be approximately 1.96 deg. Therefore, angular mating between planes and the newly formed axis on the femoral head were performed fixing the femur bone in this correct anatomical location within the acetabular socket.

6. Game-Engine (UNITY 3D Software)

Unity 3D is a software created for the development of digital games but, recently, has been used in several field of study including engineering, medical simulation and architecture. Sigitov et al., [3] have used the platform for rapid prototyping and content generation as has been done in this study. Having successfully modeled the hip-femur assembly in SolidWorks, a SimLab Soft FBX file exporter add-on was used to create the appropriate file type for Unity 3D readiness [9]. A new project was created in Unity in which a pre-fabricated dissection hospital scene obtained from the Unity Asset Store was downloaded and hip-femur joint incorporated. Adjustment to size, lighting, camera, VR node connection and joint physics capabilities (character joint is the term used in Unity) were accounted for in scene production. Real physics applied to the joint were implemented in order to allow the VR user to interact with the anatomical components in the 4-WALL environment. Background C# scripting was performed in communication between Unity software and the VR enabler/Tracker integrated system to allow for head tracking and navigation capabilities by merely walking within the CAVE space as opposed to using a wand for navigation as has been done in the past [10-11-12-13].

7. The 4-Wall VR System Setup

As shown in Figure 4, the 4-WALL consisted of an assembly of 3” x 3” aluminum extrusion connected to one another using L-brackets and round head socket screws. Three aluminum extrusions were used for the top and side supports per screen with additional extrusions used to mount the 4th projector as shown in Figure 5. Each screen was made of acrylic with special coating to allow for stereoscopic capabilities. Four projects were incorporated in the design: InFocus IN5312a with 3D projection and side-by-side settings.

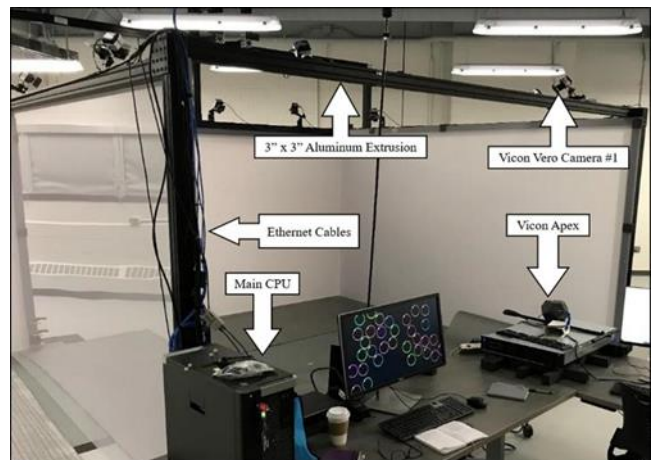


Figure 4. The 4-wall VR setup with optical tracking cameras, interaction device, and main workstation.

Nine optical tracking cameras were mounted to the top extrusion support bars along the length of the screens using six-degrees-freedom adjustable joints and mounting fixtures as shown in Figure 5. Using Ethernet cords and high-quality graphics card, all connections between the cameras were connected to an optical tracking camera lock sync box which was connected to the main CPU. Ethernet server adapter properties were altered to ensure maximum data reception from Optical tracking camera lock sync box which was connected to the main CPU. Ethernet server adapter properties were altered to ensure maximum data reception from Optical tracking cameras to Optical tracking Tracker software on main CPU as per guidelines from Optical tracking Quick Guide manual. Calibration of Optical tracking Vero® cameras was undertaken with the assistance of its iPad app and special reflector markers (same markers used in head tracker) to map out incremental clusters of volumes in the 4-wall environment.

Optimization of the location and orientation of all nine cameras along the top sides of the screens was conducted in SolidWorks as shown in Figure 5. In this Figure, each field of view (79.0 deg x 67.6 deg at a total length of 12 m) was modeled and attached to the front of each camera.

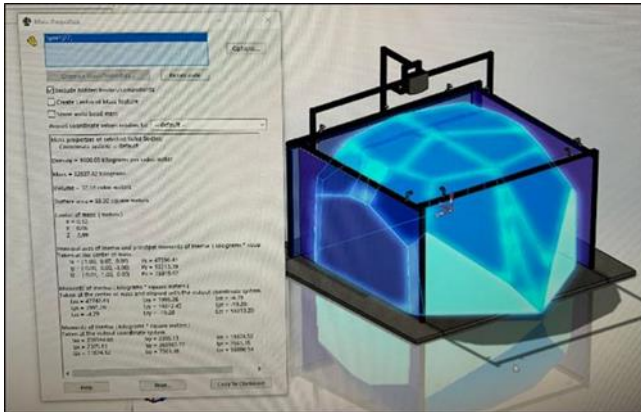


Figure 5. Optical tracking cameras' placement, orientation, optimization, and combined volume calculation.

After each camera was calibrated and coordinate system orientation was determined, "objects" were created within Tracker to identify 3D glasses movement (head tracking) in the VR enabler and ultimately Unity 3D. 3D printing and SolidWorks modeling tools were utilized in creating custom build marker holders mountable on 3D glasses as shown in Figure 6. Once "object was created, a simple text-file based virtual reality peripheral network (VRPN) was used to link the created object in Tracker to the VR enabler software. Using similar syntax, Middle VR allowed us to introduce 3D glasses as an object as was previously done for the Tracker Apex (a device that contains a joystick, buttons and operates as a wand in the VR scene). Once the configuration was complete, stereoscopic cameras setup in the VR-Enabler model were tied to a "tracker" in this instance the 3D glasses. This allows the user to move freely in the 4-Wall VR Environment which real-time tracking to occur in order continuously inform VR-Enabler where the location of the camera (the user's point of view) is in the 4-Wall VR Environment. Having head tracking capabilities transforms the 4-Wall VR Environment experience from forcing the user to stand

directly in the middle of the 4-Wall VR Environment to experience the full effect of the stereoscopic cameras to being able to freely move while tracking is happening and the users' head (and eyes) can control the virtual reality experience, giving the system integration continuous feedback for optimal experience.

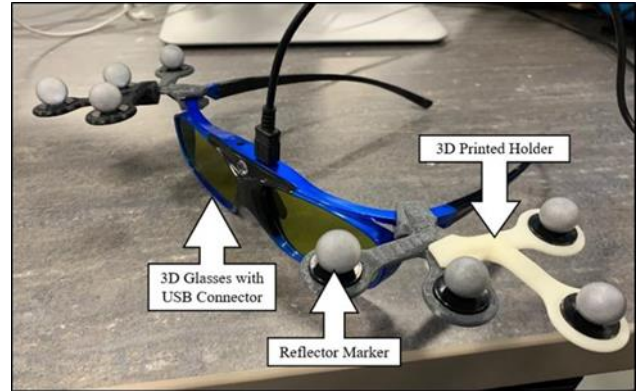


Figure 6. 3D VR glasses with reflectors for head tracking.

5. Results and Discussion

An immersive virtual reality tour in the 4-Wall VR Environment was conducted using Joystick navigation capabilities of the Optical tracking Apex device as shown in the Figure 7 below. Floating capabilities with the 4-WALL VR Environment apparatus were evident as shown in Figure 7.

In Figure 8, 3D glasses were placed directly in front of the camera lens to allow for the camera to capture stereoscopic effects of the projection.



Figure 7. The 4-WALL VR Environment VR simulation of dissection room with patient-specific hip-femur joint.

Anatomical features of the hip-femur joint including greater trochanter, lesser trochanter, intertrochanteric crest, femur head, femur neck, fovea capitis, and the acetabulum portions of the pubic bone, ischial bone, and iliac bone were identified using the VR-Enabler wand pointer. Decomposition of the joint was made possible by developing a VRAction script and collider to the hip and femur components in Unity 3D game engine software, while at the same time, using "Manipulation Return Objects" script was selected for those objects in order to return them in their original position after a set amount of time past disassembly.

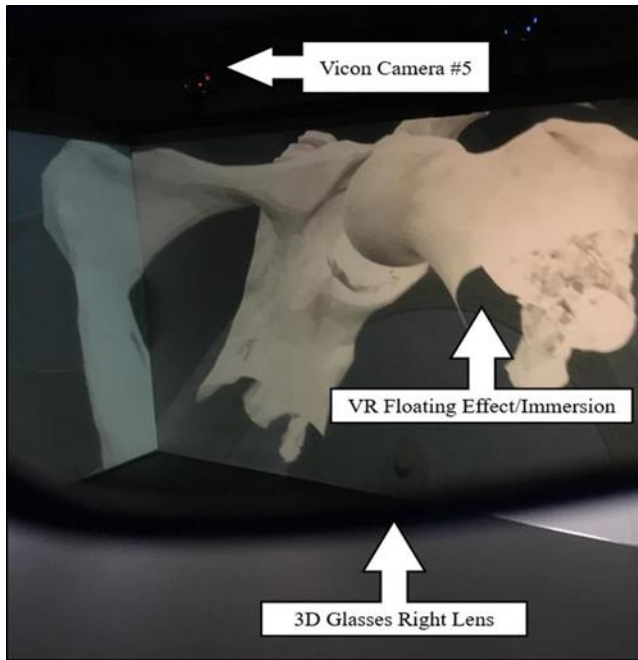


Figure 8. 3D glasses rendering of immersive experience in patient femur bone.

Due to added physics (Character joint) when the femur bone and the acetabulum in Unity 3D, the patient-specific model was dynamic, and the joint was exploded in flexion, extension, abduction, adduction and medial/lateral rotations. As the users immersed themselves in the model, a sense of depth and scaling for anatomical features within the joint was attained. This will aid physicians and researchers like orthopedic surgeons in gaining insight into patient specific volume measurements, distances, and orthopedic surgery specific data critical to tailor each medical intervention to the patient, as opposed to current medical approach which introduces a bit of error into each orthopedic replacement. For example, the Swedish Hip Arthroplasty Register in its Annual Report 2013, Garellick [14] reported that dislocation post total hip replacement (THR) contributed to 13.8% of primary revisions for patients and 22.5% of all second revisions in 2012. In addition, another study found that 22.5% of all THR revisions in the United States were because of instability and dislocation [15]. Being able to visualize hip-femur joints, its dynamics and take vital depth, scaling, and dimensional information in a patient-specific manner can contribute to efforts to lower the stated percentages and increase the efficiencies of said post-operation medical conditions in patients.

Orthopedics is one example of a medical specialty that can be greatly impacted by immersive virtual reality applications and tracking data acquisition.

6. Conclusion

This paper presents a novel patient-specific workflow to produce interactive, immersive and dynamic 3D anatomical models integrated into a 4-WALL VR environment (virtual reality system). This paper elaborates in extensive detail the steps taken to translate CT medical imaging data into accurate 3D model assemblies that are later incorporated into virtual reality

software where dynamics, lighting, and interactive capabilities are infused. Lastly, we detail in our workflow the intricacies of designing our 4-WALL VR environment, its components, and specific tools and 3D CAD solutions used to bring to life a hip-femur joint assembly. Finally, we discuss the benefits of this state-of-the-art technology, its future, and how it can be applied to various medical fields in need of visualization and computer modeling capabilities to improve their diagnoses, medical procedures like surgery, and extracting more information from medical imaging data.

Acknowledgement

The authors would like to thank Eastern Michigan University Virtual Reality Laboratory for supporting this endeavor and the GameAbove College of Engineering and Technology for facilitating this research work.

Author contributions

Hesham Tanbour: CT data analysis and transformation, writing-original draft preparation, software, visualization, anatomical insight, tracking system calibration, and validation. **Emad Tanbour:** VR technology environment design and erection, integration, VR hardware design and build, methodology, CAD software, editing and preparing final manuscript, and research project management.

Conflicts of interest

The authors declare no conflicts of interest.

References

1. Tcha-Tokey, K., Loup-Escande, E., Christmann, O., & Richir, S. (2017). Effects on User Experience in an Edutainment Virtual Environment. Proceedings of the European Conference on Cognitive Ergonomics 2017, 1–8. <https://doi.org/10.1145/3121283.3121284>
2. Nan, X., Zhang, Z., Zhang, N., Guo, F., He, Y., & Guan, L. (2013). VDESIGN: Toward image segmentation and composition in cave using finger interactions. 2013 IEEE China Summit and International Conference on Signal and Information Processing, 461–465. <https://doi.org/10.1109/ChinaSIP.2013.6625382>
3. Sigitov, A., Scherfgen, D., Hinkenjann, A., & Staadt, O. (2015). Adopting a Game Engine for Large, High-Resolution Displays. *Procedia Computer Science*, 75, 257–266. <https://doi.org/10.1016/j.procs.2015.12.246>
4. Long, G., Kim, H. S., Marsden, A., Bazilevs, Y., & Schulze, J. P. (2012). Immersive volume rendering of blood vessels (I. E. McDowall & M. Dolinsky, Eds.; p. 82890L). <https://doi.org/10.1117/12.909729>
5. Witkowski, M., Lenar, J., Sitnik, R., & Verdonshot, N. (2012). A virtual reality interface for pre-planning of surgical operations based on a customized model of the patient (I. E. McDowall & M. Dolinsky, Eds.; p. 82890M). <https://doi.org/10.1117/12.909857>
6. Al-khalifah, A. H., Woff, R., Alexandrov, V. N., & Roberts, D. J. (2005). Case study: interacting with

- volumetric medical datasets in networked CAVE environments (R. F. Erbacher, J. C. Roberts, M. T. Grohn, & K. Borner, Eds.; p. 350). <https://doi.org/10.1117/12.587633>
7. Toward Precision Medicine. (2011). National Academies Press. <https://doi.org/10.17226/13284>
 8. Arnold, J. L., McKenzie, F. (Rick) D., Miller, J. L., & Mancini, M. E. (2018). The Many Faces of Patient-Centered Simulation. *Simulation in Healthcare: The Journal of the Society for Simulation in Healthcare*, 13(3S), S51–S55. <https://doi.org/10.1097/SIH.0000000000000312>
 9. simlab-soft.com. (n.d.). https://www.simlab-soft.com/3dplugins/SolidWorks/fbx_exporter_for_SolidWorks-main.aspx?h=1. Retrieved February 8, 2022, from https://www.simlab-soft.com/3dplugins/SolidWorks/fbx_exporter_for_SolidWorks-main.aspx?h=1
 10. He, Y., Zhang, Z., Nan, X., Zhang, N., Guo, F., Rosales, E., & Guan, L. (2017). vConnect: perceive and interact with real world from CAVE. *Multimedia Tools and Applications*, 76(1), 1479–1508. <https://doi.org/10.1007/s11042-015-3121-4>
 11. Koning, A. H. J. (2011). How 3D immersive visualization is changing medical diagnostics (B. E. Rogowitz & T. N. Pappas, Eds.; p.786503). <https://doi.org/10.1117/12.881511>
 12. Lin, Q., Xu, Z., Li, B., Baucom, R., Poulouse, B., Landman, B. A., & Bodenheimer, R. E. (2013). Immersive virtual reality for visualization of abdominal CT (C. K. Abbey & C. R. Mello-Thoms, Eds.; p. 867317). <https://doi.org/10.1117/12.2008050>
 13. Ritter, K. A., Borst, C. W., & Chambers, T. L. (2015). Overview and Assessment of Unity Toolkits for Rapid Development of an Educational VR Application. *International Journal for Innovation Education and Research*, 3(7), 147–164. <https://doi.org/10.31686/ijer.vol3.iss7.398>
 14. Garellick G, K. J. L. H. (2013). Swedish Hip Arthroplasty Register Annual Report 2013.
 15. Bozic, K. J., Kurtz, S. M., Lau, E., Ong, K., Vail, T. P., & Berry, D. J. (2009). The Epidemiology of Revision Total Hip Arthroplasty in the United States. *The Journal of Arthroplasty*, 24(2), e19. <https://doi.org/10.1016/j.arth.2008.11.033>



© Author(s) 2023. This work is distributed under <https://creativecommons.org/licenses/by-sa/4.0/>



Sentiment analysis with ensemble and machine learning methods in multi-domain datasets

Muhammet Sinan Başarslan^{*1}, Fatih Kayaalp²

¹Istanbul Medeniyet University, Department of Computer Engineering, Türkiye

²Duzce University, Department of Computer Engineering, Türkiye

Keywords

Ensemble Learning
Machine Learning
Sentiment Analysis
Text Representation

Research Article

DOI: 10.31127/tuje.1079698

Received: 26.02.2022

Accepted: 07.04.2022

Published: 26.04.2022

Abstract

The first place to get ideas on all the activities considered to occur in everyday life was the comments on the websites. This is an area that deals with these interpretations in the natural language processing, which is a sub-branch of artificial intelligence. Sentiment analysis studies, which is a task of natural language processing are carried out to give people an idea and even guide them with such comments. In this study, sentiment analysis was implemented on public user feedback on websites in two different areas. TripAdvisor dataset includes positive or negative user comments about hotels. And Rotten Tomatoes dataset includes positive (fresh) or negative (rotten) user comments about films. Sentiments analysis on datasets have been carried out by using Word2Vec word embedding model, which learns the vector representations of each word containing the positive or negative meaning of the sentences, and the Term Frequency Inverse Document Frequency text representation model with four machine learning methods (Naïve Bayes-NB, Support Vector Machines-SVM, Logistic Regression-LR, K-Nearest Neighbour-kNN) and two ensemble learning methods (Stacking, Majority Voting-MV). Accuracy and F-measure is used as a performance metric experiments. According to the results, Ensemble learning methods have shown better results than single machine learning algorithms. Among the overall approaches, MV outperformed Stacking.

1. Introduction

Software and hardware technologies are in constant evolution. As a result of this development, people's habits also change. Communication devices have been improved over time. Especially with the improvement of intelligent devices, the first place to be referred to, in many areas, especially in the health field, is the apps and websites on these devices.

The opinions of the people who post comments on these two websites can be seen from every device that has access to the internet and these opinions give an idea to the users. Naturally, before going to a movie or deciding on a hotel to stay at, it is important for people to visit these sites and see the experiences and comments of other people.

Positive (fresh) or negative (rotten) comments on a movie on the Rotten tomatoes site can be a guide for those who would watch a movie for the first time. Apart

from the comments on the movie, information on the director, actor reviews, and cinema news are also included and it functions as a guide for the site users. Similarly, users who look for hotel and restaurant reviews on the TripAdvisor site before planning a trip can make their decisions on the hotels or restaurants they would prefer to visit in their trips, and even cancel their travels. It was seen that the comments on these websites pushed the communication to a process that guides people with the infrastructure of internet technologies. Companies that want to benefit from this process have supported the studies that extract sentiments from the comments using natural language processing techniques and this extracting process is a sub-branch of artificial intelligence. This process is not limited to the selection of movies or hotels and has turned into an area where people can get ideas and benefit from many features.

* Corresponding Author

^{*}(msinanbasarslan@gmail.com) ORCID ID 0000-0002-7996-9169
(fatihkayaalp@duzce.edu.tr) ORCID ID 0000-0002-8752-3335

Cite this article

Başarslan, M. S., & Kayaalp, F. (2023). Sentiment analysis with ensemble and machine learning methods in multi-domain datasets. Turkish Journal of Engineering, 7(2), 141-148

In this study, a sentiment analysis study was carried out on the comments that were collected from two websites accessible to everyone and that were labeled with a sentiment class. After feature extraction with the help of a Word2Vec (W2V) model that learns the vector representations of the words in the comments and the Term frequency Inverse document frequency (TF-IDF) model based on text frequency, sentiment analysis was performed by creating comprehensive models with machine learning and collective learning methods. In comparing the performances of the models created for sentiment analysis, the training and test cluster distinctions were made in two ways as the holdout method, training-test sets, 80% -20%, and 70%-30%, respectively. Before creating classifier models for sentiment analysis, text pre-processing processes such as clearing numbers of comments, removing numbers and special characters, converting all letters to the lowercase, and stemming processes were carried out.

Our contribution to the literature covered in the present study;

The effect of text representation methods by frequency (TF-IDF) and by the prediction (W2V) on performance has been studied.

Creating a high-performance model in the analysis of sentiments, the impact of general learning methods and single machine learning methods for performance has been studied.

With the heterogeneous use of single machine learning methods in ensemble learning methods, the effect of the model on performance has been analyzed. The workflow process followed during the study can be seen in Figure 1.

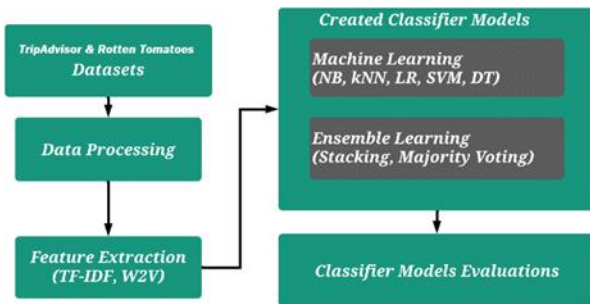


Figure 1. The flowchart of the study

As can be seen in Figure 1, after the data labeled with sentiment class were passed through the pre-processing process, separate text representation was created with both word frequency-based TF-IDF and predicted-based W2V methods. Then, models for machine learning, ensemble learning, and sentiment classes were created and the results of these models were obtained.

In this study, previous studies or similar studies with the sentiment analysis study on the hotel reviews on the TripAdvisor website and the criticisms of the movies, actors, and directors on the Rotten Tomatoes website are explained in the second section.

Information on the algorithms used in classifier models, ensemble learning algorithms, text representation methods, and the datasets used are presented in the third section. Performance metrics and

the experimental results are presented in section four. Evaluations of the results and future works are presented in section five.

2. Related works

Reviews on websites such as TripAdvisor and Rotten Tomatoes are a big part of the sentiment analysis study. The ability to access these sites from any device and the comments made for movies or hotels give people an introductory idea about their preferences.

Sentiment analysis, which is the subject of classifying people’s sentiments using natural language processing, and which is also a sub-branch of artificial intelligence, is examined in a multi-disciplinary fashion. In this section, machine learning models and interpretation, classification models will be analyzed. The authors collected reviews from the TripAdvisor site on five hotels in Aswan, Egypt, which received a total of 11.458 reviews. They used TF-IDF for text representation of these comments. NB yielded the highest accuracy Score among the models they created with SVM, NB, and Decision Tree (DT) classifiers for sentiment analysis [1].

The authors used a TripAdvisor dataset that It consists of approximately 250000 customer-provided reviews of 1850 hotels. They suggested feature extraction of these studies and Subjectivity Based Feature Extraction. They created a model through SVM, NB, and DT, and the SVM yielded the best result of 87.51% with the help of the method they suggested [2].

They collected a total of 2000 reviews from the TripAdvisor website, 500 positive and 500 negative reviews for training sets and 500 positives and 500 negative reviews for test sets. They created a model with SVM, NB, and DT. Through the machine learning method, they achieved an accuracy score of 87 % in hotel assessment classification with the help of SVM [3].

In sentiment analysis performed on the Rotten Tomatoes Analysis Dataset, the n-gram method (Bigram, Unigram, Trigram) and the combination of various n-grams were used for text representations. In the study, models were created in SVM, Maximum Entropy, and NB. The study notes that it yields better results for unigram, bigram, and trigram methods, but the score decreases when observed for four grams, five grams, six grams, and more [4].

Of the one hundred thousand views about the hotel, 70% is seperated into training sets, 10% is validation sets, and 20% is divided into test sets. GloVe built models with Bi-Directional Long Short-Term Memory (Bi-LSTM) and various Convolutional Neural Networks for emotion classification after text representations with FastText. The Bi-LSTM model with GloVe word embedding technique achieved the best performance with 73.73% test accuracy [5].

They used a movie dataset on Rotten Tomatoes consisting of 8000 polar movie reviews. They created models with RF, kNN, NB, and Bagging classifiers. In their study, the RF technique achieved the highest accuracy score of 95% [6].

Rotten Tomatoes Film Dataset created various methods such as NB, Instance-Based Learning, DT, SVM

in the classification study on comments. The kNN algorithm performed between 65% and 95% on average [7].

Using W2V technique and Machine Learning techniques, a Sentiment Analysis Model has been proposed to analyze the emotions of Egyptian students in the learning process with the pandemic. The word embedding process was then evaluated by NB, SVM and DT classification, and evaluated for precision, recall and accuracy [8].

During the COVID-19 pandemic from Twitter in 2020, English tweets were classified as positive or negative by applying the LR algorithm to them, using this method they achieved a classification accuracy of 78.5% [9].

In the study, MultinomialNB on Twitter datasets, Results were obtained with BernoulliNB, LR, Stochastic Gradient Descent (SGD). In the experimental results, BernoulliNB, LR and SGD classifier reached up to 75% accuracy [10].

In this study, three different ensemble Machine Learning models are proposed to classify the data of approximately 12 thousand tweets in the UK into three emotion tags. First, the stacking classifier gave the highest F1 score of 83.5%, while in the second model the voting classifier gave 83.3% and in the last model the bagging classifier gave 83.2% results [11].

As seen in these studies, experiments were carried out on text representations or classifying models for performance improvement in the models created in sentiment analysis studies. Similarly, in this study, models based on ensemble learning in which traditional and predictive text representation methods are used together with different classification models, are created and their effect on the classification is analyzed.

3. Methodology

In this section, text representations, machine and ensemble learning algorithms, and datasets will be discussed.

3.1. Datasets

In the study, comments from public hotel review sites, which are shared as open-source by those who collected from these sites, were used.

TripAdvisor hotel reviews dataset [12] consists of data from 20490 hotel reviews. Reviews with 1,2 stars are marked as negative, 3 stars as neutral, and 4,5 stars as positive. The dataset consists of two attributes, hotel reviews and ratings.

Rotten Tomatoes films and critic reviews dataset has movie reviews, labeled as 240000 fresh, and 240000 rotten [13]. Reviews of Gervais with 1,2 stars were marked as negative, ones with 3 stars as neutral and ones with 4,5 stars as positive. The dataset consists of two attributes, film reviews and rating.

Hotel and Movie datasets were preprocessed before classification, including removing punctuation and symbols, conversion of characters to lower case and stemming. Also, stop words have been removed. The python NLTK library is used for these operations.

3.2. Text representation

Methods used to represent the text in documents pave the way for successful results in classification. Text representation methods are divided into two methods as Frequency Based Representation and Prediction Based Representation. Frequency-based text representation, which is defined as the more traditional method, is based on the principle of identifying the words in documents and the frequency of these words. The following text representation methods, W2V and TF-IDF, were used in this study.

3.2.1. TF-IDF

TF-IDF is the weight factor calculated by the statistical method that shows the importance of a term in a document.

TF is the method used to calculate the weight of a term in a document. There are weight calculation methods such as binary, raw frequency, and logarithm normalization.

IDF attempts to figure out whether a word is a term and not a Stop Word by detecting the number of occurrences of the word in more than one document. It is calculated by dividing the Number of Documents Elapsed by the Period by the absolute value of the logarithm of the Number of Documents.

3.2.2. Word2Vec

Word2Vec is an unsupervised and prediction-based model that attempts to express words in vector space. It was invented in 2013 by Google researcher Tomas Mikolov and his team. There are 2 types of sub-methods: Continuous Bag of Words (CBOW) and Skip-Gram [12].

CBOW and Skip-Gram models differ from each other in receiving input and output data. In the CBOW model, words that are not in the center of the window size are taken as input and the words in the center are predicted to be output; In the Skip-Gram model, the words in the center are taken as input and the words that are not in the center are predicted to be output.

This process continues until the whole sentence is processed. This operation is applied to all of the sentences and the mapping operation is applied to the unlabeled data available at the beginning and it is then ready to be trained.

In the study, hyperparameter settings for vector size of 100 and 200, the window size of 5, the Sub-sampling Rate of 1e-3, Min-count of 5 were taken from the Word2Vec method. CBOW from W2V methods was used.

3.3. Machine learning

Machine learning is a sub-branch of computer science that was developed from studies of numerical learning and the recognition of models in artificial intelligence in 1959. Machine learning is a system that investigates the work of algorithms that can make predictions on data. The classifier algorithms Logistic LR, SVM, NB, and kNN were used in the study. It is seen in Figure 2. These Four algorithms are discussed in this section.

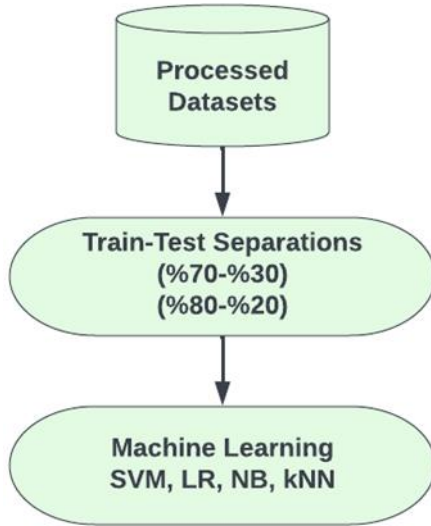


Figure 2. The flowchart of the Machine learning process

3.3.1. Naïve bayes

It is a lazy learning algorithm based on Bayes' theorem. It calculates all probabilities for each element in the data set and performs the classification based on the higher results [15].

3.3.2. Support vector machine

SVM is a supervised learning algorithm based on statistical learning theory. It is used to distinguish between two classes of data in the most appropriate way. The data set is divided into two, based on linear separation and non-separation [16].

3.3.3. K-Nearest neighbor

kNN is one of the easy-to-implement supervised learning algorithms. Although it is used to solve both classification and regression problems, it is mostly used in the solution of classification problems in the industry.

kNN algorithms were proposed by [17]. The algorithm is utilized by means of making use of data from a sample set whose classes are known. The distance of the new data to be included in the sample data set is calculated based on the existing data and the k number of close neighbors is checked. Generally, 3 types of distance functions are used for the calculation of distance [18]:

- "Euclidean" Distance
- Distance to "Manhattan"
- "Minkowski" is the Distance.

3.3.4. Logistic regression

It is a statistical method used to analyze a data set with one or more independent variables that determine the result. The result is measured by a binary variable [19].

3.4. Ensemble learning

Ensemble Learning is the combined use of machine algorithms of the same types (homogeneous Ensemble Learning) or different types (heterogeneous Ensemble Learning). It is based on the use of various models together to improve the performance achieved by a single algorithm [20].

Homogeneous or heterogeneous machine learning models have a variety of Ensemble Learning methods such as Bagging, Boosting, and Stacking, depending on the decision function (average, voting, etc.). In addition to these, two important variations have been developed one of these is the Voting, which complements Bagging, and the Blending, a subtype of Stacking. Although Voting is a subtype of Bagging and Blending is a subtype of Stacking, these techniques are frequently referred to as types of Ensemble Learning. It is seen in Figure 3.

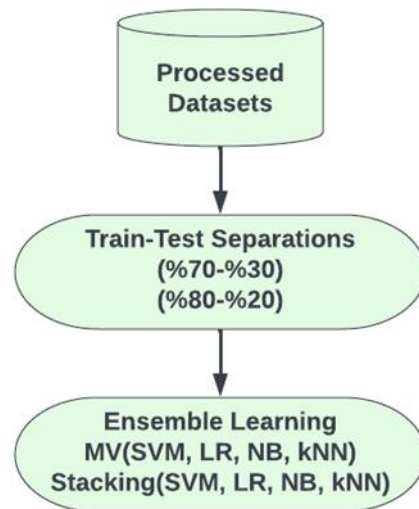


Figure 3. The flowchart of the Ensemble learning process

3.4.1. Voting

It is an effective and a simple ensemble algorithm used in classification processes. Minimum two sub-models are created and each sub-model determines the results of the model by combining the predictions through a vote that determines the prediction result by taking the average of the predictions [21]. In this study, majority voting was used.

3.4.1.1. Majority voting

In majority voting, every individual classifier vote for a class, and the majority wins. In statistical terms, the predicted target label of the ensemble is the mode of the distribution of individually predicted labels.

Here, we predict the class label \hat{y} via majority (plurality) voting of each classifier C. This equation (1) is given.

$$\hat{y} = \text{mode}\{C_1(x), C_2(x), \dots, C_m(x)\} \quad (1)$$

Assuming that we combine three classifiers that classify a training sample as in the following equation (2):

$$\hat{y} = mode\{0,0,1\} = 0 \tag{2}$$

Via majority vote, we would classify the sample as "class 0." [22].

3.4.2. Stacking

Stacking is an extension of the Voting method used in classification processes. More than one sub-model may be chosen. It also allows the use of a different model for the best combination of predictions [23].

4. Experiments and results

In the experimental analysis, the two data sets were divided by using a test training separation method called holdout (80% -20% and 70% -30%). Python scikit-learn library was used in the experiments.

In the experimental analysis, NB, SVM, LR, and kNN classifiers were used. Stacking and Voting methods were used in ensemble classification. Experimental evaluations were carried out on a computer having a 4.1 GHz AMD RYZEN 7 2700 CPU with 32.00 GB RAM.

4.1. Performance metrics

The performance metric used to evaluate the predictive performance of sentiment classification models is the accuracy and F-measure. Accuracy is one of the most commonly used metrics. It is the ratio of true negatives (TN) and true positives (TP) to the total number of samples as given by Equation (3) [24].

$$ACC = \frac{T_p + T_N}{T_p + T_N + F_p + F_N} \tag{3}$$

Abbreviations in Equation 1 show the number of TN, the number of TP, the number of false positives (FP), and the number of false negatives (FN).

The F-measure value is shown in Equation (4) [24].

$$F - measure (F) = \frac{2 * Precision * Sensitivity}{Precision + Sensitivity} \tag{4}$$

4.2. Experimental results

TF-IDF and W2V text representations in TripAdvisor and Rotten Tomatoes data sets, followed by 80-20% and 70-30% train-test separation, NB, kNN, LR, SVM machine learning methods, and Stacking and Voting ensemble learning methods using these methods together with sentiment classification models were created using Table 1, Table 2 show the accuracy results of the models obtained with TripAdvisor, Table 3 and Table 4 Rotten Tomatoes. Table 5 and Table 6 show TripAdvisor's F-measure result and Table 7 and Table 8 show the F-measure result for Rotten Tomatoes.

Table 1. Accuracy results of methods on TripAdvisor Dataset (80:20 training and test sets)

	NB	kNN	LR	SVM	Stacking	Voting
TF-IDF	83.1	80.2	82.8	83.3	83.6	84.2
W2V	83.5	81.6	83.4	83.6	84.1	84.7

When the Table 1 is analyzed, it is seen that SVM has the best results in an accuracy score among the single machine learning methods. When the ensemble learning methods are compared against single machine learning methods, it is seen that both ensemble learning methods have demonstrated better performance than single machine learning methods. Furthermore, Voting has demonstrated better results than stacking among ensemble learning methods.

Table 2. Accuracy results of methods on TripAdvisor Dataset (70:30 training and test sets)

	NB	kNN	LR	SVM	Stacking	Voting
TF-IDF	83.3	82.1	84.1	85	85.8	86.2
W2V	85.5	80.1	85.8	86.9	86.5	87.3

When the Table 2 is analyzed, it is seen that SVM has the best results in an accuracy score among the single machine learning methods with TF-IDF. However, the LR achieves the best Results with W2V. When the ensemble learning methods are compared against single machine learning methods, it is seen that Stacking is slightly behind LR and Voting is ahead of LR. Furthermore, Voting has demonstrated better results than Stacking among ensemble learning methods.

Table 3 and Table 4 show, the results obtained from sentiment classification models created using NB, kNN, LR, SVM, and all machine learning methods together in Stacking and Voting ensemble learning following TF-IDF and W2V text representations with 80%-20% and 70%-30% training/test sets on the Rotten Tomatoes dataset.

Table 3. Accuracy results of methods on Rotten Tomatoes Dataset (80:20 training and test sets)

	NB	kNN	LR	SVM	Stacking	Voting
TF-IDF	80.5	74.3	80.7	82.2	83.8	84.5
W2V	81.3	80.1	81.6	82.7	85.8	86.5

When the Table 3 is analyzed, it is seen that SVM has the best results in an accuracy score among the single machine learning methods with TF-IDF. However, SVM achieves the best Results with W2V. When the ensemble learning methods are compared against single machine Learning methods, it is seen that Stacking is behind SVM but Voting is ahead of SVM. Furthermore, Voting has demonstrated better results than stacking among ensemble learning methods.

Table 4. Accuracy results of methods on Rotten Tomatoes Dataset (70:30 training and test sets)

	NB	kNN	LR	SVM	Stacking	Voting
TF-IDF	81.5	76.8	81.7	83.8	83.9	87.2
W2V	81.6	80.6	81.9	87.8	88.5	88.7

When the Table 4 is analyzed, it is seen that SVM has the best results in an accuracy score among the single machine learning methods with TF-IDF. When the ensemble learning methods are compared against single machine learning methods, it is seen that both ensemble learning methods have demonstrated better performance than single machine learning methods. Furthermore, Voting has demonstrated better results than stacking among ensemble learning methods.

Table 5. F-measure results of methods on TripAdvisor Dataset (80:20 training and test sets)

	NB	kNN	LR	SVM	Stacking	Voting
TF-IDF	78.9	74.1	76.3	78.4	79.2	79.5
W2V	79.2	75.3	77.2	78	79.6	80.1

As can be seen in Table 5, Ensemble models gave better results. Although the results with the Community models were close to each other, Voting gave better results.

Table 6. F-measure results of methods on TripAdvisor Dataset (70:30 training and test sets)

	NB	kNN	LR	SVM	Stacking	Voting
TF-IDF	77.4	72.1	76.2	76.7	78.3	78.6
W2V	78.6	73.4	77.1	78.5	78.4	79.4

As seen in Table 6, Ensemble models gave better results than other machine learning models. Community models gave better results than Voting Stacking in itself.

Table 7. F-measure results of methods on Rotten Tomatoes Dataset (80:20 training and test sets)

	NB	kNN	LR	SVM	Stacking	Voting
TF-IDF	82.4	81.3	84.5	85.7	87.3	87.5
W2V	83.6	82.5	85.3	86.3	87.4	87.8

As seen in Table 7, the Voting Ensemble model gave the best results. It was seen that the models created after W2V gave better results than the models created with TF-IDF.

Table 8. F-measure results of methods on Rotten Tomatoes Dataset (70:30 training and test sets)

	NB	kNN	LR	SVM	Stacking	Voting
TF-IDF	82.5	81.2	83.2	84.6	85.3	85.6
W2V	83.4	80.1	84.2	85.4	86.2	86.5

As seen in Table 8, Ensemble models gave better results. Ensemble models gave better results than Voting Stacking in itself.

4.3. Literature comparison

The results, in which we compared the method with which we obtained the best results in the sentiment analysis study on the TripAdvisor dataset, and the other studies, are given in Table 9.

Table 9. Accuracy results comparison of models on Tridadvisor dataset

References	Method	ACC	F measure
25	TF-IDF	0.82	-
26	BOW	0.82	-
Our Voting Model	TF-IDF	86.2	79.5
	W2V	87.3	80.1

No study has been found in the literature on the open source Gervious's Rotten Tomatoes dataset [13]. The dataset was compared with other studies with a common source. These comparison results are given in Table 10.

Table 10. Accuracy results comparison of models on Rotten Tomatoes dataset

References	Method	ACC	F measure
27	n-gram	-	80.7
Our Voting Model	TF-IDF	87.2	87.5
	W2V	88.7	87.8

As can be seen in Table 9 and Table 10, even if the word representation methods are common, using machine learning algorithms together with ensemble models instead of using them alone increases the classification performance.

5. Discussion and conclusion

Sentiment classification study was carried out following the performance of text representation (TF-IDF) and word embedding methods (W2V) after text processing on public data sets of TripAdvisor and Rotten Tomatoes. Using the machine learning methods analyzed in this study together with ensemble learning algorithms instead of using them alone is the main contribution of the paper to the sentiment classification process. In this context, a sentiment classification study was carried out with the help of four different machine learning algorithms, namely NB, kNN, SVM, and LR, and two ensemble learning algorithms, namely Stacking and Voting. Training/test sets are used in the separation of 80%- 20% and 70%- 30% on both datasets in the holdout method. The experimental results were evaluated by measuring the accuracy and F-measure performance metric.

Instead of using single machine learning classifiers, using them together in ensemble learning methods has demonstrated better results. Voting, which is one of the ensemble methods, has been observed to yield better results in all experiments compared to Stacking.

When TF-IDF and W2V results of the experiments are evaluated, it is seen that W2V has outperformed TF-IDF. At 70%-30% and 80%-20% test-train separation, W2V gave better results than the TF-IDF.

Based on the experiments carried out as part of this study, it has been observed that more successful results are obtained in the models that are created using single classification algorithms together for ensemble learning. The performances of ensemble learning algorithms for larger data sets from different domains are aimed to be analyzed in future works.

We are planning to examine the performances of Bert in particular, FastText, Glove, Bert (even RoBerta, DistilBert etc., which are derivatives of Bert), together with single and ensemble ML methods, in future studies.

Author contributions

Fatih Kayaalp: Defining the methodology, evaluations of the results and draft editing **Muhammet Sinan Başarslan:** Preprocessing the dataset, data analysis, experiments and evaluations, manuscript draft preparation

Conflicts of interest

The authors declare no conflicts of interest.

References

1. Mostafa, L. (2020). Machine learning-based sentiment analysis for analyzing the travelers reviews on Egyptian hotels. In Joint European-US Workshop on Applications of Invariance in Computer Vision. Springer, Cham, 405-413.
2. Dehkharghani, R., Yanikoglu, B., Tapucu, D., & Saygin, Y. (2012). Adaptation and Use of Subjectivity Lexicons for Domain Dependent Sentiment Classification. IEEE 12th International Conference on Data Mining Workshops, 10 December, Washington, 669-673.
3. Raut, V. B., & Londhe, D. D. (2014). Opinion Mining and Summarization of Hotel Reviews. International Conference on Computational Intelligence and Communication Networks, November, Bhopal, 556-559.
4. Tiwari, P., Mishra, B. K., Kumar, S., & Kumar, V. (2017). Implementation of n-gram methodology for rotten tomatoes review dataset sentiment analysis. International Journal of Knowledge Discovery in Bioinformatics (IJKDB), 7(1),30-41.
5. Zhou, Y. (2019). Sentiment Classification with Deep Neural Networks. Master's Thesis. Tampere University. Finland.
6. Sahu, T. P., & Ahuja, S. (2016). Sentiment analysis of movie reviews: A study on feature selection and classification algorithms. International Conference on Microelectronics, Computing, and Communications (MicroCom), 23-25 January, Durgapur, 1-6.
7. Oswin, H. R., Virginia, G., & Antonius, R. C. (2016). Sentiment Classification of Film Reviews Using IB1. 7th International Conference on Intelligent Systems, Modelling, and Simulation (ISMS), 23-25 January, Bangkok 78-82.
8. Mostafa, L. (2021). Egyptian Student Sentiment Analysis Using Word2vec During the Coronavirus (Covid-19) Pandemic. In: Hassanien A.E., Slowik A., Snášel V., El-Deeb H., Tolba F.M. (eds) Proceedings of the International Conference on Advanced Intelligent Systems and Informatics 2020. AISI 2020. Advances in Intelligent Systems and Computing, vol 1261. Springer, Cham.
9. Machuca, C. R., Gallardo, C., & Toasa, R. M. (2021, February). Twitter sentiment analysis on coronavirus: Machine learning approach. In Journal of Physics: Conference Series (Vol. 1828, No. 1, p. 012104). IOP Publishing.
10. U. A. Siddiqua, T. Ahsan, & A. N. Chy, (2016). Combining a rule-based classifier with ensemble of feature sets and machine learning techniques for sentiment analysis on microblog. in 2016 19th International Conference on Computer and Information Technology (ICCIT), 2016, 304- 309.
11. Rahman, M., & Islam, M. N. (2022). Exploring the performance of ensemble machine learning classifiers for sentiment analysis of covid-19 tweets. In Sentimental Analysis and Deep Learning (pp. 383-396). Springer, Singapore.
12. Alam, M. H., Ryu, W. J., & Lee, S. (2016). Joint multi-grain topic sentiment: modeling semantic aspects for online reviews. Information Sciences, 339, 206-223.
13. Gervais, N. (2019). Rotten Tomatoes Dataset. rotten-tomatoes-dataset (Access Date:21.02.2020).
14. Mikolov, T., Sutskever, I., Chen, K., Corrado, G., & Dean, J. (2013). Distributed Representations of Words and Phrases and their Compositionality, Advances in Neural Information Processing systems 3111-3119.
15. Basarslan, M. S., & Kayaalp, F. (2020). Sentiment analysis with machine learning methods on social media. ADCAIJ: Advances in Distributed Computing and Artificial Intelligence Journal, 9(3),5-15.
16. Bakay, M. S., & Ağbulut, Ü. (2021). Electricity production-based forecasting of greenhouse gas emissions in Turkey with deep learning, support vector machine and artificial neural network algorithms. Journal of Cleaner Production, 285, 125324.
17. Cover, T., & Hart, P. (1967). Nearest neighbor pattern classification. IEEE Transactions on Information Theory, 13(1),21-27.
18. Basarslan, M. S., Bakir, H., & Yücedağ, İ. (2019, April). Fuzzy logic and correlation-based hybrid classification on hepatitis disease data set. In The International Conference on Artificial Intelligence and Applied Mathematics in Engineering (pp. 787-800). Springer, Cham.
19. Indulkar, Y., & Patil, A. (2021). Comparative Study of Machine Learning Algorithms for Twitter Sentiment Analysis. 2021 International Conference on Emerging Smart Computing and Informatics (ESCI), 295-299.
20. Zhou, Z. H. (2012). Ensemble methods: foundations and algorithms. CRC press.
21. Polikar, R. (2006). Ensemble based systems in decision making. IEEE Circuits and systems magazine, 6(3), 21-45.
22. Tao, F., Jiang, L., & Li, C. (2021). Differential evolution-based weighted soft majority voting for crowdsourcing. Engineering Applications of Artificial Intelligence, 106, 104474.
23. Battiti, R., & Colla, A. M. (1994). Democracy in neural nets: Voting schemes for classification. Neural Networks, 7(4), 691-707.
24. Canli, H., & Toklu, S. (2021). Deep Learning-Based Mobile Application Design for Smart Parking. IEEE Access, 9, 61171-61183.

25. Mahima, K. T. Y., Ginige, T. N. D. S., & De Zoysa, K. (2021). Evaluation of Sentiment Analysis based on AutoML and Traditional Approaches. *Evaluation*, 12(2).
26. Assyafah, H. B., Yulianti, D. T., & Kom, S. (2021). Analisis Dataset menggunakan Sentiment Analysis (Studi Kasus Pada Tripadvisor). *Jurnal STRATEGI-Jurnal Maranatha*, 3(2), 320-331.
27. Frangidis, P., Georgiou, K., Papadopoulos, S. (2020). Sentiment Analysis on Movie Scripts and Reviews. In: Maglogiannis, I., Iliadis, L., Pimenidis, E. (eds) *Artificial Intelligence Applications and Innovations. AIAI 2020. IFIP Advances in Information and Communication Technology*, vol 583. Springer, Cham. https://doi.org/10.1007/978-3-030-49161-1_36



© Author(s) 2023. This work is distributed under <https://creativecommons.org/licenses/by-sa/4.0/>



Determination of the critical drop height and critical flow velocity of aluminum alloy (AL-91% Mg-8% Fe-0.4% Zn-0.2%) in gravity sand casting

Francis Inegbedion ^{*1}, James Chinedu Orji ¹

¹University of Benin, Department of Production Engineering, Nigeria

Keywords

Critical drop height
Critical velocity
Gravity sand casting
Finite element method
Sprue

Research Article

DOI: 10.31127/tuje.1077467

Received: 22.02.2022

Accepted: 20.04.2022

Published: 26.04.2022

Abstract

Casting is a manufacturing process in which molten metal is poured through the gating system to fill the mould cavity where it solidifies. Variations in casting parameters by different researchers have led to significant variations in casting guidelines, which have forced Foundry Engineers to carry out a number of trial-and-error runs to create guidelines based on their own experience. These variations in guidelines have led to defects occurring in casting during the mould filling process. This work aimed at determining the critical drop height and critical flow velocity of a certain molten aluminum alloy as it flow down the mould sprue in gravity sand casting. The continuity equation was used to describe the velocity distribution of the aluminum alloy as it flows down the sprue. The mathematical tool used in this research is the finite element method. It involves the discretization of the domain of interest into smaller finite elements. The weak form of the governing equation was obtained and integrated over the domain of interest. The results obtained, established the critical flow velocity of aluminum alloy, down the sprue, as 2.565×10^3 mm/s and the critical drop height as 377mm. Results obtained were compared with literature and were also used to produce various casts, it was observed that casts produced, using sprue height below the critical drop height obtained prevented casting defects, while at sprue height above the critical drop height, the danger of casting defects could not be avoided.

1. Introduction

Casting is a manufacturing process in which liquid metal is usually poured into a mould cavity of the desired shape, and then allowed to solidify. The solidified part is known as casting, which is ejected or broken out of the mould to complete the process. There are two main consecutive stages: filling process and solidification process. In filling process, gating system, comprising the pouring cup, runner, sprue, sprue well and in-gate, is designed to guide molten metal into the mould cavity for filling. The riser system is used to compensate for shrinkage caused by casting solidification [1].

Mould filling is a very important step in determining the quality of a casting. The fluid flow phenomenon during the mould filling is closely related to the casting quality, surface finish and macro segregation of the cast part and mould erosion. Dimensional accuracy of casting is affected by the flow in the mould cavity. Modeling of the mould filling is a very complex process, since many

physical phenomena, such as free surface flow, turbulence, surface tension and combination of fluid flow with heat transfer, should be considered. In order to take all these parameters into account, the computing technique tends to be complicated [2].

Pouring turbulence during mould filling is detrimental to the quality of sand castings. The formation of various castings defects could be directly related to the fluid flow phenomena involved in the stage of mould filling. For instance, vigorous steam could cause mould erosion; highly turbulent flows could result in air and inclusions entrapments; and relatively slower filling might generate cold shut [2]. Furthermore, porosity, a common defect in casting also could result from improper design of gating system [3].

The objective of a gating system is to get enough metal into the mould cavity before the metal starts to solidify, minimize turbulence to avoid trapping gases into the mould and establish the best possible temperature gradient in the solidifying casting so that

* Corresponding Author

(francis.inegbedion@uniben.edu) ORCID ID 0000-0002-2142-8079
(jamesorji9396@gmail.com) ORCID ID 0000-0002-6098-6663

Cite this article

Inegbedion, F., & Orji, J. C. (2023). Determination of the critical drop height and critical flow velocity of aluminum alloy (AL-91% Mg-8% Fe-0.4% Zn-0.2%) in gravity sand casting. Turkish Journal of Engineering, 7(2), 149-156

the shrinkage occurs in the gating system not in the cast [4]. For proper functioning of the gating system, the rate at which molten metal is poured to fill the mould cavity must be controlled [5].

These problems not only lead to a long casting development cycle, but also a low reliability of casting design due to variations of individual knowledge and experience. Getting the liquid metal out of the crucible into the mould is a critical step in the casting process. Most casting scrap arises during these few seconds of mould filling. Therefore, the authors seek to streamline the several casting design guidelines by establishing the critical flow velocity and drop height of molten aluminum alloy as it flows down the sprue during gravity sand casting process, having a top riser opened to atmospheric pressure.

2. Method

2.1. Mathematical model employed

The continuity equation of a controlled volume and the finite element method were the models used in analyzing the critical flow velocity and critical drop height of the aluminum alloy.

2.1.1 Analysis of molten metal flow in the mould sprue in gravity sand casting

The governing equations of molten metal flow in gravity sand casting and the finite element method were used in this analysis.

2.1.2 Governing equations

The governing equations of molten metal flow in casting mould cavity are governed by the continuity equations in cylindrical axisymmetric coordinate as shown in Equation (1) [6–10].

$$\frac{\partial P}{\partial t} + \frac{1}{r} \frac{\partial}{\partial r}(ru_r) + \frac{\partial u_z}{\partial z} = 0 \quad (1)$$

At steady state $\frac{\partial}{\partial t} = 0$ and Equation (1) becomes

$$\frac{1}{r} \frac{\partial}{\partial r}(ru_r) + \frac{\partial u_z}{\partial z} = 0 \quad (2)$$

The solutions to Equation (2) can only be obtained by applying the appropriate initial and boundary conditions. The initial conditions for pressure and temperature fields are given by Equation (3) [4,6].

$$p(z, t_0) = p_0(z), \quad T(r, z, t_0) = T_0(r, z) \quad (3)$$

The boundary conditions specified in the considered problem are as indicated in Equations (4) to (7), [5,11–15].

At the inlet gate:

$$u_n = u_{in} \quad u_t = 0 \quad \text{or} \quad p = p_{in} \quad (4)$$

At the mould wall:

$$u_r = u_z = 0, \quad \frac{\partial p}{\partial n} = 0 \quad (5)$$

At the flow front:

$$p = 0 \quad (6)$$

At the cavity center line:

$$\frac{\partial p}{\partial n} = 0 \quad \frac{\partial u_t}{\partial r} = 0 \quad u_r = 0 \quad u_z = u \quad (7)$$

The solutions to Equations (2) were obtained using the finite element method in the weighted residuals formulation [16–18].

2.2. Finite element solution of molten metal flow in the mould sprue

The velocity distribution over the domain of interest is discretized into finite element having M nodes, using suitable interpolation models for $u^{(e)}$ in element e as:

$$u_{(r,z)} = \sum_{i=1}^m w(r, z) u_i = [w]\{u\} \quad (8)$$

and we developed the velocity distribution for Equation (2) using the finite element method, seeking an approximate solution over each finite element. The weighted residual and the weighted integral of Equation (2) are Equations (9) and (10) respectively.

$$w_{(r,z)} \left[\frac{1}{r} \frac{\partial u_r}{\partial r} + \frac{\partial u_z}{\partial z} \right] = 0 \quad (9)$$

$$\int_{\Omega_e} w_{(r,z)} \left[\frac{1}{r} \frac{\partial u_r}{\partial r} + \frac{\partial u_z}{\partial z} \right] dr dz = 0 \quad (10)$$

We integrated Equation (10) by parts (Equation (11)), to obtain the weak form of Equations (2).

$$-\int_{\Omega_e} \left(u_r \frac{1}{r} \frac{\partial w}{\partial r} + u_z \frac{\partial w}{\partial z} \right) \partial r \partial z + w \left(u_z + u_r \frac{1}{r} \right) \Big|_{\Omega_e} = 0 \quad (11)$$

The finite element model (Equation 13) was developed by substituting Equations (8) and (10) into Equation (11) to obtain Equation (12).

$$\int_{\Omega_e} w \left(\frac{1}{r} \frac{\partial w}{\partial r} + \frac{\partial w}{\partial z} \right) \partial r \partial z \{u\} = w \left(u_z + u_r \frac{1}{r} \right) \Big|_{\Omega_e} \quad (12)$$

In matrix form Equation (12) becomes

$$[K]_{ij}^e \{u\} = \{Q\}_{ij}^e \quad (13)$$

Where $|K_{ij}^e|$ the M x M matrix is

$$|K_{ij}^e| = \int_{\Omega_e} w \left(\frac{1}{r} \frac{\partial w}{\partial r} + \frac{\partial w}{\partial z} \right) \partial r \partial z \quad (14)$$

and $\{Q_{ij}^e\}$ represented by M x 1 column matrix is

$$\{Q_{ij}^e\} = w \left(u_z + u_r \frac{1}{r} \right) \Big|_{\Omega_e} \quad (15)$$

To simplify the $|K_{ij}^e|$ and $\{Q_{ij}^e\}$, we used a linear rectangular element (Figure 1) to develop our interpolation model

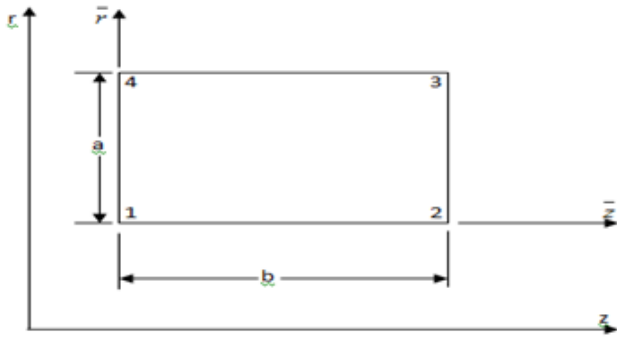


Figure 1. Geometry of the element

Firstly, we obtained the interpolation model for the K^e matrices by considering an approximation of the form:

$$w(r, z) = c_1 + c_2 r + c_3 z + c_4 r z \quad (16)$$

and used a linear rectangular element sides a and b (with $r = a$ and $b = z$) (Figure 1).

$$w(r, z) = c_1 + c_2 a + c_3 b + c_4 ab \quad (17)$$

and require

$$w_1 = w(0,0) = c_1$$

$$w_2 = w(a,0) = c_1 + c_2 a$$

$$w_3 = w(a,b) = c_1 + c_2 a + c_3 b + c_4 ab$$

$$w_4 = w(0,b) = c_1 + c_3 b$$

(18)

The solutions for $c_i (i = 1, \dots, 4)$, in Equations (18) are

$$c_1 = w_1 \quad c_2 = \frac{w_2 - c_1}{a} = \frac{w_2 - w_1}{a} \quad (19)$$

$$c_3 = \frac{w_4 - c_1}{b} = \frac{w_4 - w_1}{b}$$

$$c_4 = \frac{w_3 - c_1 - c_2 a - c_3 b}{ab} = \frac{w_3 - w_1 - w_2 - w_1 - w_4 - w_1}{ab} = \frac{w_3 - w_4 + w_1 - w_2}{ab}$$

We substituted Equation (19) into Equation (17) and noting that $a = r$ and $b = z$ to obtain Equation (20)

$$w(r, z) = \left(1 - \frac{r}{a}\right) \left(1 - \frac{z}{b}\right) w_1 + \frac{r}{a} \left(1 - \frac{z}{b}\right) w_2 + \frac{r z}{ab} w_3 + \frac{z}{b} \left(1 - \frac{r}{a}\right) w_4 \quad (20)$$

Equation (20) becomes Equation (21)

$$w(r, z) = \theta_1 w_1 + \theta_2 w_2 + \theta_3 w_3 + \theta_4 w_4 \quad (21)$$

Where

$$\begin{aligned} \theta_1 &= \left(1 - \frac{r}{a}\right) \left(1 - \frac{z}{b}\right) & \theta_2 &= \frac{r}{a} \left(1 - \frac{z}{b}\right) \\ \theta_3 &= \frac{r z}{ab} & \theta_4 &= \frac{z}{b} \left(1 - \frac{r}{a}\right) \end{aligned} \quad (22)$$

We differentiated Equation (22) with respect to r and z to obtain Equation (23).

$$\begin{aligned} \frac{d\theta_1}{dr} &= \left(-\frac{1}{a}\right) \left(1 - \frac{z}{b}\right) = \left(-\frac{1}{a} + \frac{z}{ab}\right) \\ \frac{d\theta_1}{dz} &= \left(-\frac{1}{b}\right) \left(1 - \frac{r}{a}\right) = \left(-\frac{1}{b} + \frac{r}{ab}\right) \\ \frac{d\theta_2}{dr} &= \frac{1}{a} \left(1 - \frac{z}{b}\right) = \frac{1}{a} - \frac{z}{ab} \\ \frac{d\theta_2}{dz} &= -\frac{r}{ab} \\ \frac{d\theta_3}{dr} &= \frac{z}{ab} \\ \frac{d\theta_3}{dz} &= \frac{r}{ab} \\ \frac{d\theta_4}{dr} &= -\frac{z}{ab} \\ \frac{d\theta_4}{dz} &= \frac{1}{b} \left(1 - \frac{r}{a}\right) = \frac{1}{b} - \frac{r}{ab} \end{aligned} \quad (23)$$

To derive the respective $|K_{ij}^e|$ values we used a four linear rectangular element (Figure 2) to obtain Equation (24).

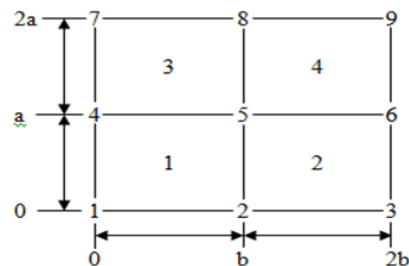


Figure 2. Four Linear Rectangular Elements

$$K_{11}^1 = \int_0^b \int_0^a \left[\left(\left(-\frac{1}{a} \right) \left(1 - \frac{z}{b} \right) \right)^2 + \left(\left(-\frac{1}{b} \right) \left(1 - \frac{r}{a} \right) \right)^2 \right] drdz = \frac{a}{3b} + \frac{b}{3a} \quad (24a)$$

$$K_{12}^1 = \int_0^b \int_0^a \left[\left(\frac{-1}{a} + \frac{z}{ab} \right)^2 + \left(\frac{-1}{b} + \frac{r}{ab} \right) \left(-\frac{r}{ab} \right) \right] drdz = \frac{a}{6b} + \frac{b}{3a} \quad (24b)$$

$$K_{13}^1 = \int_0^b \int_0^a \left[\left(\frac{-1}{a} + \frac{z}{ab} \right) \left(\frac{z}{ab} \right) + \left(\frac{-1}{b} + \frac{r}{ab} \right) \left(\frac{r}{ab} \right) \right] drdz = \frac{-a}{6b} - \frac{b}{6a} \quad (24c)$$

$$K_{14}^1 = \int_0^b \int_0^a \left[\left(\frac{-1}{a} + \frac{z}{ab} \right) \left(-\frac{z}{ab} \right) + \left(\frac{-1}{b} + \frac{r}{ab} \right) \left(\frac{1-r}{ab} \right) \right] drdz = \frac{a}{3b} + \frac{b}{6a} \quad (24d)$$

$$K_{21}^1 = K_{12}^1 = \frac{a}{6b} + \frac{b}{3a} \quad (24e)$$

$$K_{22}^1 = \int_0^b \int_0^a \left[\left(\frac{1}{a} - \frac{z}{ab} \right)^2 + \left(-\frac{r}{ab} \right)^2 \right] drdz = \frac{a}{3b} + \frac{b}{3a} \quad (24f)$$

$$K_{23}^1 = \int_0^b \int_0^a \left[\left(\frac{1}{a} - \frac{z}{ab} \right) \left(\frac{z}{ab} \right) + \left(-\frac{r}{ab} \right) \left(\frac{r}{ab} \right) \right] drdz = \frac{b}{6a} - \frac{a}{3b} \quad (24g)$$

$$K_{24}^1 = \int_0^b \int_0^a \left[\left(\frac{1}{a} - \frac{z}{ab} \right) \left(-\frac{z}{ab} \right) + \left(-\frac{r}{ab} \right) \left(\frac{1-r}{ab} \right) \right] drdz = \frac{b}{6a} - \frac{a}{6b} \quad (24h)$$

$$K_{31}^1 = K_{13}^1 = \frac{-a}{6b} - \frac{b}{6a} \quad K_{32}^1 = K_{23}^1 = \frac{b}{6a} - \frac{a}{3b} \quad (24i)$$

$$K_{33}^1 = \int_0^b \int_0^a \left[\left(\frac{z}{ab} \right)^2 + \left(\frac{r}{ab} \right)^2 \right] drdz = \frac{a}{3b} + \frac{b}{3a} \quad (24j)$$

$$K_{34}^1 = \int_0^b \int_0^a \left[\left(\frac{z}{ab} \right) \left(-\frac{z}{ab} \right) + \left(\frac{r}{ab} \right) \left(\frac{1-r}{ab} \right) \right] drdz = \frac{a}{6b} - \frac{b}{3a} \quad (24k)$$

$$K_{41}^1 = K_{14}^1 = \frac{a}{3b} + \frac{b}{6a} \quad K_{42}^1 = K_{24}^1 = \frac{b}{6a} - \frac{a}{6b} \quad K_{43}^1 = K_{34}^1 = \frac{a}{6b} - \frac{b}{3a} \quad (24l)$$

$$K_{44}^1 = \int_0^b \int_0^a \left[\left(-\frac{z}{ab} \right)^2 + \left(\frac{1-r}{ab} \right)^2 \right] drdz = \frac{a}{3b} + \frac{b}{3a} \quad (24m)$$

The $|K_{ij}^e|$ matrix is therefore Equations (25) and (26)

$$K = \begin{bmatrix} \frac{a}{3b} + \frac{b}{3a} & \frac{a}{6b} + \frac{b}{3a} & \frac{-a}{6b} - \frac{b}{6a} & \frac{a}{3b} + \frac{b}{6a} \\ \frac{a}{6b} + \frac{b}{3a} & \frac{a}{3b} + \frac{b}{3a} & \frac{6a}{6a} - \frac{3b}{3a} & \frac{6a}{6a} - \frac{6b}{3a} \\ \frac{-a}{6b} - \frac{b}{6a} & \frac{6a}{6a} - \frac{3b}{3a} & \frac{a}{a} + \frac{b}{b} & \frac{a}{a} - \frac{b}{b} \\ \frac{a}{3b} + \frac{b}{6a} & \frac{6a}{6a} - \frac{6b}{6b} & \frac{6a}{6a} - \frac{3b}{3a} & \frac{6b}{3b} + \frac{3a}{3a} \end{bmatrix} \quad (25)$$

$$K = \frac{b}{6a} \begin{bmatrix} 2 & -2 & -1 & 1 \\ -2 & 2 & 1 & -1 \\ -1 & - & 2 & -2 \\ 1 & -1 & -2 & 2 \end{bmatrix} + \frac{a}{6b} \begin{bmatrix} 2 & 1 & -1 & -2 \\ 1 & 2 & -2 & -1 \\ -1 & -2 & 2 & 1 \\ -2 & -1 & 1 & 2 \end{bmatrix} \quad (26)$$

If $a = 4$ and $b = 1$ Equation (26) becomes

$$K = \begin{bmatrix} 1.4166 & 0.5834 & -0.7084 & -1.2916 \\ 0.5834 & 1.4166 & -1.2916 & -0.7084 \\ -0.7084 & -1.2916 & 1.4166 & 0.5834 \\ -1.2916 & -0.7084 & 0.5834 & 1.4166 \end{bmatrix} \tag{27}$$

Let, $K^1 = K^2 = K^3 = K^4$, therefore

$$K_{ij}^e = K^1 + K^2 + K^3 + K^4 \tag{28}$$

$$K_{ij}^e = \begin{bmatrix} 1.4166 & 0.5834 & -0.7084 & -1.2916 \\ 0.5834 & 1.4166 & -1.2916 & -0.7084 \\ -0.7084 & -1.2916 & 1.4166 & 0.5834 \\ -1.2916 & -0.7084 & 0.5834 & 1.4166 \end{bmatrix} + \begin{bmatrix} 1.4166 & 0.5834 & -0.7084 & -1.2916 \\ 0.5834 & 1.4166 & -1.2916 & -0.7084 \\ -0.7084 & -1.2916 & 1.4166 & 0.5834 \\ -1.2916 & -0.7084 & 0.5834 & 1.4166 \end{bmatrix} + \begin{bmatrix} 1.4166 & 0.5834 & -0.7084 & -1.2916 \\ 0.5834 & 1.4166 & -1.2916 & -0.7084 \\ -0.7084 & -1.2916 & 1.4166 & 0.5834 \\ -1.2916 & -0.7084 & 0.5834 & 1.4166 \end{bmatrix} + \begin{bmatrix} 1.4166 & 0.5834 & -0.7084 & -1.2916 \\ 0.5834 & 1.4166 & -1.2916 & -0.7084 \\ -0.7084 & -1.2916 & 1.4166 & 0.5834 \\ -1.2916 & -0.7084 & 0.5834 & 1.4166 \end{bmatrix} \tag{29}$$

The assembled K_{ij}^e matrix using Figure 2 becomes Equations (30) and (31)

$$K_{ij}^e = \begin{bmatrix} K_{11}^1 & K_{12}^1 & 0 & K_{14}^1 & K_{13}^1 & 0 & 0 & 0 & 0 \\ K_{21}^1 & K_{22}^1 + K_{11}^2 & K_{12}^2 & K_{24}^1 & K_{23}^1 + K_{14}^2 & K_{23}^2 & 0 & 0 & 0 \\ 0 & K_{21}^2 & K_{22}^2 & 0 & K_{24}^2 & K_{23}^2 & 0 & 0 & 0 \\ K_{41}^1 & K_{42}^2 & 0 & K_{44}^1 + K_{11}^3 & K_{43}^1 + K_{12}^3 & 0 & K_{14}^3 & K_{13}^3 & 0 \\ K_{31}^1 & K_{32}^1 + K_{41}^2 & K_{42}^2 & K_{34}^1 + K_{21}^3 & K_{33}^1 + K_{44}^2 + K_{22}^3 + K_{11}^4 & K_{43}^2 + K_{12}^4 & K_{24}^3 & K_{23}^3 + K_{14}^4 & K_{13}^4 \\ 0 & K_{31}^2 & K_{32}^2 & 0 & K_{34}^2 + K_{21}^4 & K_{33}^2 + K_{22}^4 & 0 & K_{24}^4 & K_{23}^4 \\ 0 & 0 & 0 & K_{41}^3 & K_{42}^4 & 0 & K_{44}^4 & K_{43}^4 & 0 \\ 0 & 0 & 0 & K_{31}^3 & K_{32}^3 + K_{41}^4 & K_{42}^4 & K_{34}^3 & K_{33}^3 + K_{44}^4 & K_{43}^4 \\ 0 & 0 & 0 & 0 & K_{31}^4 & K_{32}^4 & 0 & K_{34}^4 & K_{33}^4 \end{bmatrix} \tag{30}$$

$$K_{ij}^e = \begin{bmatrix} 1.4166 & 0.5834 & 0 & -1.2916 & -0.7084 & 0 & 0 & 0 & 0 \\ 0.5834 & 2.8332 & 0.5834 & -0.7084 & -2.5832 & -1.2916 & 0 & 0 & 0 \\ 0 & 0.5834 & 1.4166 & 0 & -0.7084 & -1.2916 & 0 & 0 & 0 \\ -1.2916 & -0.7084 & 0 & 2.8331 & 1.1668 & 0 & -1.2916 & -0.7084 & 0 \\ -0.7084 & -2.5832 & -0.7084 & 2 & 5.6664 & 1.1668 & -0.7084 & -2.5832 & -0.7084 \\ 0 & -0.7084 & -1.2916 & 0 & 1.1668 & 1.1668 & 0 & -0.7084 & -1.2916 \\ 0 & 0 & 0 & -0.7084 & -1.2916 & 0 & 0.5834 & 1.4166 & 0 \\ 0 & 0 & 0 & -0.7084 & -2.5832 & -0.7084 & 0.5834 & 2.8332 & 0.5834 \\ 0 & 0 & 0 & 0 & -0.7084 & -1.2916 & 0 & 0.5834 & 1.4166 \end{bmatrix} \tag{31}$$

Applying the boundary conditions on Equations (4) through (7), yielded Equation (32).

$$\{\phi_{ij}^e\} = \begin{bmatrix} 0 \\ 0 \\ 0 \\ 0 \\ 1 \\ 0 \\ 0 \\ 1 \\ 0 \end{bmatrix} \tag{32}$$

We substituted Equations (31) and (32) into Equation (13) and obtained Equation (33)

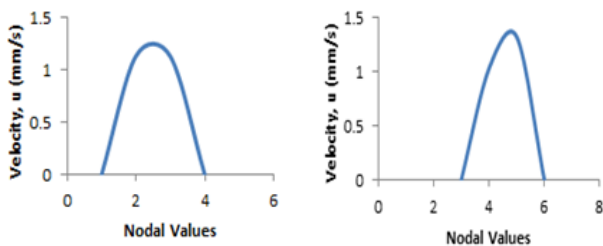
$$\begin{bmatrix}
 1.4166 & 0.5834 & 0 & -1.2916 & -0.7084 & 0 & 0 & 0 & 0 \\
 0.5834 & 2.8332 & 0.5834 & -0.7084 & -2.5832 & -1.2916 & 0 & 0 & 0 \\
 0 & 0.5834 & 1.4166 & 0 & -0.7084 & -1.2916 & 0 & 0 & 0 \\
 -1.2916 & -0.7084 & 0 & 2.8331 & 1.1668 & 0 & -1.2916 & -0.7084 & 0 \\
 -0.7084 & -2.5832 & -0.7084 & 2 & 5.6664 & 1.1668 & -0.7084 & -2.5832 & -0.7084 \\
 0 & -0.7084 & -1.2916 & 0 & 1.1668 & 1.1668 & 0 & -0.7084 & -1.2916 \\
 0 & 0 & 0 & -0.7084 & -1.2916 & 0 & 0.5834 & 1.4166 & 0 \\
 0 & 0 & 0 & -0.7084 & -2.5832 & -0.7084 & 0.5834 & 2.8332 & 0.5834 \\
 0 & 0 & 0 & 0 & -0.7084 & -1.2916 & 0 & 0.5834 & 1.4166
 \end{bmatrix}
 \begin{Bmatrix}
 u_1 \\
 u_2 \\
 u_3 \\
 u_4 \\
 u_5 \\
 u_6 \\
 u_7 \\
 u_8 \\
 u_9
 \end{Bmatrix}
 =
 \begin{Bmatrix}
 0 \\
 0 \\
 0 \\
 0 \\
 1 \\
 0 \\
 0 \\
 1 \\
 0
 \end{Bmatrix}
 \quad (33)$$

3. Results and Discussion

“Table 1” shows the results for the finite element analysis. Figure 3, are the graphs of velocity against nodal values, showing the velocity profile at different cross sections along the mould’s sprue. These profiles are parabolic in shape with the maximum velocity at the center.

Table 1. Finite Element Results

Nodes	U	Velocity (mm/s)
1	u_1	1.1152
2	u_2	1.1108
3	u_3	0.000
4	u_4	1.0088
5	u_5	1.3055
6	u_6	0.000
7	u_7	0.7337
8	u_8	1.7030
9	u_9	0.000



Figures 3(a) and (b). Graphs of velocity against nodal values showing the velocity profile at different cross sections along the mould’s sprue in gravity sand casting

The maximum velocity of molten metal flow obtained from this work (2565mm/s), when compared with the work of Rohaya [19] (Table 2 and Figure 4) which ranged from 2300mm/s to 3200mm/s showed that the danger of casting defects as a result of molten metal flow above the critical velocity can be avoided. Meanwhile below the critical velocity the melt was safe from entrainment problem.

The solutions obtained from this work (2565mm/s) were also compared with the work of Feng [1] (Table 3 and Figure 5) which ranged from 260mm/s to 2850mm/s, the comparison showed that the danger of

air entrainment leading to defect as a result of molten metal flow above the critical velocity can be avoided.

Table 2. Comparison between this work and Rohaya [19]

Z	This Work	Rohaya
1	135.76	500
2	2245.54	2300
3	2564.81	3200
4	0.0000	0.000

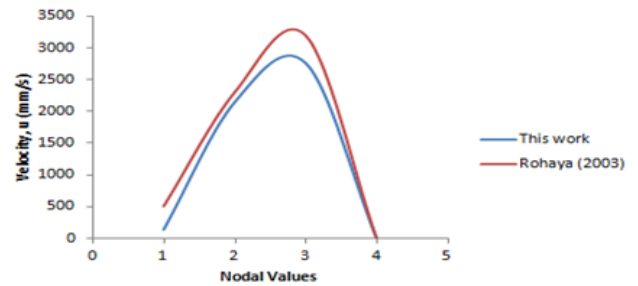


Figure 4. Graph of velocity against nodal values showing the velocity profile at a cross section along the sprue in gravity sand casting for this work and Rohaya.

Table 3. Comparison between this work and Feng [1].

Z	This Work	Feng
1	135.76	260
2	2245.54	2450
3	2564.81	2850
4	0.0000	0.000

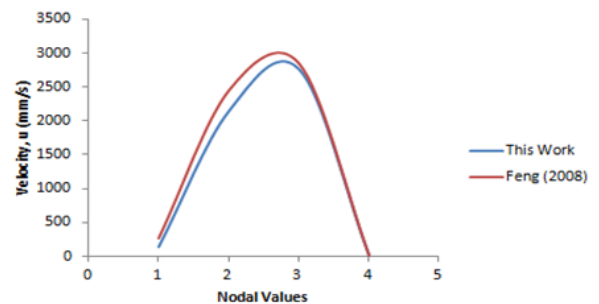


Figure 5. Graph of velocity against nodal values showing the velocity profile at a cross section along the sprue in gravity sand casting for this work and Feng [1]

The maximum velocity of molten metal flow obtained from this work (2565mm/s), when compared with the work of Inegbedion and Akpobi [20] (Table 4 and Figure

6) which ranged from 130.76mm/s to 2754.81mm/s showed that the danger of casting defects as a result of molten metal flow above the critical velocity can be avoided. Meanwhile below the critical velocity the melt was safe from entrainment problem.

Table 4. Comparison between this work and Inegbedion and Akpobi [20]

Z	This Work	Inegbedion and Akpobi
1	135.76	130.76
2	2245.54	2135.54
3	2564.81	2754.81
4	0.0000	0.0000

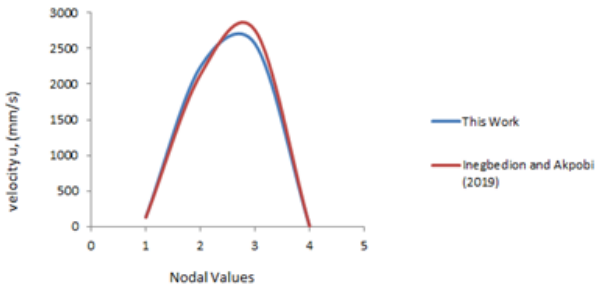


Figure 6. Graph of velocity against nodal values showing the velocity profile at a cross section along the sprue in gravity sand casting for this work and Inegbedion and Akpobi [20]

To validate the results obtained, we produced various casts using these results. The cast produced showed that sprue height below the critical drop height prevented casting defects associated with pouring velocities while sprue height above the critical drop height the danger of casting defects associated with pouring velocities above the critical velocity could not be avoided.

“Figure 7”, showed the various surface defects that can occur in casting when cast are produced using sprue height above the critical drop height (377mm): The molten metal is not safe from casting defects because the pouring velocity exceeded the critical flow velocity. These defects can be avoided with pouring velocities below the critical velocity (Figure 8).

It is evident from Figure 8 that all casting defects associated with pouring, using sprue height above the critical drop height, can be avoided if cast can be produced using sprue heights below the critical drop height. In this case, the melt is safe since the pouring velocity is below the critical velocity.

4. Conclusion

Results obtained from the analysis of molten metal flow showed that there exist a critical velocity and critical drop height for molten metal flow, to prevent entrainment of air and porosity problem in casting.

The finite element analysis of molten metal flow in the mould sprue using continuity equation was used in this research work. The velocity distribution of the flow of molten metal were developed using the finite element method. The weighted integral of the equation was obtained, the weak form of the equation was developed and the finite element model was determined. The various matrices were assembled, solved and solutions

obtained by using an eight linear element of nine nodes and a four linear rectangular element. By using appropriate interpolation function and boundary conditions, the solutions to the equations were obtain and validated using relevant literatures.



Figure 7. Cast produced for different sprue height above the critical drop height: (a) 450mm sprue height (b) 400mm sprue height. The critical drop height is 377mm.

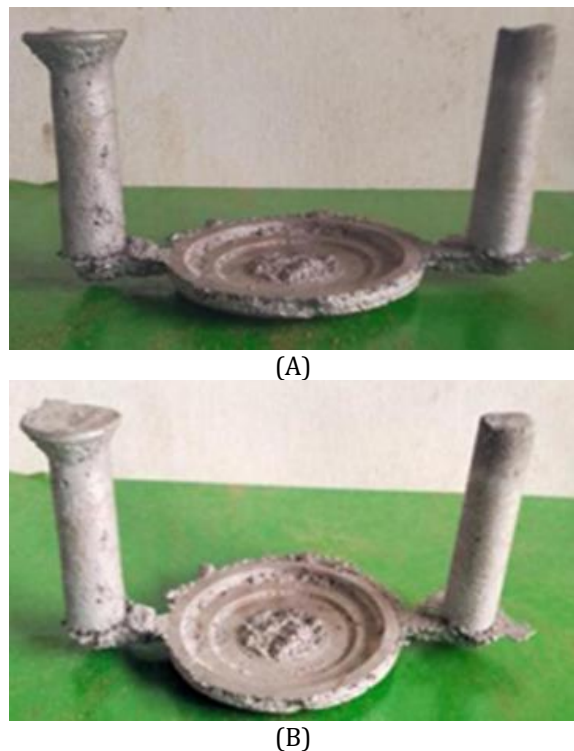


Figure 8. cast produced for different sprue height below the critical drop height: (a) 250mm sprue height (b) 220mm sprue height. The critical drop height is 377mm

Finally, to avoid entrainment of air and porosity problems in casting, the critical velocity and critical drop

height of molten metal as it flows down the sprue of casting mould was established. Further analysis of the flow of fluid in casting mould showed that molten metal flow below the critical velocity will prevent casting defects because flow is smooth and laminar. The critical drop height obtained from this work was used to produce various casts. The results obtained showed that casting defects can be avoided when cast are produced using sprue height below the critical drop height while cast produced using sprue height above the critical drop height the danger of casting defects could not be avoided. Therefore, the critical velocity and critical drop height obtained in this work will prevent air entrainment and porosity problem in casting. Consequently, foundry engineers will no longer rely on their individual knowledge and experience or perform trial and error runs before carrying out any casting process. This will reduce casting development cycle, defects and production time.

Author contributions

Francis Inegbedion: Conceptualization, Visualization, Methodology, Investigation, Writing-Reviewing and Editing **James Chinedu Orji:** Methodology, Investigation, Data curation, Writing-Original draft preparation

Conflicts of interest

The authors declare no conflicts of interest.

References

1. Feng L., (2008). Optimized Design of Gating/Riser System in Casting Based on CAD and Simulation Technology, Submitted to the faculty of the Worcester Polytechnic Institute in partial fulfillment of the requirements for degree of Master of science in Manufacturing Engineering.
2. Attar E.H., Babaei R.P., Asgari K., Davami P., (2005). Modelling of air pressure effects in casting moulds, *Journal of Modelling and Simulation in Materials Science and Engineering*, 13, 903-917
3. Lee P. D., Chirazi A., & See D. (2001). Modelling micro porosity in Aluminium - Silicon alloys: a review, *Journal of Light Metals*, 1, 15-30
4. Sowa L. (1998). Model of the Casting Solidification taking into consideration the motion of liquid phase, *Archives of Mechanical technology and Automatization*, 18, 287 – 296
5. Sowa, L., (2010). Mathematical Modelling of the Filling Process of a slender mould cavity, *Scientific Research of the Institute of Mathematics and Computer Science*, 9(2) 219-227
6. Salih A. (2011). Conservation Equations of fluid Dynamics, Department of Aerospace Engineering, Indian Institute of space Science and technology, Thiruvananthapuram publishers 4-7
7. Sowa L. & Bokota A. (2007). Numerical Modelling of Thermal and Fluid Flow Phenomena in the Mould Channel, *Archives of Foundry Engineering*, 7(4), 165 – 168.
8. Sowa, L., (2010), Numerical Analysis of the Thermal and Fluid Flow Phenomena of the Fluidity test, *Archives of Foundry Engineering*, 10(1), 157 – 160.
9. Bird R. B., Stewart W.E., & Lightfoot E.N., (2002). *Transport Phenomena*, 2nd edition, Wiley: NY.
10. Aris, R., (1962). *Vectors, Tensors, and the Basic Equations of Fluid Mechanics*, Prentice Hall Publishers, Englewood Cliffs, NJ
11. Ik-Tae I., Woo-Seung K., & Kwan-Soo L., (2001). A unified analysis of filling and solidification in casting with natural convection, *International Journal of Heat and Mass Transfer*, 44, 1507-1515
12. Sowa, L., Sczygiol, N. Domoilski, T., & Bokota, A., (2008). Simplified Model of Metal Solidification in the Thin Plane Cavity of the Casting Mould, *Archives of Foundry Engineering*, 8(1), 309 – 312
13. Bokota A. & Sowa L. (2010). Numerical Modelling of the thermal and fluid flow phenomena of the fluidity test, *Archives of Foundry Engineering* 10(1), 15–18
14. Mishima S., & Szekely J. (1989). The modelling of fluid flow and heat transfer in mould filling, *ISIJ International*, 29(4), 324-332
15. Majchrzak E., Jasinski M., & Kaluza G. (2004). Sensitivity analysis of solidification process with respect to the geometrical parameters of casting and mould, *Archives of Foundry Engineering*, 4(14) 279-284.
16. Reddy J. N., (2006). *An Introduction to the Finite Element Method*, Third Edition, International Edition McGraw- Hill., 146 – 147, 441 - 442.
17. Singiresu S. R. (2004). *The Finite Element Methods in Engineering*, fourth edition, Elsevier Science and Technology Books Publisher
18. Hutton V. D. (2004). *Fundamentals of Finite Element Analysis*, 1st Edition, McGraw-Hill Companies, Inc. 293 – 295
19. Rohaya B. D. (2013). Design and Analysis of Casted LM6 - TIC in Designing of Production Tooling, Faculty of Manufacturing Engineering, Universiti Teknikal Malaysia Melaka (UTEM) 63 – 69
20. Inegbedion F. and Akpobi J.A. (2019). Determination of the Critical Velocity of Molten Metal Flow in Casting Mould Sprue, *International Journal of Engineering Trends and Technology (IJETT)* – 67(10), 27 – 33.





Collapse capacity assessment of non-ductile open ground story reinforced concrete frame

Emre Akin^{*1}, Emad Kanas¹

¹Mersin University, Civil Engineering Department, Türkiye

²Adnan Menderes University, Civil Engineering Department, Türkiye

Keywords

Reinforced Concrete
Infill Wall
Soft Story
Open Ground Story
Collapse Capacity

Research Article

DOI: 10.31127/tuje.1071965

Received: 11.02.2022

Accepted: 25.04.2022

Published: 26.04.2022

Abstract

It is a well-known fact that the absence of infill walls at the ground story, which is termed as "open ground story" may lead to a soft-story deficiency, especially in the case of non-ductile buildings. The previous severe earthquakes have shown that catastrophic destruction may occur in such a condition. Therefore, the seismic assessment of open ground story reinforced frames, where the effects of infill walls are incorporated, is of vital importance. However, the effects of infill walls are generally disregarded or considered indirectly in the seismic assessment procedures of the codes. This may mislead the actual condition of the open ground story buildings at different performance levels. This study aims to assess a non-ductile reinforced concrete frame with an open ground story regarding the collapse prevention performance level. The pushover and incremental dynamic analyses results are evaluated following the code limitations for collapse prevention. The results demonstrate the measure of misleading caused by the ignorance of infills at the upper stories while applying these code limitations.

1. Introduction

The previous studies reveal the influence of infill walls on the lateral behavior of buildings by a consideration of numerous parameters [1-7]. Yet, the knowledge of these members has been improving with the aid of latest analytical tools and models. The non-uniform placement of infills along the building elevation or in plan causes stiffness and strength irregularities [8-9]. The most common example is the open ground story (OGS) in which case the infills are absent in one story (generally the ground story). The OGS has the potential to cause soft/weak story deficiency which may depend on the characteristics of the structural system, masonry infills and ground motion [10]. Although there are certain regulations entailed by the codes to prevent soft/weak story deficiency [11-12] in the design, the assessment of existing buildings with OGS that were constructed in the absence of these regulations is a critical issue. A more approximate seismic assessment of these types of buildings requires taking the effects of infill walls into account.

In the current study, the collapse performance of a reinforced concrete frame that does not comply with the

current seismic design principles is assessed by comparison with the collapse prevention limits suggested by various seismic codes. The nonlinear pushover and incremental dynamic analyses were conducted for this purpose. The frame models were considered to have either OGS or not. To be used in the time history analyses, eleven selected earthquake ground motion records were matched with the design spectrum.

2. Numerical modeling

Seismostruct software [13] was used for the nonlinear analyses of the five-story, two-span planar RC frame. The frame that is illustrated in Fig. 1 belongs to an existing building which was also used by Kadas [14]. However, some slight alterations were done in the dimensions and reinforcement details of the members as given in Table 1, to obtain non-ductile structural characteristics. No additional cross ties were used for the confinement of the sections (i.e., only hoop reinforcement with two legs along both sectional directions). The characteristic compressive strength of

* Corresponding Author

(eakin@mersin.edu.tr) ORCID ID 0000-0003-1936-8916
(imad_alkanas@hotmail.com) ORCID ID 0000-0002-5905-4172

Cite this article

Akin, E., & Kanas, E. (2023). Collapse capacity assessment of non-ductile open ground story reinforced concrete frame. Turkish Journal of Engineering, 7(2), 157-165

concrete was 15 MPa. The characteristic yield strength of all reinforcements was 220 MPa.

The lateral response of the floor levels was assumed as a rigid diaphragm. The uniformly distributed beam dead loads were 12.36 kN/m in the first four stories and 9.62 kN in the last story. The live loads were 0.98 kN/m on all beams, except those at the roof where it had a value of 0.49 kN/m. The concrete specific weight was considered as 24 kN/m³. The specific weight was 8 kN/m³ for the infills. The second-order effects are considered in all analyses.

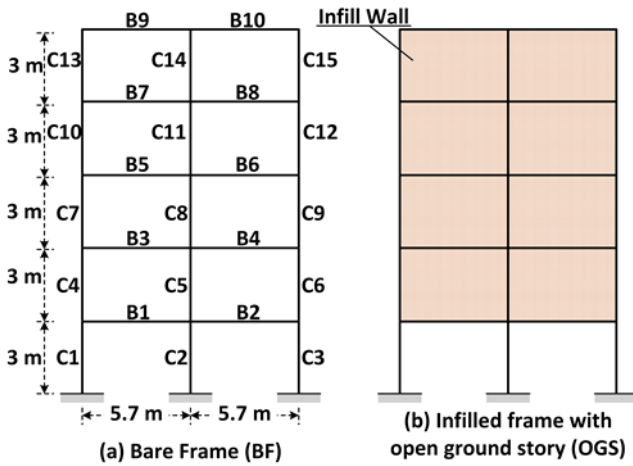


Figure 1. The models of (a) bare and (b) OGS frames

Table 1. The properties of the beams and columns

Section	Dimensions (mm×mm)	Longitudinal Reinforcement	Transverse Reinforcement
Column	500×500	10φ18	φ8/200 mm
Beam-Support	250×600	6φ18 (top) 4φ18 (bottom)	φ8/200 mm
Beam-Span		4φ18 (top) 6φ18 (bottom)	

The nonlinear model which is compatible with the relationship proposed by Mander et al. [15] and the cyclic rules of Martinez-Rueda and Elnashai [16] was employed for the concrete. The elastic modulus was calculated as 18200 MPa for the concrete according to ACI [17]. The strain at the ultimate strength of concrete was considered as 0.002 in compression. The modulus of elasticity was 2×10⁵ MPa for the steel reinforcement. The strain hardening was considered with a ratio of 0.005 for the steel. A distributed inelasticity model which was the inelastic force-based frame element of Seismostruct was employed for the RC members. Four integration sections were used, where a meshing with 100 fibers was conducted. The initial and final beam integration sections were formed by using the support sectional properties (Table 1) and the properties for the span sections were assigned to the others.

The masonry wall properties that are defined as “fair” quality by the American Society of Civil Engineers (ASCE) [18] were employed for the infill wall model of this study. Accordingly, the compressive strength (f_m), modulus of elasticity (E_m) and shear strength of the infill walls were quantified as 4.1 MPa, 2255 MPa and 0.14 MPa, respectively. The four-node inelastic infill panel element of Seismostruct software which consists of two struts for

the axial response and one strut for the shear response along each diagonal direction was employed for the nonlinear modeling of infill walls. The same definitions and assumptions are followed to constitute the infill wall models as described in a previous study by the first author Akin [10]. Therefore, these will not be repeated here once again to keep it abbreviated.

3. Analyses

3.1. Pushover Analyses

The eigenvalue analyses resulted in a fundamental vibration period of 1.13 s. for the BF and 0.71 s. for the OGS. Besides, the mode shape vector, $\{\Phi\}$ and mass matrix, $[m]$ were taken for the first (fundamental) modes. The generalized mass (M_1), base shear effective modal mass (M_1^*) and other modal properties (L_1 and Γ_1) were estimated in the first mode (designated by the subscript “1”) by using Eqns. (1)-(4). In these expressions, m_j is the total mass in the “j”th story and Φ_{j1} is the modal lateral deflection at the “j”th story corresponding to the first mode.

$$M_1 = \sum_{j=1}^{N=5} m_j \times \phi_{j1}^2 \tag{1}$$

$$L_1 = \sum_{j=1}^{N=5} m_j \times \phi_{j1} \tag{2}$$

$$\Gamma_1 = L_1 / M_1 \tag{3}$$

$$M_1^* = \Gamma_1 \times M_1 \tag{4}$$

The static pushover analyses (SPO) were conducted under lateral loading where the pattern of nominal loads was assumed as inverse triangular. These nominal lateral loads at the stories were allocated to each node according to the nodal masses. Fig. 2 illustrates the design spectrum that was utilized to determine the displacement at the target point. The design spectrum was determined for the location of the original building in accordance with the previous version of the Turkish Earthquake Code (TEC [19]) that was the official code at the time when this study started. An earthquake level corresponding to 475 years of return period was chosen for the design spectrum. The damping ratio was considered as 5%. The region of the design spectrum with constant acceleration was bounded by the corner periods of 0.10 s. (T_A) and 0.48 s (T_B). The capacity curves obtained by SPO analyses were converted into the spectral coordinates of the design spectrum. This was accomplished by converting base shear, V_b into spectral acceleration, S_a and roof drift, δ_{roof} into spectral displacement, S_d by utilizing Eqns. (5) and (6), respectively. Φ_{N1} is the modal lateral deflection at the roof level for the first mode (i.e., $j=N$).

$$S_a = V_b / M_1^* \tag{5}$$

$$S_d = \delta_{roof} / (\Phi_{N1} \times \Gamma_1) \tag{6}$$

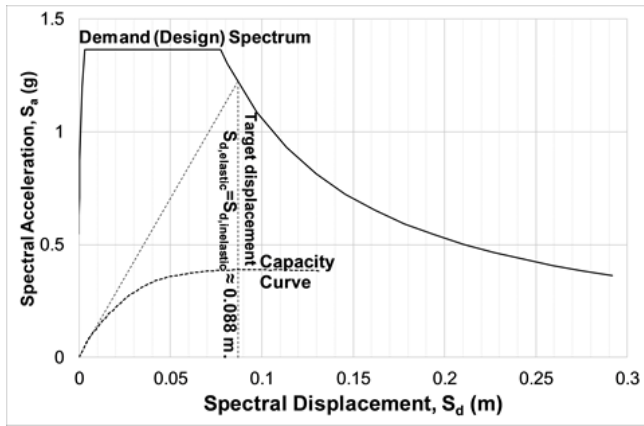


Figure 2. Estimation of the target displacement in the BF

The fundamental vibration periods (T_1) of all models were larger than T_B (upper limit for the region of constant acceleration). This enabled the utilization of the rule which states that the inelastic displacement demands, $S_{d,inelastic}$ may be taken as equal to the elastic displacement demands, $S_{d,elastic}$. Fig. 2 illustrates the determination of the displacement at the target point according to the TEC [12] for the bare frame. These spectral displacements could be converted to roof displacements at the target point by an inverted utilization of Eq. (6). This yielded a roof displacement of 0.113 m for the BF and 0.078 m for the OGS. The SPO analyses were conducted again up to a step where these determined roof displacements were attained. And finally, the inelastic demand parameters were obtained for the columns.

3.2. Incremental Dynamic Analyses (IDA)

The incremental dynamic analyses of the models were conducted under gradually increasing intensity of the applied acceleration time history records by use of scaling factors, changing between 0.1 and 1.3 with an increment of 0.2 at each step. During the analyses of some models, the convergence problems occurred and the analyses should have to be terminated before attaining the scale factor of 1.3. Even so, the quantity of the analysis steps was enough for a reasonable evaluation of the results in all cases. Eleven ground acceleration records, each belonging to a different event, were chosen for the IDA. The records were taken from the Pacific Earthquake Engineering Research Center (PEER) “NGA-West 2” database in conformity with a seismic scenario chosen according to the location of the building [19]. The parameters that were taken into account for this seismic scenario are listed in Table 2.

The chosen ground motion records were Darfield-New Zealand-2010, Duzce-Turkey-1999, Erzincan-1992, Imperial Valley-02-1940, Landers-1992, Kobe-Japan-1995, Kocaeli-Turkey-1999, Parkfield-1966, Sierra-Mexico-2010, Superstition Hills-02-1987, Tottori-Japan-2000. SeismoMatch software [20] was utilized to match the response spectra of these ground motion records with the design spectrum. The matching was completed in two steps having a maximum of 30% misfit tolerance. The matching was continued up to the periods of 1 s. and 4 s in the first and second steps, respectively. The spectra

that were matched with the design spectrum are shown in Fig. 3. The period of each model at the first mode and upper boundary for the constant acceleration zone, T_B is also marked in Fig. 3. These matched ground acceleration records were used for the IDA.

Table 2. Specifications of the seismic scenario

Parameter	Interval/Property
Type of Fault	Strike-Slip
Magnitude of Earthquake	6.0-7.8
Distance of Rupture (R_{RUP}) (km)	0-100
Distance of Joyner-Boore (R_{JB}) (km)	0-30
Shear Wave Velocity at the top 30 m of the subsurface (V_{s30}) (m/sec.)	100-400

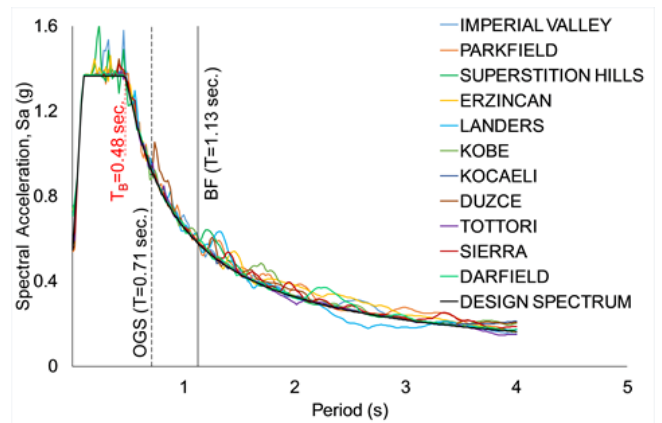


Figure 3. The spectrums of the chosen ground acceleration records matched with the design spectrum

4. Discussion of results

4.1. Results of SPO Analyses

The pushover curves are presented in Fig. 4 where the estimated target lateral drift at the roof level is also presented for the models. The non-ductile characteristic of both frames is explicit in this figure with a negative slope during the plastic phase of the response. When the capacity curves of both models are compared, the considerable increase in the initial rigidity of the OGS model compared to BF is clear. This is notable since it is attributed to the addition of infills in the absence of those at the ground story. A consequent alteration of the base shear demand may be expected in the OGS model due to the increased rigidity. On the other hand, it is obvious in Fig. 4 that there is no considerable base shear capacity increase in the OGS model in comparison to BF that may counterveil the altered demands.

At this stage, a probable concentration of inelastic demand parameters in the ground story columns of the OGS model compared to BF is evaluated. The concrete strain values at the columns of only the ground story are considered in this evaluation. However, the base shear demands and chord rotations at the ground and first story levels are taken into account for comparison. In Fig. 5, these demand parameters are assessed with respect to the limiting values of Eurocode 8 [11] and TEC [12] at different damage states. Here “SD” and “NC” correspond to the “Significant Damage” and “Near-Collapse” limit states of Eurocode 8, respectively. These limit states are

designated as “Controlled Damage” and “Collapse Prevention” in the TEC [12], respectively.

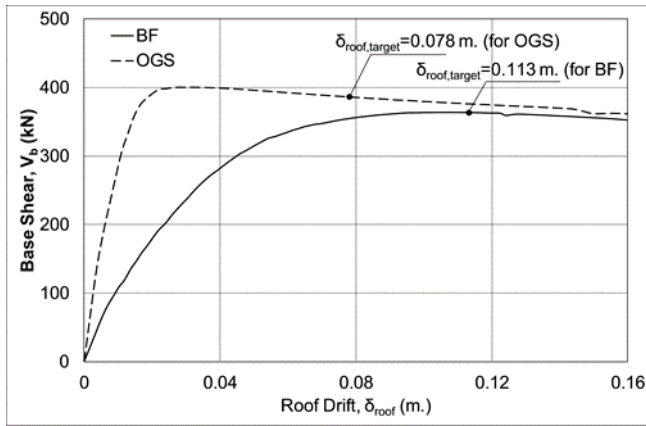


Figure 4. The static pushover analyses results of the BF and OGS models

The column sectional details that are provided in Table 1 and the properties of the materials given in the preceding sections were used for the calculation of the limit values of the codes. The resulting chord rotation capacity values are 0.0096 rad and 0.0128 rad at the SD and NC limit states, respectively. The NC limit in terms of shear force capacity was estimated as 163.8 kN. These limit values for the chord rotation and shear force were calculated according to the Eurocode 8 (i.e., sections A.3.2 and A.3.3 of part 3). On the other hand, section 5.8.1.1 of the TEC [12] was utilized to estimate the concrete strain capacity values of 0.0051 and 0.0068 for the SD and NC limit states, respectively. In Eurocode 8, the parameter that is employed to distinguish the priority of the members in terms of seismic resistance of the structure (γ_{el}) was taken to be 1.5 for the columns (as a primary element). The ratio between moment and shear at the end section was considered to be one-half of the column height as recommended by the TEC [12]. In the calculations of the limit states, the axial load on the columns was assumed as 560 kN. This value is the mean value for the highest axial loads at the ground story columns which occurred during the IDA step corresponding to the NC stated by FEMA 350 [21]. The definition of the NC limit using the IDA results according to FEMA 350 will be given in the next section. Only the reinforcements at the ends of the section ($4\phi 18$) were regarded as the tension or compression reinforcements. In other words, the probable contribution of the reinforcement at the mid-section ($2\phi 18$) to the tensile or compressive response was ignored. No diagonal reinforcement was considered since there is none in the section (i.e., $\rho_d=0$). The confinement effectiveness factor (α) was estimated as 0.42 with the same definition in Eurocode 8 [11] and TEC [12]. During the calculations according to Eurocode 8, the capacities were reduced with regard to the insufficient seismic detailing and the use of smooth bars for the longitudinal reinforcements. While applying these reductions, the longitudinal reinforcements were regarded as lapped at the member ends, which is a typical application for most of the buildings in Turkey. The length of the lapped bars (l_o) was assumed as equal to 50 times the diameter of the bar

(db_L). In the concrete strain capacity calculations according to TEC [12], only 30 percent of the lateral reinforcement was taken into account due to the use 90° hook ends of the stirrups as suggested by the code.

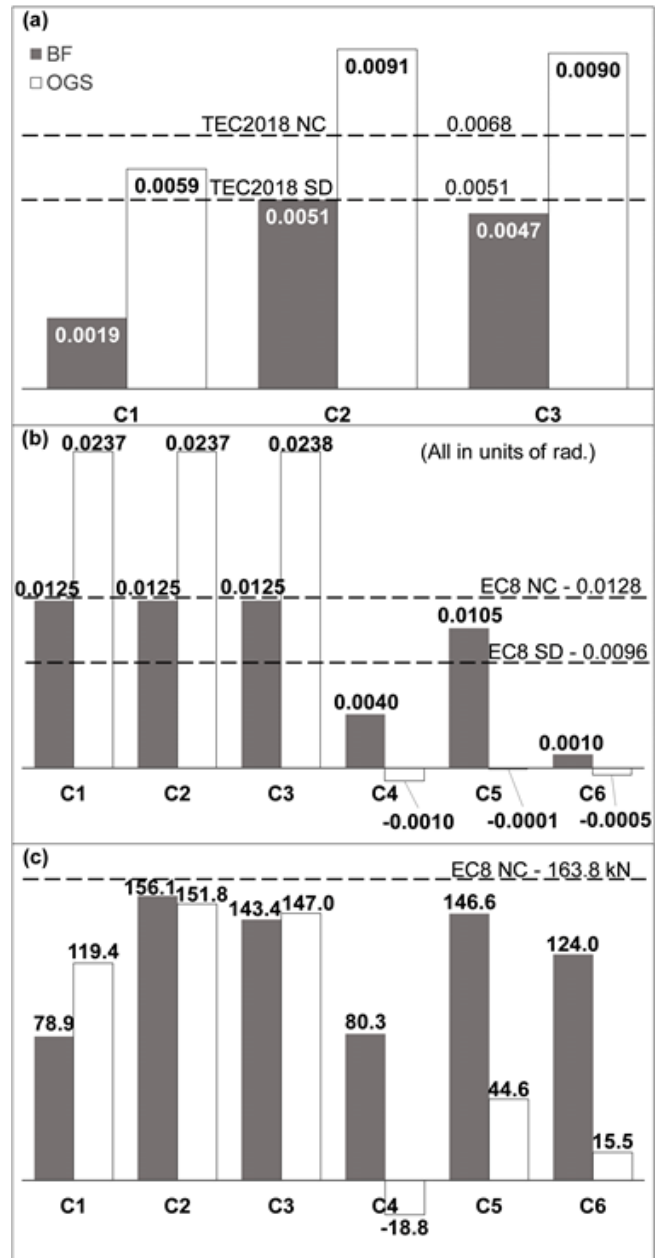


Figure 5. The results of the SPO analyses: (a) maximum concrete strain on the columns of the ground story, (b) maximum chord rotations and, (c) maximum shear forces on the columns of the ground and first stories

According to the TEC (2018) classification in terms of the concrete strain, one column (C2) exceeds the SD limit, and one other column (C3) is approximate to this limit at the ground story (Fig 5(a)). The concrete strain of the columns in the OGS model is larger compared to BF even though these values were obtained at a smaller target displacement in the OGS frame (Figs 4 and 5). Two columns (C2 and C3) go beyond the NC limit and one column (C1) exceeds the SD state at the ground story of the OGS model. All columns at the ground level and one column at the upper story of the BF remain in between the SD and NC limits when the Eurocode 8 definition in terms of chord rotation is considered (Fig. 5(b)). In the

OGS frame, the chord rotations of columns at the ground story increase substantially and go beyond the NC limit state. On the other hand, there was an abrupt decrease in the chord rotations of the first story columns in this frame compared to BF. In this story, the observed negative chord rotations may be attributed to the contribution of higher modes of vibration due to the irregular distribution of rigidity in the OGS model. It should be noted that the assessment of Eurocode 8 according to the chord rotation may be regarded as more conservative in comparison to that of TEC [12] with respect to the local strain obtained by SPO analyses. This was especially notable for the BF model. There was no major difference between the OGS and BF concerning the column shear demands at the ground story (Fig. 5(c)). As one may anticipate, there was a considerable decline in the shear demands of the first story columns owing to the infills of the OGS frame compared to BF.

4.2. Results of IDA

To be comparable with the SPO results, in the IDA analysis, the base shear was determined as the “intensity measure” and roof drift was chosen as the “engineering demand parameter”. The consequent IDA curves of all ground acceleration records are given in Fig. 6(a). The statistical 16%, 50% (median) and 84% fractile curves are presented in Fig. 6(b). When the IDA results of bare and OGS frames are statistically compared, it may be stated that the dispersion is higher for the OGS in comparison to BF.

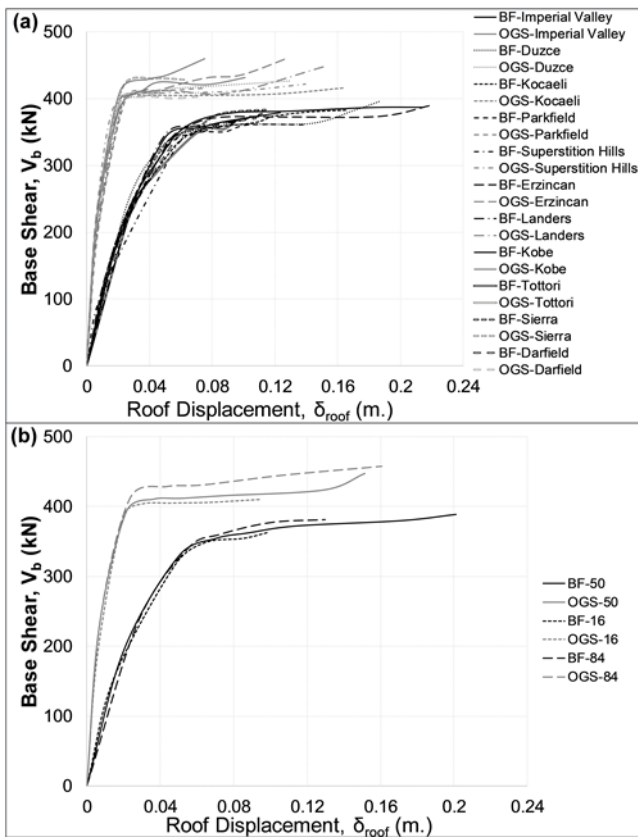


Figure 6. The incremental dynamic analysis curves of BF and OGS frame: (a) under all acceleration records, (b) 16%, 50% (median) and 84% fractile curves

Referring to FEMA 350, Vamvatsikos and Cornell [22] assume that the near-collapse limit is defined either by the point where the local slope of the IDA curve attains 20% of the initial (i.e., elastic) slope or maximum inter-story drift ratio extends to 10% for the steel moment-resisting frames. In this study, the definition that states an 80% reduction in the initial rigidity is considered to determine the NC limit state by a graphical rendition of the IDA curves. The same definition of Eurocode 8 for the NC limit state in terms of chord rotation (i.e., 0.0128 rad) that was used in the previous section is also evaluated here. Additionally, the concrete strain limit value of the TEC [12] for the NC (i.e., 0.0068) which is generally more critical compared to the strain of reinforcement is also considered in this part once again. It is worth noting that none of these limit state definitions, except the graphical rendition proposed by Vamvatsikos and Cornell [12] take the infills into account during the assessment of the building. A graphical definition for the limit states naturally considers all structural characteristics, such as the effect of infill walls assigned to the model.

The point corresponding to an 80% reduction in the initial rigidity (i.e. NC limit state of FEMA 350) is shown in Fig. 7 on the median IDA curves as exemplarily. This procedure was applied for the IDA curves of all models under each ground acceleration record where the IDA step nearest to this level was designated as the limit for the NC. Eventually, the local values for the chord rotation and concrete strain are obtained at this limit. The median, 16th and 84th percentile of these demands obtained from the representative column “C2” are presented in Fig. 8 together with the code limits for the NC state.

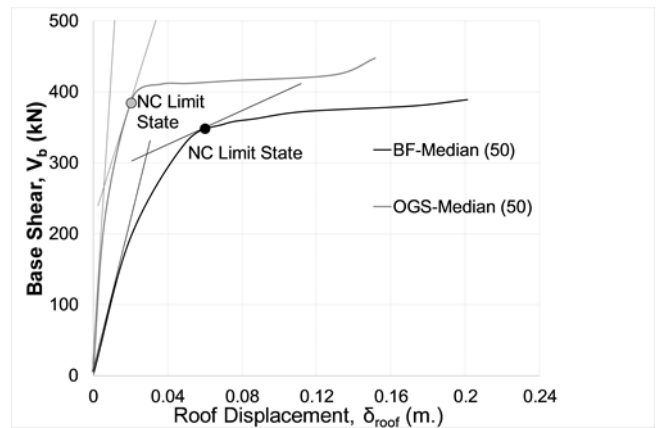


Figure 7. The graphical definition of the near-collapse (NC) limit state according to FEMA 350

As shown in Fig. 7, the limit for the NC is determined at the transition part of all curves between the initial (ascending) portion and the flat (or almost flat) remaining portion. The NC was experienced at a smaller roof drift in the case OGS frame in comparison to BF. There may be two reasons for this: the initial rigidity of the OGS model is higher and the transition from the initial region to the remaining flat region is sharper in the case of OGS in comparison to BF. This caused a reduction in the demand values of the OGS frame at the NC limit state

as exemplarily shown in Fig. 8 for column C2. It should be noted that this result was also the case in the other columns of the ground story.

When compared with the graphical method of FEMA-350 [21], the TEC [12] seems to be slightly more conservative while describing the NC limit state for the BF by employing the strain in the columns (Fig. 8(a)). However, this was not the case in the OGS frame and the limit for the NC is experienced earlier with regard to FEMA 350. The NC limit defined by Eurocode 8 according to the chord rotation was much larger than the one determined by FEMA 350 for the ground story columns of both types of frames (Fig. 8(c and d)).

The plastic hinge formations throughout the structure were designated to evaluate the description of FEMA 350 for the near-collapse limit. The plastic hinge formation was identified by observing the hysteretic moment-rotation diagrams at the integration sections of the members. This was done at the IDA step which was specified as the limit for the NC. The consequent moment-rotation diagrams at the initial sections of columns C1 and C4 are presented in Fig. 9. An “idealized yield point” has been transcended by the initial section of column C1, so that the plastic hinge formation can be defined (Fig. 9(a)). However, the bottom section of column C4 has not experienced any inelastic response (Fig. 9(b)).

The resulting distributions of the plastic hinges in the IDA step specified as NC limit by FEMA 350 and the following step are illustrated in Fig. 10 for the Duzce record. The maximum column chord rotations formed at the ground story corresponding to these steps are also denoted in the same figure. According to Fig. 10(a), the number of plastic hinges was not adequate to result in collapse (i.e., instability) when the NC limit defined by FEMA 350 was reached for the BF (i.e., chord rotation equals 0.0074). On the other hand, the collapse was formed at the first two-story levels in the following step when the ultimate chord rotation of the ground story columns attained 0.0113. It may be stated that the collapse seems to form immediately after the FEMA 350 NC limit. Consequently, the description of FEMA 350 for the NC limit state, which was proposed for the steel frames may be regarded as convenient for the reinforced concrete bare frames. Whereas the collapse mechanism was already produced for the OGS frame at the NC limit of FEMA 350 (Fig. 10(b)). It may be concluded that the definition of NC limit state at an earlier stage may be regarded as more appropriate for the OGS frame.

4.3. Comparison of SPO Analyses and IDA Results

The base shear-roof drift relationships obtained by SPO and IDA (median) are presented together in Fig. 11 for each model. Similar to the statement of Vamvatsikos and Cornell [22], when the intensity measure and engineering demand parameters are selected as those in this study, the capacity diagrams achieved by both SPO and IDA methods are almost identical in the initial region. Yet, the base shear (or S_a determined by Eqn. (5)) capacities determined by the SPO and IDA are also quite similar which is in contradiction to the results of

Vamvatsikos and Cornell [22]. Eventually, the curves of each analysis method begin to differentiate after the ultimate base shear capacity is reached. This result was more significant in the case of OGS.

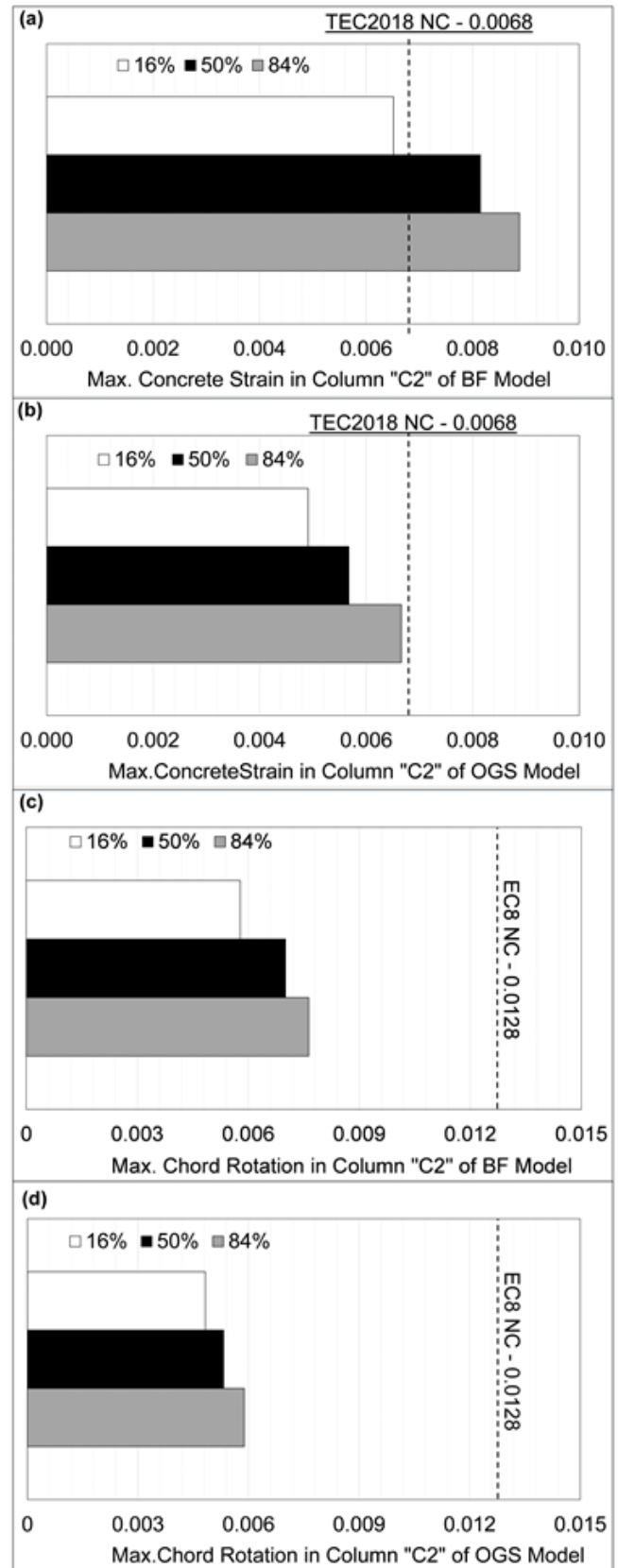


Figure 8. The comparison of NC limit state definitions of FEMA 350, TEC, and Eurocode 8

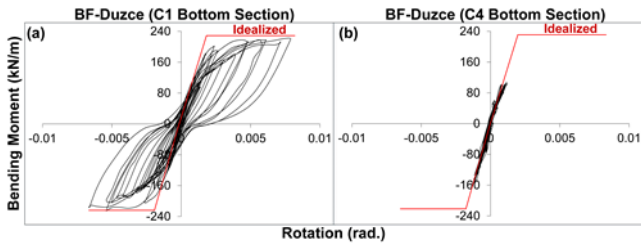


Figure 9. Moment-rotation behavior at the initial sections of columns (a) C1 and (b) C4 at the NC limit of FEMA 350

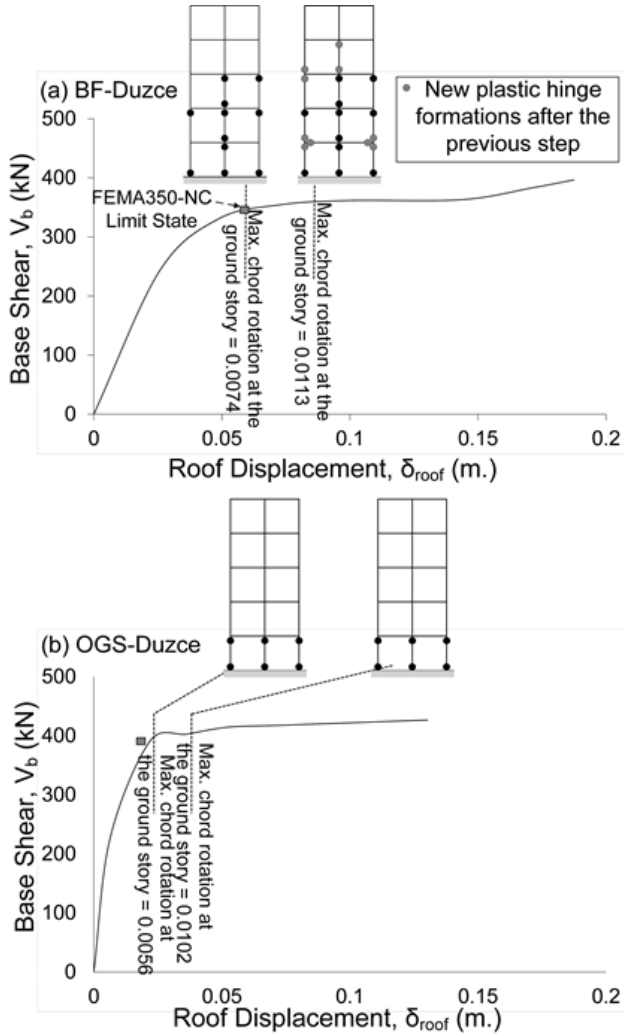


Figure 10. The plastic hinge formations of the (a) BF and (b) OGS models at two stages of IDA for Duzce record

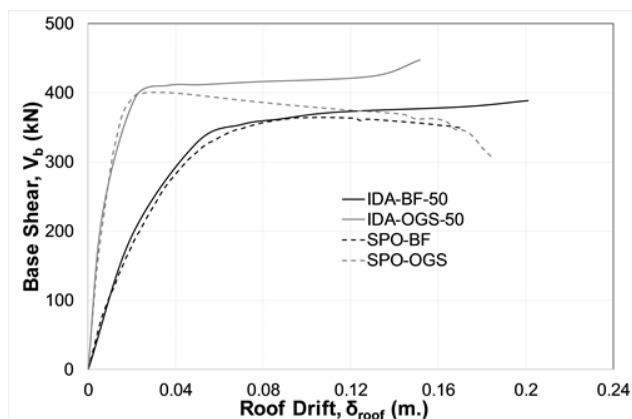


Figure 11. Base shear-root drift diagrams of SPO and IDA (median)

In Fig. 12, the maximum concrete strain and chord rotation of column C2 are compared for three steps of the response (i.e., in the case of Imperial Valley record exemplarily). The local demand parameters of the BF derived from the SPO and IDA were very approximate at the initial part of the response and started to differentiate as the related capacity curves separate (Fig. 12). This was more considerable for the concrete strain, which may clarify the more conservative assessment conducted by the SPO according to the chord rotation (i.e., concrete strain remains lower in the SPO). Although the separation of SPO and IDA curves after the ultimate capacity is more distinct for the OGS, the inelastic demand values determined by the two methods at the same roof drift are quite approximate in all regions of the response of this model. This may be related to the concentration of demand at the story level without infills. The measure of the scattering of damage between the stories of BF may be dissimilar for the SPO and IDA which may result in the demands changing at different stages of response in this model.

5. Conclusion

A reinforced concrete bare and OGS frame were analyzed using SPO and IDA regarding the NC limit state descriptions of different seismic codes. The two different analyses methods were also compared in terms of this evaluation. It should be noted that the presented results were obtained according to the assumptions of the study.

The assessment by SPO provided much larger demands for the OGS frame as may be expected, although the corresponding target displacement was smaller for the OGS compared to BF. According to the SPO analyses, it may be stated that the seismic assessment with regard to the definition of Eurocode 8 in terms of chord rotation is more conservative than the definition of TEC [12] in terms of concrete strain. This statement is more considerable for the BF model.

The NC limit state described by FEMA 350 which is suggested actually for the steel frames and based on a graphical interpretation of the IDA results was also suitable for the RC bare frame considered in this study. However, the same conclusion may not be valid for the OGS frame due to the plastic hinge formations that indicate an early column-sideway mechanism in this model. It may be more appropriate to define the near-collapse at an earlier stage on the IDA curve for the RC frames with OGS. As opposed to the conclusion from the SPO analyses, the concrete strain limit of TEC [12] is more conservative in describing the near-collapse for the columns of bare RC frames considering the IDA results, which is not the case for the frame with OGS. The chord rotation limit of Eurocode 8 seems to describe the near-collapse of the columns at a much later stage on the IDA curves considering both BF and OGS models. The quite early signs of collapse without producing considerable inelastic deformations should be regarded more conservatively during the seismic assessment of existing nonductile OGS buildings.

The differences in the assessment according to different codes by using either SPO or IDA results may be

understood after a closer look at the local demands of the ground story columns at different stages of the results. Although the global SPO capacity and IDA curves are very close for the bare RC frame, the dissociation of local demands obtained by these two analysis methods increases as the inelastic actions progress within the structure. This was more distinct for the concrete strain which was significantly smaller in the SPO results of BF in comparison to IDA. On the other hand, the global SPO and IDA curves of OGS differ from each other considerably during the inelastic response. Yet, the local demand values are close at all stages of the two analysis methods.

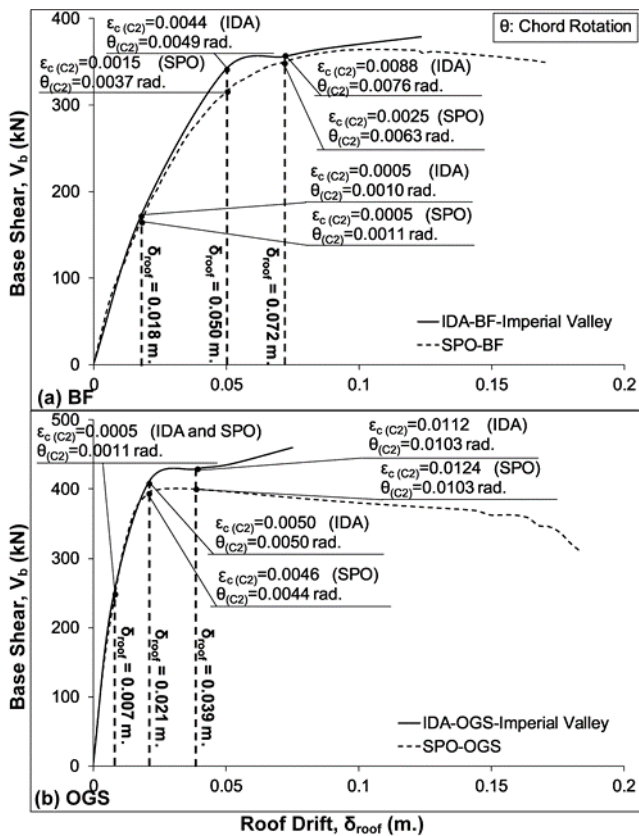


Figure 12. The maximum concrete strain and chord rotation of column C2 at various steps of the SPO and IDA curves: (a) for BF and (b) for OGS

Acknowledgement

This work was supported by the Adnan Menderes University Scientific Research Projects Commission [grant number MF-19013].

Author contributions

Emre Akin: Conceptualization, Methodology, Software, Writing-Original draft preparation, Validation. **Emad Kanas:** Data curation, Writing-Original draft preparation, Visualization, Investigation, Writing-Reviewing and Editing.

Conflicts of interest

The authors declare no conflicts of interest.

References

- Asteris, P. G. (2003). Lateral Stiffness of Brick Masonry Infilled Plane Frames. *Journal of Structural Engineering, American Society of Civil Engineers (ASCE)*, 129(8), 1071–1079. [https://doi.org/10.1061/\(ASCE\)0733-9445\(2003\)129:8\(1071\)](https://doi.org/10.1061/(ASCE)0733-9445(2003)129:8(1071))
- Cavaleri, L. & Di Trapani, F. (2014). Cyclic response of masonry infilled RC frames: Experimental results and simplified modeling. *Soil Dynamics and Earthquake Engineering*, 65, 224–242. <https://doi.org/10.1016/j.soildyn.2014.06.016>
- Comite Euro-International du Beton (CEB) (1996). *RC Frames Under Earthquake Loading: State of the Art Report*. Thomas Telford, London, UK.
- Dolšek, M., & Fajfar, P. (2008). The effect of masonry infills on the seismic response of a four storey reinforced concrete frame-a probabilistic assessment. *Engineering Structures*, 30(11), 3186–3192. <https://doi.org/10.1016/j.engstruct.2008.04.031>
- Hashemi, A., & Mosalam, K. M. (2006). Shake-table experiment on reinforced concrete structure containing masonry infill wall. *Earthquake Engineering and Structural Dynamics*, 35(14), 1827–1852. <https://doi.org/10.1002/eqe.612>
- Mehrabi, A. B, Shing, P. B., Schuller, M. P., & Noland, J. L. (1996). Experimental Evaluation of Masonry-Infilled RC Frames. *Journal of Structural Engineering*, 122(3), 228–237. [https://doi.org/10.1061/\(ASCE\)0733-9445\(1996\)122:3\(228\)](https://doi.org/10.1061/(ASCE)0733-9445(1996)122:3(228))
- Negro, P. & Verzeletti, G. (1996). Effect of infills on the global behaviour of R/C frames: Energy considerations from pseudodynamic tests. *Earthquake Engineering and Structural Dynamics*, 25(8), 753–773. [https://doi.org/10.1002/\(SICI\)1096-9845\(199608\)25:8<753::AID-EQE578>3.0.CO;2-Q](https://doi.org/10.1002/(SICI)1096-9845(199608)25:8<753::AID-EQE578>3.0.CO;2-Q)
- Dolšek, M., & Fajfar, P. (2001). Soft storey effects in uniformly infilled reinforced concrete frames. *Journal of Earthquake Engineering*, 5(1), 12. <https://doi.org/10.1080/13632460109350383>
- Negro, P., & Colombo, A. (1997). Irregularities induced by nonstructural masonry panels in framed buildings. *Engineering Structures*, 19(7), 576–585. [https://doi.org/10.1016/S0141-0296\(96\)00115-0](https://doi.org/10.1016/S0141-0296(96)00115-0)
- Akin, E. (2019). Open ground story in properly designed reinforced concrete frame buildings with shear walls. *Structures*, 20, 822-831. <https://doi.org/10.1016/j.istruc.2019.07.003>
- Eurocode 8 (2005). *European Standard EN 1998-3:2005: Design of structures for earthquake resistance - Part 3: Assessment and retrofitting of buildings*. Comite Europeen de Normalisation, Brussels, Belgium.
- TEC (2018). *Turkish Earthquake Code for Buildings*. Republic of Turkey Prime Ministry Disaster and Emergency Management Authority, Ankara, Turkey.

13. SeismoStruct (2020). A computer program for static and dynamic nonlinear analysis of framed structures. Seismosoft Ltd. <https://seismosoft.com>
14. Kadaş, K. (2006). Influence of idealized pushover curves on seismic response. MSc Thesis, Middle East Technical University, Graduate School of Natural and Applied Sciences, Ankara, Turkey, 320p.
15. Mander, J. B., Priestley, M. J. N., & Park, R. (1988). Theoretical Stress-Strain Model for Confined Concrete. *Journal of Structural Engineering*, 114(8), 1804–1826. [https://doi.org/10.1061/\(ASCE\)0733-9445\(1988\)114:8\(1804\)](https://doi.org/10.1061/(ASCE)0733-9445(1988)114:8(1804))
16. Martínez-Rueda, J. E., & Elnashai, A. S. (1997). Confined concrete model under cyclic load. *Materials and Structures*, 30(3), 139–147. <https://doi.org/10.1007/BF02486385>
17. ACI (American Concrete Institute) (2008). Building code requirements for structural concrete (ACI 318M-08) and Commentary. Farmington Hills, MI, USA.
18. American Society of Civil Engineers (ASCE) (2000). *Prestandard and commentary for the seismic rehabilitation of buildings (FEMA 356)*. Washington, D.C., USA
19. TEC (2007). *Turkish Earthquake Code for Buildings*. Republic of Turkey Prime Ministry Disaster and Emergency Management Authority, Ankara, Turkey.
20. SeismoMatch (2018). A computer program for spectrum matching of earthquake records. Seismosoft Ltd. <https://seismosoft.com>
21. FEMA-350 (2000). *Recommended Seismic Design Criteria for New Steel Moment-Frame Buildings*. Washington, D.C., USA.
22. Vamvatsikos, D., & Cornell, C. A. (2005). Direct estimation of the seismic demand and capacity of multidegree-of-freedom systems through incremental dynamic analysis of single degree of freedom approximation. *Journal of Structural Engineering*, 131(4). [https://doi.org/10.1061/\(ASCE\)0733-9445\(2005\)131:4\(589\)](https://doi.org/10.1061/(ASCE)0733-9445(2005)131:4(589))



© Author(s) 2023. This work is distributed under <https://creativecommons.org/licenses/by-sa/4.0/>